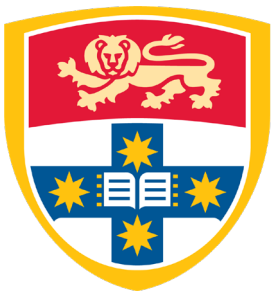

THE UNIVERSITY OF SYDNEY

Graphitic Carbon Materials from Clean Hydrogen Production for Advanced Energy Storage Systems

Yuqi Pan

A thesis submitted in fulfillment of the requirements for the degree of

Doctor of Philosophy

School of Chemical and Biomolecular Engineering

Faculty of Engineering

The University of Sydney

2024

Statement of originality

This is to certify that to the best of my knowledge, the content of this thesis is my own work. This thesis has not been submitted for any degree or other purposes.

I certify that the intellectual content of this thesis is the product of my own work and that all the assistance received in preparing this thesis and sources have been acknowledged.

Yuqi Pan

Jan 2024

Authorship attribution statement

Chapter 3 of this thesis is published as **Y. Pan**, V. Lo, L. Cao, A. Roy, B. Chivers, N. Noorbehesht, Y. Yao, J. Wang, L. Wei, Y. Chen, Graphitic carbon from catalytic methane decomposition as efficient conductive additives for zinc-carbon batteries, Carbon 192 (2022) 84-92.

I conceived this study, designed, and performed the experiments, analysed the data, validated the results, wrote and revised the manuscript.

Chapter 4 of this thesis is published as **Y. Pan**, L. Cao, Y. Yao, Y. Tao, V. Lo, Z. Zheng, B. Chivers, J. Prabowo, F. Liu, L. Lai, Graphitic Co‐Products of Clean Hydrogen Production Enabling High‐Rate‐Performance Dual‐Carbon Batteries, Adv. Energy Mater. (2023) 2300495.

I conceived this study, designed, and performed the experiments, analysed the data, validated the results, wrote and revised the manuscript.

Attesting authorship attribution statement

In addition to the statements above, in cases where I am not the corresponding author of a published item, permission to include the published material has been granted by the corresponding author.

Yuqi Pan

Jan 2024

As supervisor for the candidature upon which this thesis is based, I can confirm that the authorship attribution statements above are correct.

Yuan Chen

Jan 2024

Acknowledgments

I would like to express my sincere appreciation to my supervisor, Prof. Yuan Chen, for his continued generous academic support, guidance, patience, and encouragement. When I face challenges, he offers me academic opinions to solve problems and always encourages me to carry on. He is a responsible supervisor who guides me in developing research ideas, designing experiments, and revising manuscripts for publication. The professional knowledge and research skills I have learned from him will greatly benefit my future career. All the progress I achieved during my Ph.D. candidature is highly attributed to the supervision of Prof. Yuan Chen.

I would like to thank my auxiliary supervisor, Dr. Wei Li, greatly for his expert guidance, generous help, and kind encouragement and support. I would also like to express gratitude to all the experts involved in my research project for their valuable help and support: Dr. Liuyue Cao, Dr. Yuanyuan Yao, Dr. Zhi Zheng, Dr. Victor Lo, Dr. Benjamin Chivers, Dr. Anup Roy, Dr. Nikan Noorbehesht, Dr. Zengxia Pei, Dr. Asif Mahmood, Dr. Cheng Wang, Ms. Yongwen Tao, Mr. Justin Prabowo, Mr. Leo Lai, Mr. Fangzhou Liu, and Ms. Jiani Wang. Additionally, I would like to thank my great team members for their assistance and for providing a positive research environment: Dr. Zixun Yu, Dr. Jing Li, Mr. Di Zhu, Ms. Fangxin She, Ms. Jiaxiang Chen, Ms. Xin Yang, Ms. Mohan Li, Mr. Yeyu Deng, Mr. Jiacheng Wu, and Mr. Yueyu Ding.

Further, I would like to acknowledge my family and friends. Specifically, I would like to express my sincerest gratitude to my parents, Mr. Yong Pan and Ms. Wei Song, for their endless love, financial support and unconditional encouragement to me for completing my Ph.D. candidature. I want to express my great thanks to my boyfriend, Dr. Huan Li, for his valuable support, love, and company.

Abstract

Catalytic methane pyrolysis ($CH_4 \rightarrow 2H_2 + C$) is a promising hydrogen production process which directly splits methane into hydrogen and solid carbon materials without direct emissions of carbon dioxide. With a mass ratio of hydrogen to solid carbons of 1 to 3, large amounts of carbon materials are generated from the catalytic methane pyrolysis process. Developing value-added applications for these solid carbon co-products could eliminate waste generation from the process, bring economic benefits to the process, and significantly offset hydrogen production costs. Carbon materials play a crucial role in electrochemical energy storage devices, serving as essential components of electrodes, including conductive additives and active energy storage materials. With the ever-growing energy demand, the continuous development of the energy storage field holds great potential for the accommodation of co-produced carbon materials from clean hydrogen production via the catalytic pyrolysis process.

In Chapter 2, a comprehensive study of the most used techniques for characterizing carbon materials and determination of their physiochemical properties and electrochemical performances is conducted. The analytical methods include microscopic and diffraction techniques (scanning electron microscopy (SEM), transmission electron microscopy (TEM), and X-ray diffraction (XRD)) for examining morphology and crystal structure, nitrogen physisorption technique for determining surface area and pore structure, spectroscopic techniques (Raman spectroscopy, and X-ray photoelectron spectroscopy (XPS)) for investigating chemical structure, defect level and surface functional groups, and thermal technique (thermogravimetric analysis (TGA)) for analyzing carbon purity and quality. Commonly used electrochemical characterization techniques are discussed, such as linear sweep voltammetry and cyclic voltammetry, electrochemical impedance spectroscopy, and galvanostatic charge–discharge measurements. These technologies are used in further works to

investigate and understand the characteristics of solid carbon materials co-produced from the catalytic methane pyrolysis process.

In Chapter 3, I demonstrate how graphitic carbon materials from the catalytic methane pyrolysis process work as efficient carbon conductive additives for zinc-carbon batteries. Graphitic carbon materials are synthesized as co-products from methane pyrolysis using iron ore catalysts, followed by the standard high-temperature thermal treatment and the alternative electrochemical purification to reach high purity of 99.82 and 99.59 wt.%, respectively. Manganese dioxide cathodes containing purified carbon materials as conductive additives present two essential properties: high conductivity (98 S cm^{-1}) and good electrolyte absorption capabilities (4.2 mg mg^{-1}). Zinc-carbon batteries assembled using these carbon materials show the advantages of higher electrode conductivity, larger specific capacity under higher current densities, better rate performance, lower internal resistance, and superior long-term stability compared with commercial carbon conductive additives (Super P).

In Chapter 4, I present the utilization of graphitic carbon co-products from the methane pyrolysis process as active materials for both anode and cathode electrodes, enabling high-rate-performance dual-carbon batteries, outperforming commercial natural and synthetic graphite. Dual-carbon batteries are emerging as a promising battery system due to the unique advantages of low cost, high sustainability, and high working voltage. Their challenges of unsatisfied cyclability and poor rate performance result from graphite cathodes suffering from severe structural deterioration, calling for advanced carbon electrode materials. Purified graphitic carbon co-products from methane pyrolysis are generated using a standard high-temperature thermal treatment or a room-temperature electrochemical method. Compared to graphite, they have smaller crystalline sizes and larger surface areas, enabling faster surface redox reactions and better structural stability upon electrolyte ion intercalation. Dual-carbon batteries assembled with purified graphitic carbon using 1M lithium hexafluorophosphate ($LiPF_6$) ethyl

methyl carbonate electrolyte deliver energy storage capacities of 75.1 and 74.7 mAh g^{-1} at 500 mA g^{-1} with capacity retentions of 79.2 and 93.4 % after the high-rate charge/discharge over 5000 mA g^{-1}, respectively. They can also be cycled at 500 mA g^{-1} over 300 cycles without capacity decay, demonstrating excellent cycling stability. They show energy densities of 168.7 and 159.7 Wh kg^{-1} at power densities of 10.6 and 10.8 kW kg^{-1}, outperforming recently reported dual-carbon batteries.

Through the studies of Chapter 3 and 4, the suitability of graphitic carbon materials from catalytic methane pyrolysis process serving as conductive additives and active materials in electrodes has been validated, outperforming commercial conductive additive (Super P) and conventional graphite electrodes, respectively. These findings open new applications in energy storage field for these graphitic carbon co-products from methane pyrolysis, beneficial for developing advanced energy storage devices, as well as enhancing the economic viability of the clean hydrogen production process.

Table of Contents

Statement of originality....ii

Authorship attribution statement.... iii

Attesting authorship attribution statement....iv

Acknowledgments....v

Abstract....vi

Table of Contents....ix

List of Figures.... xiii

List of Tables....xix

List of Publications....xx

Chapter 1. Introduction....1

1.1 Background....1

1.2 Catalytic methane pyrolysis....2

1.3 Carbon materials from catalytic methane pyrolysis....9

1.3.1 Different co-produced carbon materials....9

1.3.2 Applications of carbon materials from catalytic methane pyrolysis....12

1.4 Carbon materials in batteries....14

1.4.1 Conductive additives....14

1.4.2 Electrode active materials....17

1.5 Thesis scope....21

Chapter 2. Characterization techniques of carbon materials 24

2.1 Carbon materials preparation 24

2.2 Scanning electron microscopy (SEM).....25

2.3 Transmission electron microscopy (TEM).....27

2.4 X-ray diffraction (XRD).....28

2.5 Nitrogen (N_2) physisorption technique 30

2.6 Raman spectroscopy.....31

2.7 X-ray photoelectron spectroscopy (XPS).....33

2.8 Thermogravimetric analysis (TGA).....35

2.9 Electrode fabrication and electrolyte preparation 36

2.10 Coin cell assembly 37

2.11 Electrochemical characterization 38

2.11.1 Linear sweep voltammetry (LSV) and cyclic voltammetry (CV).....38

2.11.2 Electrochemical impedance spectroscopy (EIS) 40

2.11.3 Galvanostatic charge–discharge (GCD) measurements 41

Chapter 3. Graphitic carbon from catalytic methane decomposition as an efficient conductive additive for zinc-carbon batteries.....43

3.1 Introduction.....43

3.2 Experimental section.....44

3.2.1 Material synthesis.....44

3.2.2 Material characterization.....48

3.2.3 Electrode fabrication and characterization 48
3.2.4 Zn-C battery assembly and characterization 49
3.3 Results and discussion 50
3.3.1 Properties of carbon materials 50
3.3.2 Properties of fabricated electrodes 56
3.3.3 Properties of assembled Zn-C batteries 57
3.4 Conclusion 62
Chapter 4. Graphitic co-products of clean hydrogen production enabling high-rate-performance dual-carbon batteries 64
4.1 Introduction 64
4.2 Experimental section 68
4.2.1 Material synthesis 68
4.2.2 Material characterization 70
4.2.3 Electrode fabrication and battery cell assembly 71
4.2.4 Electrochemical measurement and characterization 71
4.2.5 Calculations of energy density and power density of DCB full cells 72
4.3 Results and discussion 74
4.3.1 Characteristics of graphitic carbon materials 74
4.3.2 Electrochemical behaviors of graphitic cathodes 83
4.3.3 Electrochemical performances of graphitic anodes 96
4.3.4 Electrochemical performances of DCB full cells 99

4.4 Conclusion.....107

Chapter 5. Conclusions and outlooks.....108

5.1 Conclusions.....108

5.2 Outlooks.....110

Reference.....113

List of Figures

Figure 1-1. Global hydrogen production by technology from 2020 to 2022 [13]. 3

Figure 1-2. A general process of catalytic methane pyrolysis for hydrogen production using a fluidized bed reactor with carbon catalysts [19]. 6

Figure 1-3. Reaction mechanisms for catalytic methane pyrolysis on the catalyst surface, (a) molecular adsorption mechanism, and (b) dissociative adsorption mechanism [18]. 7

Figure 1-4. Vapor-liquid-solid (VLS) mechanism for the catalytic growth of filamentous carbon on metal catalysts [18]. 10

Figure 1-5. The formation mechanisms for carbon nano-onions (CNOs): (a) CNOs with a metal particle core and (b) CNOs with an empty core [63]. 11

Figure 1-6. Schematic figure of a cylindrical Leclanché battery in a cutaway view [75]. 15

Figure 1-7. Schematic illustration of typical conducting models of carbon materials as conductive additives, from left to right: point-to-point mode, plane-to-point mode, and hybrid-dimensionality mode [78]. 17

Figure 1-8. Structures of typical carbon materials: (a) graphite, (b) single-walled carbon nanotubes, and (c) multi-walled carbon nanotubes [95]. 18

Figure 2-1. Schematic illustration of the synthesis of graphitic carbon materials from catalytic methane pyrolysis process using Fe ore catalysts. 24

Figure 2-2. (a) Schematic diagram of the basic components of a scanning electron microscope [156]. (b) SEM images of typical carbon materials [159]. 26

Figure 2-3. (a) Schematic illustrations of a light microscope (left) and a transmission electron microscope [160]. TEM images of graphitic carbon nanofibres, (b) hollow-tunnel structures,

(c) walls of the hollow structures, (d) graphene sheets and (e) determination of interlayer spacing of graphene sheets [162]. 28

Figure 2-4. (a) Basic components of an X-ray diffractometer and their geometric arrangement [156]. (b) XRD profiles of pure graphite and synthesized graphene oxide [163]. 29

Figure 2-5. Schematic diagram of a physical adsorption analyser for determining the specific surface area and pore size distribution of carbon materials [165]. 31

Figure 2-6. (a) Schematic diagram of a Raman microscopic system [156]. Typical Raman spectra of (b) single crystal graphite and (c) commercial graphite [158]. 32

Figure 2-7. (a) Schematic diagram of an X-ray photoelectron spectrometer [172]. (b) XPS survey of carbon nanotubes (CNTs) and oxidized CNTs (O-CNTs), and (c) XPS spectra of C 1s of O-CNTs [174]. 34

Figure 2-8. (a) Main components of a TGA instrumentation, and (b) a TGA curve representing the decomposition of materials [156]. 35

Figure 2-9. Schematic illustrations of (a) the electrode components and (b) the doctor blade method for slurry coating. 36

Figure 2-10. Schematic diagram of a typical coin cell configuration. 38

Figure 2-11. (a) A typical three-electrode electrochemical cell for LSV and CV measurements [176]. (b) A typical cyclic voltammogram for a battery-type material [178]. 39

Figure 2-12. Nyquist plots for an electrochemical process and the Randles equivalent electrical circuit [182]. 41

Figure 2-13. (a) A typical GCD profile for a battery-type material [178]. An example of (b) the rate performance of a lithium-ion battery cell under different current densities, and (c) the corresponding GCD curves [186]. 42

Figure 3-1. Schematic illustrations of (a) the synthesis of graphitic carbon materials encapsulating Fe particles by catalytic decomposition of CH_4 on Fe ore catalysts and (b) the electrochemical cell used to purify the graphitic carbon materials.....46

Figure 3-2. SEM and TEM images of carbon materials used as conductive additives in this study. SEM images of (a) Super P, (b) GC, (c) TG, and (d) EG. TEM images of (e) GC, (f) TG, (g) EG, and their graphitic structures (h) GC, (i) TG, and (j) EG. 51

Figure 3-3. Particle size distribution profiles of carbon materials used as conductive additives in this study: Super P, GC, TG, and EG. 52

Figure 3-4. (a) N_2 physisorption isotherms, (b) Pore size distribution, (c) Raman spectra, and (d) TGA profiles of different carbon materials: Super P, GC, TG, and EG. 53

Figure 3-5. Derivative thermogravimetry (DT) profiles of different carbon materials: Super P, GC, TG, and EG.....55

Figure 3-6. Electrolyte absorption capabilities of EMD electrodes fabricated using different carbon conductive additives over time. 57

Figure 3-7. Galvanostatic discharge curves of Zn-C batteries fabricated using different carbon conductive additives under the discharge current density of (a) 1.0 A g^{-1}, (b) 0.5 A g^{-1}, (c) 0.1 A g^{-1}, and (d) 0.05 A g^{-1}. (e) The comparison of the specific capacity of Zn-C batteries under different discharge current densities. The inset shows a magnified plot at the low discharge current density region. (f) Nyquist plots of Zn-C batteries. The inset shows the intercept of the impedance curve with the real axis. 59

Figure 3-8. (a) GITT profiles of Zn-C batteries assembled using different carbon additives, (b) the enlargement of one GITT segment at the third test cycle, (c) cell resistances of Zn-C batteries during 30 test cycles of GITT, and (d) OCV plots of Zn-C batteries in long-term stability tests over one month. 61

Figure 3-9. Galvanostatic discharge curves of Zn-C batteries under 0.1 A g^{-1} after their long-term stability test. 62

Figure 4-1. Schematic illustrations of (a) a dual-carbon battery, (b) the synthesis of graphitic materials encapsulating Fe ore particles by catalytic CH_4 pyrolysis, (c) high-temperature thermal purification, and (d) room-temperature electrochemical purification. SEM images of graphitic materials used in this study: (e) natural graphite, (f) synthetic graphite, (g) high-temperature purified, and (h) electrochemically purified graphitic materials from CH_4 pyrolysis. 67

Figure 4-2. TEM images of (a) graphitic carbon encapsulating a Fe particle produced in the methane pyrolysis process, (b) TG, and (c) EG. HR-TEM images of (d) TG and (e) EG with their corresponding interplanar distances. 75

Figure 4-3. Particle size distribution profiles of graphitic carbon materials used in this study: NG, SG, TG, and EG. 76

Figure 4-4. Physiochemical properties of graphitic materials used in this study. (a) N_2 physisorption isotherms, (b) pore size distribution, (c) Raman spectra, (d) XRD profiles, and (e) XPS spectra of C 1s of NG, SG, TG, and EG. 77

Figure 4-5. XPS survey of graphitic carbon materials used in this study: NG, SG, TG, and EG. (C:O): the atomic ratio of C to O. 80

Figure 4-6. (a) TGA weight loss profiles and (b) DT profiles of different graphitic carbon materials: NG, SG, TG, and EG. 82

Figure 4-7. Electrochemical behaviors of graphitic cathodes in graphite/Li half cells. (a) GCD profiles of cathode half cells under 1 C. (b) A TG/Li half cell charge curve during anion intercalation segmented into three regions: I, II, and III. The labels from B to E correlate with the corresponding points on the *dQ/dV* curve shown as an inset. (c) Capacity in Region I, II,

and III of NG, SG, TG, and EG during charging. (d) CV curves of TG/Li half cells at the scan rates of 0.1, 0.25, 0.5, 0.75, and 1 mV s^{-1}. (e) The corresponding log *i vs.* log *v* profiles used to determine the *b* values of TG cathodes. (f) The calculated *b* values of anion storage in different graphitic cathodes. 85

Figure 4-8. Schematic illustrations of graphite intercalation compounds (GICs) with different stage features (stage number SN 4, 3, 2, and 1) [301]. 87

Figure 4-9. Charge curves of graphitic cathodes segmented into three regions and the corresponding *dQ/dV* profiles in the insets: (a) NG, (b) SG, and (c) EG in graphite/Li half-cells. 87

Figure 4-10. CV profiles of graphite/Li half-cells at the scan rates from 0.1–1.0 mV s^{-1}: (a) NG, (b) SG, and (c) EG. The corresponding log *i* versus log *v* profiles to determine *b* values for (d) NG, (e) SG, and (f) EG cathodes, respectively. 90

Figure 4-11. Pre-cycling of graphite/Li half cells for 60 cycles under 1 C before rate performance tests to ensure that all cells have reached a stable condition and eliminate the effect of graphite activation on measured cell capacities. 91

Figure 4-12. (a) Nyquist plots of EIS spectra of fresh graphite/Li half cells. The inset displays the equivalent circuit for fitting data. (b) The rate performance of graphite/Li half cells. (c) Comparison of the rate performance from 1–50 C. SEM images and XRD patterns of graphitic cathodes before and after the rate performance tests: (d, h, l) NG, (e, i, m) SG, (f, j, n) TG, and (g, k, o) EG, respectively. 92

Figure 4-13. GCD curves from rate capability tests under the initial 1 C rate (5^{th} cycle) and under 1 C rate after 50 C rate tests (61^{st} cycle) for different graphite cathodes: (a) NG, (b) SG, (c) TG, and (d) EG. 94

Figure 4-14. (a) Rate performance of graphite/Li half cells with different graphitic anodes. (b) Comparison of the rate performance of graphitic anodes from 0.1–10 C. 96

Figure 4-15. GCD curves from rate capability tests under different current rates of 0.1 C (10^{th} cycle), 0.2 C (15^{th}), 0.35 C (20^{th}), 0.5 C (25^{th}), 1 C (30^{th}), and 2 C (35^{th}) for different graphite anodes: (a) NG, (b) SG, (c) TG, and (d) EG.....98

Figure 4-16. GCD curves of graphite/Li half cells with NG, SG, TG, and EG anodes from rate capability tests under different current rates: (a) 0.1 C, (b) 0.2 C, (c) 0.35 C, and (d) 0.5 C. (The data presented here is the same as shown in Figure S9 but in a different display version for the sake of horizontal comparison between the four graphitic anodes under a specific C rate.)...99

Figure 4-17. The electrochemical performance of DCB full cells assembled using different graphitic materials in cathodes and anodes. (a) The rate performance of DCB full cells. (b) Comparison of the rate performance of DCB full cells from 1 C to 50 C. (c) Cycling performance of DCB full cells under 5 C rate. (d) Comparison of the rate performance of DCB full cells in this study with those in recently published studies. GCD curves of (e) TG and (f) EG full cells at selected cycles from cycling tests under 5 C rate. (g) Ragone plot of TG and EG DCB full cells in this study in comparison with conventional electrochemical energy storage devices and recently reported DCBs. The energy density and power density were calculated based on the total weight of active materials in both the anode and cathode.....100

Figure 4-18. GCD curves of (a) NG and (b) EG full cells at selected cycles from cycling tests under 5 C rate.....102

List of Tables

Table 1-1. A summary and comparison of hydrogen production technologies via steam methane reforming, water electrolysis, and methane pyrolysis. 4

Table 1-2. Comparison of different catalysts for methane pyrolysis, including metal, carbon, and liquid/molten metal catalysts..... 8

Table 3-1. XRF analysis of Fe ore catalyst used for CDM process (left), and XRF analysis of GC ash composition after combustion at 900 ºC for TGA test (right). 46

Table 3-2. A summary of physiochemical properties of carbon materials, the electrical conductivity of EMD/carbon electrodes, and electrolyte absorption capacity of carbon electrodes. 55

Table 4-1. XRF analysis of Fe ore catalyst used for the methane pyrolysis process. 68

Table 4-2. A summary of the physiochemical properties of the graphitic materials used in this study. 79

Table 4-3. XRF analysis of EG (left) and TG (right). 82

Table 4-4. Parameters of EIS spectra for fresh Li/graphite half cells fitted by the equivalent circuit. 92

Table 4-5. Performance comparison of DCBs developed in this work with other recently reported DCBs. 102

Table 4-6. Energy density and power density of TG full cells in this study. 104

Table 4-7. Energy density and power density of EG full cells in this study. 105

Table 4-8. Energy density and power density of TG and EG full cells based on the entire mass of anodes and cathodes. 106

List of Publications

1. **Y. Pan**, L. Cao, Y. Yao, Y. Tao, V. Lo, Z. Zheng, B. Chivers, J. Prabowo, F. Liu, L. Lai, Graphitic Co-Products of Clean Hydrogen Production Enabling High-Rate-Performance Dual-Carbon Batteries, Adv. Energy Mater. (2023) 2300495.
2. **Y. Pan**, V. Lo, L. Cao, A. Roy, B. Chivers, N. Noorbehesht, Y. Yao, J. Wang, L. Wei, Y. Chen, Graphitic carbon from catalytic methane decomposition as efficient conductive additives for zinc-carbon batteries, Carbon 192 (2022) 84-92.
3. D. Zhu, J. Li, Z. Zheng, S. Ye, **Y. Pan**, J. Wu, F. She, L. Lai, Z. Zhou, J. Chen, Water and Salt Concentration-Dependent Electrochemical Performance of Hydrogel Electrolytes in Zinc-Ion Batteries, ACS applied materials & interfaces 16(13) (2024) 16175-16185.
4. Y. Yao, **Y. Pan**, L. Lai, Z. Yu, J. Chen, Y. Yu, T. Darma, Y. Tao, L. Cao, B. Chivers, Carbon/iron co-product from clean hydrogen production as a tri-functional adsorbent and catalyst for efficient wastewater treatment, Applied Catalysis B: Environmental 342 (2024) 123380.
5. Z. Zheng, J. Li, **Y. Pan**, Y. Yu, D. Zhu, J. Prabowo, L. Wei, Y. Chen, Electrolyte additives toward practical aqueous zinc-ion batteries: recent advances and future challenges, Next Energy 1(4) (2023) 100073.
6. Y. Yao, L. Lai, Z. Yu, **Y. Pan**, Y. Yu, V. Lo, A. Roy, B. Chivers, X. Zhong, L. Wei, Carbon/iron by-product from catalytic methane decomposition as recyclable Fenton catalyst for pollutant degradation, Journal of Hazardous Materials 437 (2022) 129328.
7. Y. Yao, **Y. Pan**, Y. Yu, Z. Yu, L. Lai, F. Liu, L. Wei, Y. Chen, Bifunctional catalysts for heterogeneous electro-Fenton processes: a review, Environmental Chemistry Letters 20(6) (2022) 3837-3859.

8. C. Wang, J. Li, Z. Zhou, **Y. Pan**, Z. Yu, Z. Pei, S. Zhao, L. Wei, Y. Chen, Rechargeable zinc-air batteries with neutral electrolytes: Recent advances, challenges, and prospects, EnergyChem 3(4) (2021) 100055.

9. X. Zhang, Z. Pei, C. Wang, Z. Yuan, L. Wei, **Y. Pan**, A. Mahmood, Q. Shao, Y. Chen, Flexible zinc-ion hybrid fiber capacitors with ultrahigh energy density and long cycling life for wearable electronics, Small 15(47) (2019) 1903817.

Chapter 1. Introduction

1.1 Background

Catalytic methane pyrolysis, which directly splits methane (CH_4) into hydrogen (H_2) and solid carbon (C) ($CH_4 \rightarrow 2H_2 + C$), is a promising approach for low-emission hydrogen production. With a mass ratio between H_2 and solid carbon of 1 to 3, large amounts of carbon materials are generated from the process. Developing suitable applications for these large amounts of carbon materials could eliminate waste generation and bring economic benefits to compensate for hydrogen production costs. Currently, there is a lack of studies that evaluated technologically relevant applications for such carbon materials.

The intention of this thesis is to study the graphitic carbon materials produced from the clean hydrogen production process via methane pyrolysis and develop energy storage applications for such carbon materials. Herein, graphitic carbon materials were synthesized from catalytic methane pyrolysis and were further purified by a high-temperature thermal treatment or room-temperature electrochemical purification. A comprehensive set of characterization tools investigated their physiochemical properties. Afterward, essential functions of these graphitic carbon materials for energy storage applications were demonstrated in battery systems, which involved (a) conductive additives in manganese dioxide cathodes for zinc-carbon batteries (Chapter 3), and (b) cathode and anode materials for dual-carbon batteries (Chapter 4). This opens new energy storage applications for these graphitic carbon materials from catalytic methane pyrolysis, benefiting the broader adoption of the clean hydrogen production process via methane pyrolysis.

1.2 Catalytic methane pyrolysis

The global energy sector is dramatically transforming to limit global warming to no more than 1.5 ºC, as laid out in the Paris Agreement, and achieve net zero emissions by 2050 [1-3]. The imperative strengthens the momentum of developing a sustainable energy system to reduce greenhouse gas (GHG) emissions and combat climate change. To achieve the so-called decarbonization, carbon-based fossil fuels are required to be substituted by renewable low-carbon energy sources [4]. Hydrogen is a versatile and clean energy vector that can be directly used via full cells or electricity generation and as an industrial feedstock for ammonia production, petroleum refining, and fertiliser manufacturing [5-8]. The combustion of hydrogen generates higher energy of 142 MJ kg^{-1} on a mass basis than any of the hydrocarbon fuels, which enables hydrogen to hold significant promise in creating a low-carbon energy future [5, 9]. The global demand for hydrogen has grown more than threefold since 1975 to reach 95 million tonnes (Mt) in 2022, and it is expected to reach 115 Mt by 2030 [10-12].

Although hydrogen is a zero-emission fuel, its environmental friendliness also depends on the cleanliness of the production method. **Figure 1-1** shows the global hydrogen production from 2020 to 2022 [13]. It can be seen that the hydrogen production is currently dominated by the unabated use of fossil fuels, with 62% from natural gas, 21% from coal, and 16% produced at refineries and petrochemical industries [13]. These hydrogen production processes inevitably have a considerable environmental impact, emitting around 830 Mt of carbon dioxide (CO_2) annually [14]. By contrast, low-emission hydrogen production is less than 1% of the global hydrogen production, which necessitates the development and promotion of low-emission hydrogen production.

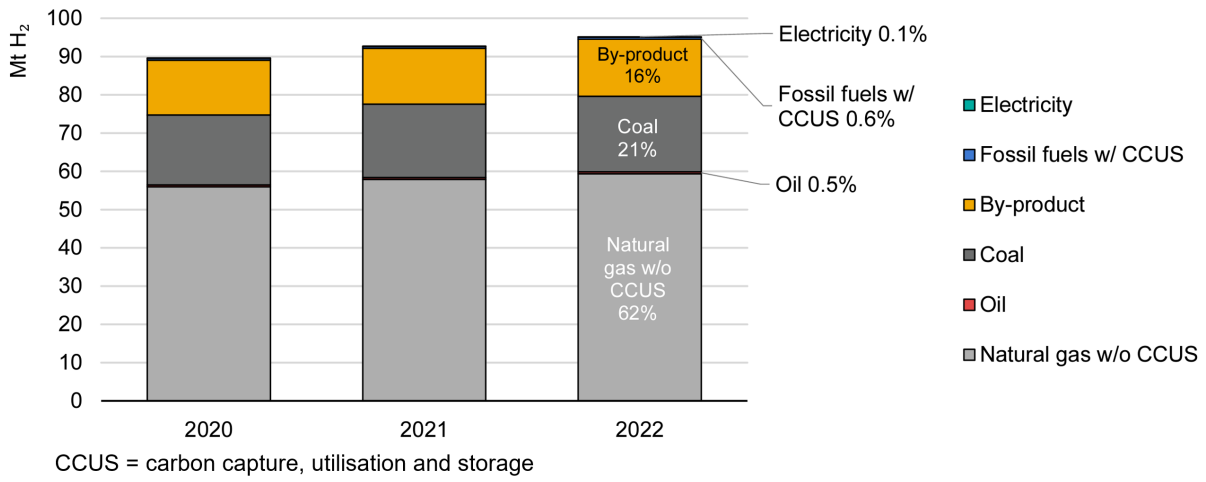

Figure 1-1. Global hydrogen production by technology from 2020 to 2022 [13].

Several hydrogen production technologies have been developed, such as steam methane reforming (SMR), water electrolysis, and methane pyrolysis. Their comparison is summarised in **Table 1-1**. SMR is the dominant process to produce hydrogen today, from which the obtained H_2 is referred to as grey H_2 from fossil fuel with unbated emissions [15]. It is the cheapest way to produce H_2 with a low cost of USD $1-3 per kg of H_2 [13]. However, SMR is reported to have high total emissions of 10-13 kg CO_2 equivalent per kg of H_2 (CO_2-eq/kg H_2) resulted from direct emissions, and upstream and midstream emissions (e.g., production, processing and transport of natural gas, methane emissions from venting or leakages, and emissions related to electricity for compressing natural gas) [13]. Water electrolysis using renewable electricity is a desirable way to produce green H_2 with no direct emissions, while it has a relatively high cost driven by the capital cost and cost of electricity [16]. The emissions from water electrolysis are determined by the emissions of electricity generation and transport. When using grid power, the current global average emission intensity for H_2 is 24 kg CO_2-eq/kg H_2, while in some countries the value could be as low as 0.5 kg CO_2-eq/kg H_2 [13].

Methane pyrolysis, also referred to as the thermal decomposition of methane, which directly splits CH_4 into H_2 and solid carbon (C) ($CH_4 \rightarrow 2H_2 + C$), produces turquoise H_2 with no direct emissions [17]. Since it is an endothermic reaction, thermal input is required for the methane pyrolysis process. When using hydrogen and natural gas as heating sources, the total emissions of the methane pyrolysis process are around 5-6 kg CO_2-eq/kg H_2, and the value could be reduced to 3 kg CO_2-eq/kg H_2 when using renewable electricity [17]. As shown in **Table 1-1**, compared with the conventional SMR technology, methane pyrolysis has a comparable low cost of USD $1.45 per kg of H_2 with lower CO_2 emissions [16]. In addition, the co-produced carbon materials from methane pyrolysis are easy to store and could be marketable, which would bring additional revenue and improve the economics of the methane pyrolysis process [18-20]. Therefore, methane pyrolysis is considered as a promising technology to produce low-emission hydrogen, holding great potential for promoting clean energy transition and fulfilling the growing energy demand [18, 21-23].

Table 1-1. A summary and comparison of hydrogen production technologies via steam methane reforming, water electrolysis, and methane pyrolysis.

Routes	Reaction chemistry	H_2 definition	Cost	Total emissions
Steam methane reforming (SMR)	$CH_4 + 2H_2O \rightarrow CO_2 + 4H_2$	Grey H_2 – fossil fuel with unabated emissions	USD $1-3/kg [13]	10-13 kg CO_2-eq/kg H_2 [13] (12 kg CO_2-eq/kg H_2 [17])
Water electrolysis	$2H_2O \rightarrow O_2 + 2H_2$	Green H_2 – renewable electricity with no direct emissions	USD $3.4-12/kg [13] (with low-emission electricity) (USD $6.16/kg [16])	0.5-24 kg CO_2-eq/kg H_2 [13] (10-460 g CO_2-eq/kWh)

Methane pyrolysis	$CH_4 \rightarrow 2H_2 + C$	Turquoise H_2 – fossil fuel with no direct emissions	USD $1.45/kg [16]	5-6 kg CO_2-eq/kg H_2 [17] (heating source: H_2 or natural gas)

Due to the strong C-H bonds of methane and symmetrical molecular structure, non-catalytic pyrolysis requires high operating temperatures above 1200 ºC to reach a reasonable reaction rate and high hydrogen yield, making this process unfavourable for practical industrial operation [24-26]. The utilization of catalysts could effectively improve the process kinetics and reduce the reaction temperature to under 1000 ºC [11, 18, 27]. For instance, a system using iron oxide as a catalyst was reported to catalytically convert hydrocarbon gas to hydrogen and graphitic carbon at a temperature between 600 and 1000 ºC [28]. **Figure 1-2** depicts a typical setup for the catalytic methane pyrolysis process. Methane gas is introduced as feedstock to a fluidized bed reactor loaded with catalysts and decomposes into hydrogen and solid carbons. The mixing gas of generated hydrogen and unreacted methane subsequently flows through gas separation units, while solid carbon particles are extracted from the bottom of the reactor.

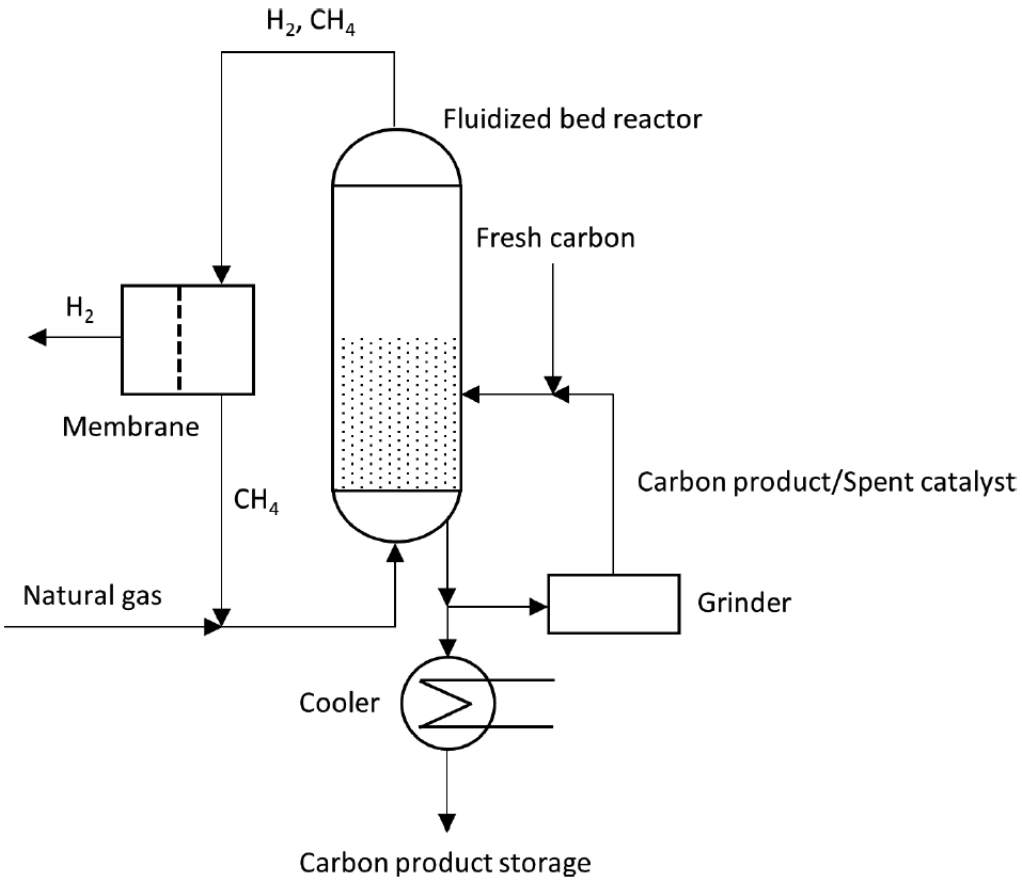

Figure 1-2. A general process of catalytic methane pyrolysis for hydrogen production using a fluidized bed reactor with carbon catalysts [19].

Various studies have been conducted to explore the reaction process of catalytic methane pyrolysis [29-36]. **Figure 1-3** illustrates two commonly accepted reaction process mechanisms: molecular adsorption and dissociative adsorption [18]. During the former process, methane adsorbed on the catalyst surface undergoes dissociation through stepwise surface dehydrogenation reactions. In contrast, methane first dissociates upon adsorption on catalytic active sites to generate chemisorbed CH_3 and H species in the latter process, followed by similar surface dissociation reactions.

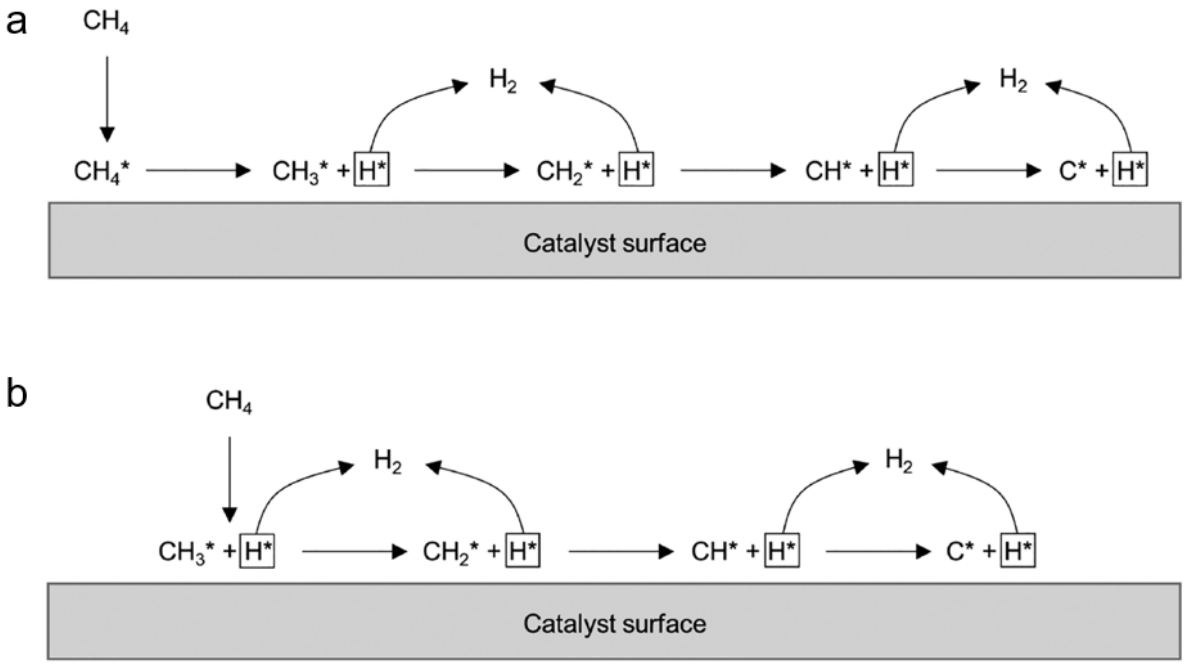

Figure 1-3. Reaction mechanisms for catalytic methane pyrolysis on the catalyst surface, (a) molecular adsorption mechanism, and (b) dissociative adsorption mechanism [18].

Different catalysts have been developed for methane pyrolysis, including solid metal, solid carbon, and liquid/molten metal catalysts, with their comparison summarised in **Table 1-2** [37]. Metal catalysts, typically based on nickel (Ni), iron (Fe) and cobalt (Co), exhibit catalytic activities in the sequence of Ni > Co > Fe [37-39]. Metal catalysts are effective in catalysing the reaction with moderate operating temperature (500-1000 ºC), while the main challenge is the rapid catalyst deactivation resulting from carbon coke coverage on the active sites of the catalyst surface [19, 40]. Despite the highest catalytic activity, Ni-based catalysts are more susceptible to catalyst deactivation [41, 42]. Co-based catalysts have received less attention due to their higher costs and toxicity considerations [43, 44]. Fe-based catalysts, showing lower cost and higher stability at a higher temperature range of 700-1000 ºC, are capable of producing high-quality carbon materials and thus have potential economic benefits [37, 45]. Carbon catalysts based on carbonaceous materials, such as activated carbon, carbon black, and graphite,

are attractive candidates for methane pyrolysis with advantages of low cost, non-toxicity, resistance to high temperature, and tolerance to impurities like sulfur compounds [17, 46-48]. However, carbon-based catalysts commonly show much lower activities than metal catalysts, leading to higher reaction temperatures (800-1100 ºC) necessary for obtaining reasonable hydrogen yields [17, 19, 49]. Additionally, liquid catalysts and liquid heat transfer media such as molten metals (e.g., Pb, Sn, or Bi), molten metal alloys (e.g., Ni-Bi, or Cu-Bi), and molten salts (e.g., KBr, NaBr, NaCl, NaF, $MnCl_2$ or KCl) have been studied to separate hydrogen and solid carbon from the surface of molten media, resulting in the prevention of carbon deposition on the catalyst and the consequent catalyst deactivation [11, 50, 51]. The main drawbacks of liquid catalyst systems are low catalytic activity and high required temperature (>1000 ºC) to achieve high conversions, which limit its applicability on an industrial scale [19, 24].

Table 1-2. Comparison of different catalysts for methane pyrolysis, including metal, carbon, and liquid/molten metal catalysts.

Catalysts	Advantages	Disadvantages
Metal (i.e., Ni, Fe, Co)	High catalytic activity (Ni>Co>Fe) Moderate operating temperature (500-1000 ºC) [40]	Rapid catalyst deactivation Co-based: high cost and toxicity issues
Carbon (i.e., activated carbon, carbon black)	Relatively low cost High-temperature resistance and good stability Non-toxicity Tolerance to impurities like sulfur compounds	Limited catalytic activity Relatively high reaction temperatures (800-1100 ºC) [19]
Liquid/molten metal (i.e., Pb, Sn, Bi, Ni-Bi, Cu-Bi)	Prevention of catalyst deactivation	Low catalytic activity High required temperature (>1000 ºC) [19]

1.3 Carbon materials from catalytic methane pyrolysis

1.3.1 Different co-produced carbon materials

The solid carbon materials generated from catalytic methane pyrolysis display varied carbon structures ranging from amorphous carbon black, ordered graphitic materials to highly specialized carbon nanotubes and fibres [23]. The characteristics of the co-produced carbon are influenced by multiple factors involving catalyst species, compositions, size of catalyst particles, and reaction conditions [52].

Generally, the use of metal catalysts is favourable for the formation of ordered nanocarbons, such as carbon nanotubes and nanofibres [19, 53, 54]. In this case, the vapor-liquid-solid (VLS) mechanism is proposed to account for the growth of such filamentous carbon materials, carbon nanotubes and nanofibres, in the presence of metal catalysts [18, 55, 56]. As outlined in **Figure 1-4**, elemental carbon species are generated from the dissociation of absorbed hydrocarbon on the catalyst surface, followed by the diffusion of carbon species through the metal particle and precipitation at the back face of the catalyst particle. Carbon species accumulated at the exposed catalyst surface gradually cover the catalyst particle and drive the particle away from the catalyst support, forming carbon filaments. The reaction temperature affects the size of carbon filaments, with higher operating temperatures resulting in decreased diameter and length [57].

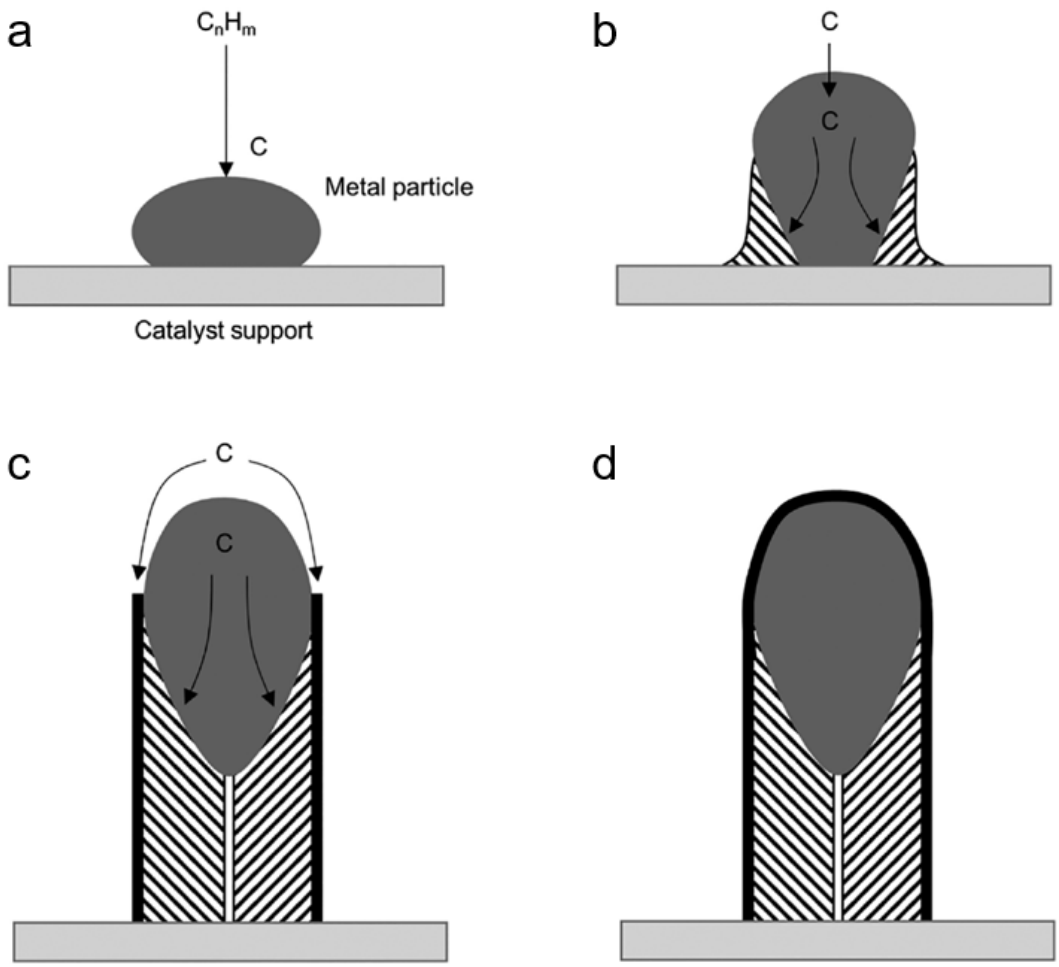

Figure 1-4. Vapor-liquid-solid (VLS) mechanism for the catalytic growth of filamentous carbon on metal catalysts [18].

Despite carbon filaments, carbon nano-onions (CNOs) are another carbon material obtained from the methane pyrolysis process when applying metal catalysts [58-62]. CNOs are quasi-spherical nanoparticles composed of concentric graphite shells, forming an onion-like graphite structure. **Figure 1-5** depicts the growth mechanism proposed for two types of CNOs, one encapsulating a metal particle as a core and the other with a hollow core [59, 63]. Methane molecules are first adsorbed to the catalyst particles from multiple directions and decompose into hydrogen and carbon. Carbons deposit around the surface of catalyst particles and form

graphitic layers accumulating on the catalyst surface, resulting in the growth of graphitic shells encapsulating the metal particle as a core. For CNOs with an empty core, the process of carbon shells surrounding the catalyst particles in the initial periods happens in a similar manner as for CNOs with a metal particle core. During the formation of carbon onion, some small metal particles with nanometer sizes are liquefied at high temperatures and gradually evaporate through the defects of the graphitic layers, leading to the hollow structure of CNOs [59]. High reaction temperatures (e.g., above 800 ^{o}C) are more likely to produce CNOs, while lower temperatures tend to attain more thin-walled carbon nanotubes [64]. Additionally, elevated reaction temperatures benefit the synthesis of nanocarbons with higher crystallinity and graphitization degree [65].

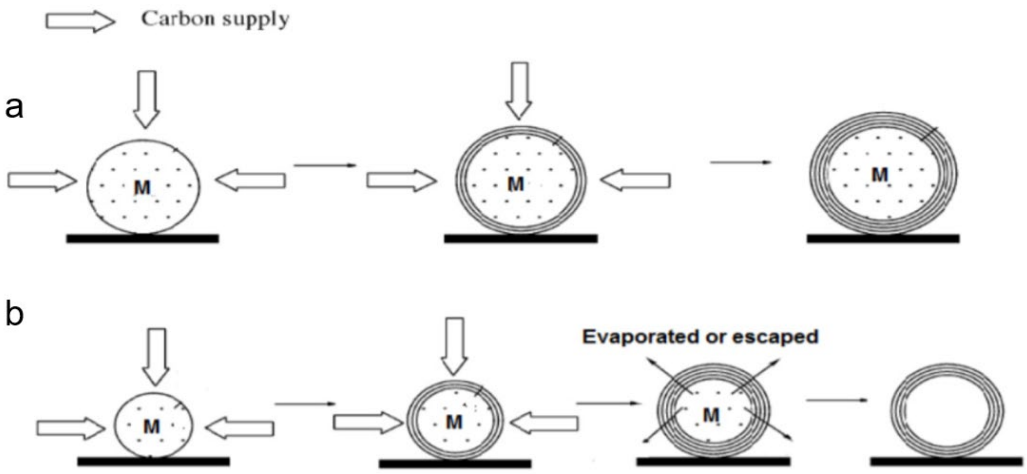

Figure 1-5. The formation mechanisms for carbon nano-onions (CNOs): (a) CNOs with a metal particle core and (b) CNOs with an empty core [63].

In the carbon-catalysed methane pyrolysis process, carbon materials with different morphologies are obtained, dependent on the nature of the catalysts [66, 67]. The formation of carbon black occurs over activated carbon catalysts, and the generation of amorphous

turbostratic carbon is observed when carbon black and graphite are catalysts. Using carbon nanotubes as catalysts enhances the growth of extra layers over the walls, thus yielding multi-walled carbon nanotubes [53]. Although various carbon materials have been explored as catalysts for the methane pyrolysis process, comprehensive mechanism studies on this process over carbon catalysts are still lacking. It is proposed that potential active sites on carbon catalysts involve defects, dislocations, vacancies, surface functional groups on carbon nanosheet edges and basal planes, as well as non-metallic heteroatoms such as O, H, N, and S [37, 52].

1.3.2 Applications of carbon materials from catalytic methane pyrolysis

Based on the endothermic reaction of the methane pyrolysis process ($CH_4 \rightarrow 2H_2 + C$), the mass ratio between hydrogen and solid carbon co-products is 1 to 3. Thus, even a small industrial-scale hydrogen production facility based on catalytic methane pyrolysis would generate thousands of tons of carbon materials. Supposing catalytic methane pyrolysis accounts for 1 % of the global hydrogen production, 2.82 Mt of carbon materials could be formed, significantly impacting the global carbon material market [52]. Developing value-added applications for these large amounts of carbon materials could eliminate waste generation and bring economic benefits to compensate for the hydrogen production cost of the methane pyrolysis process.

Carbon materials with different structures co-produced from the catalytic methane pyrolysis mainly include carbon black, carbon fibre and carbon nanotubes. The carbon co-products are required to fulfill the relevant requirements and specifications on diverse properties before being applied to existing markets. Approximately 90 % of the carbon black produced is used in rubber applications, primarily as a filler and a reinforcing agent for tires,

9 % as a pigment, and the remaining 1 % in other applications [68]. The rubber-grade carbon black requires certifications as either American Society for Testing and Materials (ASTM) or Specialty Grade, and some other grades of carbon black are authenticated by the U.S. Food and Drug Administration before using in items such as coffee mugs, food trays, and cutlery [40]. The price of carbon black materials is determined by the product specifications, ranging from US$400 to over US$1,000 per ton for ASTM-grade carbon black and exceeding US$2,000 per ton for specialty-grade carbon black [40]. Currently marketed carbon fibre and carbon nanotubes are both high-value materials. Carbon fibre materials have been used in a variety of applications, including aerospace, automobiles, sports and leisure, the chemical industry, carbon-reinforced composite materials and textiles, with the price varying from US$25,000 to US$113,000 per ton depending on the utilization [40, 69, 70]. Carbon nanotubes have a highest selling price of US$600 per gram and are utilized in polymers, electronics, plastics, and energy storage fields [40].

Even though some commercial carbon materials have high commodity value, the structural and purity control strategies to produce desirable carbon via catalytic methane pyrolysis are still limited [52]. Moreover, if hydrogen production from catalytic methane pyrolysis is implemented industrially, none of the existing markets will be able to accommodate the substantial amounts of carbon [18, 19]. Only a few studies have evaluated technologically relevant applications of carbon materials from catalytic methane pyrolysis [71-73]. Therefore, further investigations are required to validate the suitability of carbon co-products from the methane pyrolysis process for relevant scenarios and develop potential value-added applications to enhance the economic viability of this hydrogen production process.

1.4 Carbon materials in batteries

To develop energy storage applications for the carbon materials from methane pyrolysis, a deep understanding of the crucial roles of carbon materials in electrochemical energy storage devices is demanded. In this section, the two essential functions of common carbon materials for battery applications are studied, including conductive additives, and electrode active materials.

1.4.1 Conductive additives

The earliest practical application of carbon materials in electrochemical energy storage (EES) devices can be dated back to 1868, demonstrated by Georges Leclanché in cells bearing his name, as illustrated in **Figure 1-6** [74, 75]. The Leclanché cell is composed of zinc acting as a negative electrode or anode, ammonium chloride solution as an electrolyte, and a mixture of manganese dioxide (MnO_2) and powdered carbon with equal volume as a positive electrode or cathode. Since manganese dioxide, the active material of the cathode is a poor electrical conductor, carbon is added as a conductive additive to enhance the electrical conductivity of the electrode. Desirable carbon materials for conductive additive applications should fulfill the requirements in four aspects: (a) low resistivity in the presence of the electrolyte and active electrode material, (b) low impurity compositions, (c) capability to absorb and retain a considerable amount of electrolyte without sacrificing the ability to mix with the active material, and (d) compressibility and elasticity during electrode processing and battery assembly [76]. This system's commonly used carbon conductive additives are graphite and acetylene black. Graphite was once used as the principal conductive media but has been partially replaced by acetylene black due to the ability of acetylene black to hold more electrolytes [75]. Eventually, the Leclanché system was continually improved and evolved into today's zinc-carbon batteries,

among the most widely used primary batteries worldwide with a continuously growing global market [75].

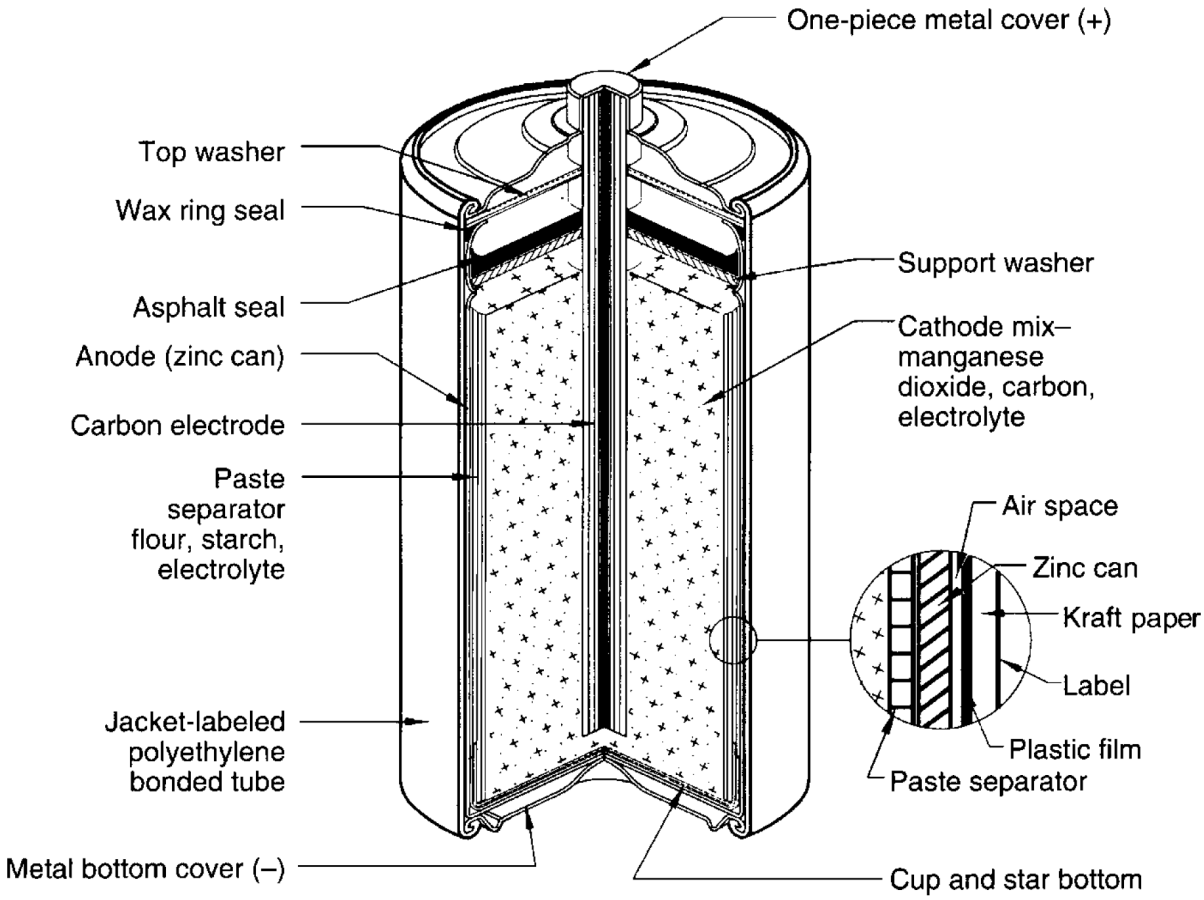

Figure 1-6. Schematic figure of a cylindrical Leclanché battery in a cutaway view [75].

With the continual development of energy storage technologies, advanced EES systems are emerging, promoting the research interests and applications of carbon materials as conductive additives. When carbon materials are applied as conductive additives to noncarbon cathodes or anodes, forming an interface between carbons and active materials impacts the electrochemical process and is essential for building high-performance EES systems [77]. Various carbon materials have been explored as conductive additives, undergoing different

contact modes with the active materials depending on their dimensionality, as illustrated in **Figure 1-7** [78, 79]. Carbon black and conducting graphite particles are zero-dimensional (0D, sphere type) carbon materials that served as conventional carbon additives, delivering a "point-to-point" contact mode. One-dimensional (1D, line or tube type) and two-dimensional (2D, plane type) carbon materials are great candidates, exhibiting essential properties for conductive additives, high conductivity, large surface area, and good flexibility [78]. The intrinsic electrical conductivity of carbon materials contributes to improving the conductivity of electrodes; meanwhile, increasing the contact area between carbon additives and active materials decreases the interparticle resistance and thus enhances the electron transfer efficiency, leading to better electronic conduction [78]. Consequently, 1D carbon nanotubes work on a "line-to-point" contact mode, and 2D carbon materials like graphene present a "plane-to-point" contact mode, both superior to the conventional "point-to-point" mode. The combination of carbon materials with different dimensions can construct multi-level conductive networks by multiple contact modes with active materials. Several binary conductive additives have been developed based on this dimensionality integration strategy. 0D carbon black (Super P) mixed with 1D carbon fibres forms a well-connected conductive network inside the electrode, lowering the electron conducting resistance and facilitating electron transfer [80]. Hence, lithium nickel manganese cobalt oxides (NCM) cathodes with this binary conductive additive have higher electrical conductivities compared to those with a single type of additives owing to the synergistic effect of two carbon additives [80]. Another hybrid conductive additive composed of 2D graphene and 0D carbon black simultaneously builds both "long-range" and "short-range" conductive networks among the electrode, resulting in a higher specific capacity of lithium iron phosphate ($LiFePO_4$) cathode with the binary conductive additive than that solely used carbon black [78, 81]. In addition, aligning 1D carbon nanotubes between 2D graphene nanosheets is proposed to establish a sandwich-like

hierarchical structure with efficient three-dimensional (3D) electron transfer pathways and ion diffusion channels [82].

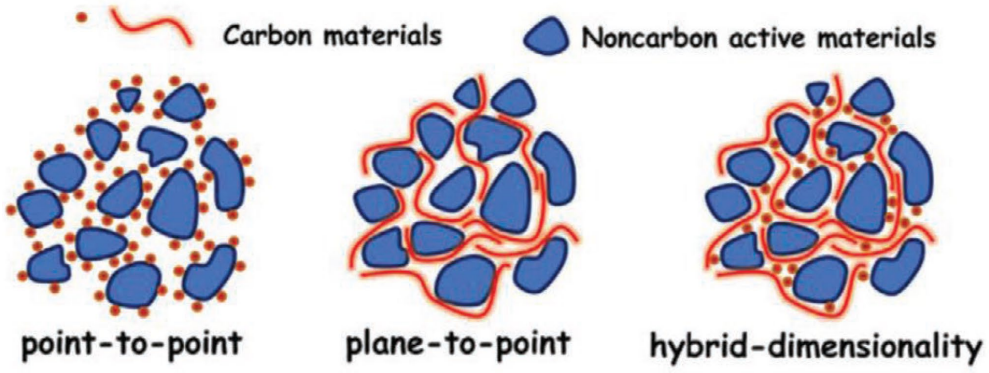

Figure 1-7. Schematic illustration of typical conducting models of carbon materials as conductive additives, from left to right: point-to-point mode, plane-to-point mode, and hybrid-dimensionality mode [78].

1.4.2 Electrode active materials

Carbon materials have a long history of being used as active materials in electrodes for various batteries due to their excellent chemical stability, good electrical conductivity, unique structure, and abundance of sources [77, 83, 84]. Since being first commercialized by Sony Corporation in 1991, lithium-ion batteries (LIBs) have been on the market for over thirty years and have been successfully used in powering portable electronic devices, electric vehicles, and smart electric grids [85, 86]. Graphite materials are the oldest and one of the most common active materials in the anode electrodes for LIBs, serving as a host for the intercalation of lithium cations. As shown in **Figure 1-8**a, with a 3D crystal structure stacked by layers composed of sp^2 hybridized carbon, graphite has an interlayer spacing of 0.335 nm, suitable for accommodating guest intercalation ions (e.g., lithium cations) [86]. The high in-plane

conductivity of graphite originating from delocalized p-bonds is also vital to the success of LIBs, guaranteeing fast contact between electron carriers and the intercalated ions. However, one drawback of graphite acting as active material in the anode is the sluggish interfacial kinetics, causing voltage drop under fast charging conditions and undesirable plating of metallic lithium on a graphite surface, which further leads to capacity fading and short-circuiting of LIBs [87-89]. Several graphite modification techniques are developed to improve the charging of graphite anodes, such as acid-base treatment and high-temperature expansion [90-94]. After being etched by potassium hydroxide (KOH) at a high temperature of 800 ºC, the modified graphite exhibits multichannel structures with surface holes, which creates de-/intercalation sites for lithium ions, decreases diffusion distance of lithium ions and, thus, facilitates the diffusion kinetics [94].

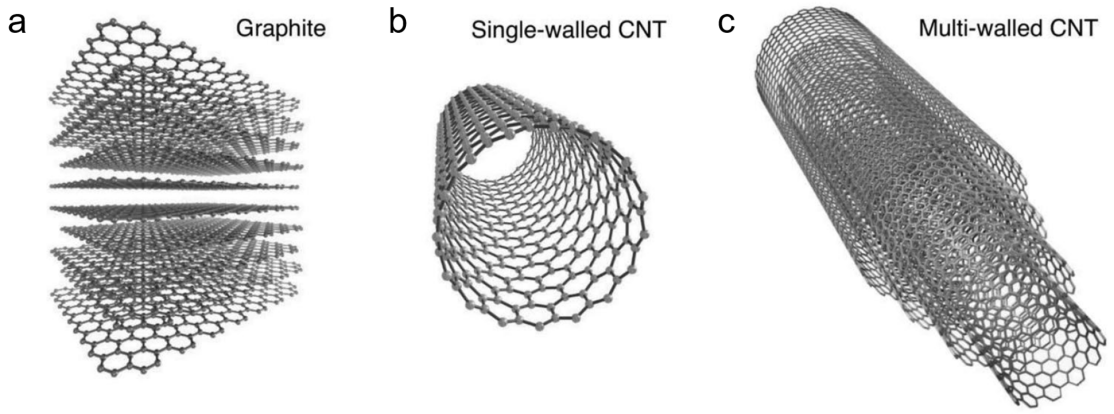

Figure 1-8. Structures of typical carbon materials: (a) graphite, (b) single-walled carbon nanotubes, and (c) multi-walled carbon nanotubes [95].

Beyond graphite, other carbon materials, such as carbon nanotubes and graphene materials, have been studied as active materials over the past thirty years [77]. As discovered in 1991 by Iijima, carbon nanotubes are hollow cylinders composed of roll-up single or multiple graphene

sheets, classified into single-walled and multi-walled carbon nanotubes, respectively (**Figure 1-8**b and c) [96, 97]. Owing to their desirable properties of ultrahigh electrical conductivity (up to 5000 S cm^{-1}), large specific surface area (up to 1300 m^2 g^{-1}), mesoporosity, and considerable charge transport mobility (over 10^5 cm^2 V^{-1} s^{-1}), carbon nanotubes are regarded as attractive candidate materials for anode electrodes in LIBs [77, 86, 98-103]. There have been several studies on the successful electrochemical intercalation of lithium in carbon nanotubes [104-113]. The reported reversible capacities for carbon nanotubes in LIBs vary from 350 to 680 mAh g^{-1}, higher than the theoretical maximum value of conventional graphite active materials (372 mAh g^{-1}), which attests the promise of using carbon nanotubes for LIB electrodes. The storage of lithium cations in carbon nanotubes is proposed to take place in their central core, the interlayer space of multi-walled carbon nanotubes, and the space between nanotubes when fabricated as carbon nanotube bundles [102, 114]. In addition, both the interior and exterior (outside walls) of carbon nanotubes are found to be electrochemically active sites for the intercalation and absorption of lithium cations [115]. The electrochemical responses of carbon nanotubes are intimately associated with their morphologies. The capacity of carbon nanotubes could be further increased by mechanical or chemical treatments, such as ball milling, chemical etching and nitrogen doping [104, 116-122]. Gao et al. reported that the reversible capacity of single-walled carbon nanotubes was increased from 600 mAh g^{-1} to 1000 mAh g^{-1} after ball milling [104], and Shimoda et al. achieved a reversible capacity of 700 mAh g^{-1} for single-walled carbon nanotubes after chemical etching by strong acids [116]. Li et al. found that nitrogen-doped carbon nanotubes with higher nitrogen content (9.6 wt%) delivered improved reversible capacities of 723 mAh g^{-1} after 200 cycles [122]. These approaches open the tubes and/or introduce defects to carbon nanotubes, increasing active sites for lithium adsorption and thus contributing to capacity improvements.

As a 2D carbon-based material, graphene is an attractive candidate for active materials owing to its high electrical conductivity, large surface area, and good electrochemical stability [123-127]. Graphene nanosheet electrodes were first employed for lithium storage in 2008, achieving a specific capacity of 540 mAh g^{-1} [128]. The capacity of graphene electrodes was further increased up to 730 and 784 mAh g^{-1} when incorporating carbon nanotubes and fullerenes, respectively [128]. The actual capacity of graphene electrodes (e.g., 540 mAh g^{-1}) is lower than its theoretical value of 744 mAh g^{-1}, ascribed to graphene sheets' restacking [77, 129, 130]. The issue of graphene sheet restacking reduces the active sites for lithium absorption, thus causing a decrease in available capacity [131]. Introducing functional groups and structural defects to graphene materials is beneficial for capacity improvements, which increase the active sites of graphene for lithium absorption and facilitate the diffusion of lithium ions on graphene planes [132-134]. Other effective strategies have been developed, such as forming hybrid materials with metal oxide and controlling the formation of layered structures in graphene [135-141].

Graphdiyne is another 2D carbon material and was first synthesized in 2010 by Li et al. [142]. Graphdiyne is a carbon allotrope with one-atom thick layer of strongly-bonded sp^2- and sp-hybridized carbon atoms. With the combination of sp^2 and sp carbon network, graphdiyne exhibits super-large conjugated structure, abundant carbon chemical bonds, natural pores, excellent chemical and mechanical stability, and high electron mobility (up to 10^5 cm^2 V^{-1} s^{-1}) [143-148]. Several simulation studies have demonstrated graphdiyne as a good electrode material for lithium intercalation, with a theoretical capacity of 744 mAh g^{-1} for lithium storage and multilayer theoretical capacity up to 1117 mAh g^{-1} [149-152]. The lithium storage in multilayer graphdiyne was reported to happen through the interlayer insertion/extraction and surface absorption/desorption methods, with a reversible capacity of 520 mAh g^{-1} at 0.5 A g^{-1} [153]. Shang et al. demonstrated ultrathin graphdiyne nanosheest as a high-performance LIB

anode, delivering a high capacity of 1388 mAh g^{-1} and good rate performance of 870 mAh g^{-1} at 10 A g^{-1} [154]. Zhang et al. found that the nitrogen doping of graphdiyne increased its reversible capacity for lithium storage from 584 mAh g^{-1} to 785 mAh g^{-1} [155].

1.5 Thesis scope

This thesis is composed of 5 chapters, which are listed below.

Chapter 1 first introduces the importance of hydrogen as a clean energy vector to the global energy transition toward low-carbon energy future, and the sustainability of catalytic methane pyrolysis as an attractive approach producing hydrogen with no direct emissions of carbon dioxide. Developing value-added applications to accommodate the large amounts of carbon materials co-produced from methane pyrolysis is of great significance to push forward this clean hydrogen production process, embodied as eliminating waste generation, bringing additional revenue, and improving economic viability. Two essential roles carbon materials play in batteries are then studied: conductive additives in electrodes and active materials for electrodes, which potentially offer new pathways to employ these carbon co-products in energy storage applications.

Chapter 2 gives a comprehensive study of the most commonly used techniques for characterizing carbon materials, determining their physiochemical properties, and evaluating their electrochemical performances. Various analytical techniques, including SEM, TEM, XRD, nitrogen physisorption, Raman, XPS, and TGA, are applied to obtain diverse information for carbon materials, such as morphology, crystal structure, surface area, pore structure, chemical composition, defect level, surface functional groups, purity, and thermal stability. The processes for electrode fabrication and coin cell assembly are discussed, followed by the study of commonly used electrochemical characterization techniques, such as linear sweep

voltammetry and cyclic voltammetry, electrochemical impedance spectroscopy, and galvanostatic charge–discharge measurements.

Chapter 3 presents the graphitic carbon materials from the catalytic methane pyrolysis process working as efficient carbon conductive additives for zinc-carbon batteries. Graphitic carbon materials are synthesized as co-products from methane pyrolysis using Fe ore catalysts and purified by the standard high-temperature thermal treatment and the alternative electrochemical method. MnO_2 cathodes containing purified carbon materials as conductive additives present two essential properties: high conductivity (98 S cm^{-1}) and good electrolyte absorption capabilities (4.2 mg mg^{-1}). Zinc-carbon batteries assembled using these carbon materials show the advantages of higher electrode conductivity, larger specific capacity under higher current densities, better rate performance, lower internal resistance, and superior long-term stability compared with commercial carbon conductive additives (Super P).

Chapter 4 demonstrates the graphitic carbon co-products from methane pyrolysis can work as active materials for both cathodes and anodes to enable high-rate-performance dual-carbon batteries, outperforming commercial natural and synthetic graphite. Compared to graphite, the smaller crystalline sizes and larger surface areas of the purified graphitic carbon materials from methane pyrolysis are favourable for faster surface redox reactions and better structural stability upon electrolyte ion intercalation. Consequently, dual-carbon batteries assembled with purified graphitic carbon delivery high capacity retention of 93.4 % after high-rate charge/discharge over 5000 mA g^{-1}, excellent cycling stability of 300 cycles without capacity decay at 500 mA g^{-1}, and great energy density of 168.7 Wh kg^{-1} at power density of 10.6 kW kg^{-1}, outperforming recently reported dual-carbon batteries.

Chapter 5 summarises the findings in this thesis and discusses future developing directions, such as optimising the synthesis of graphitic carbon co-products from catalytic methane

pyrolysis, modifying these carbon materials for performance enhancement, and developing suitable applications in more energy storage systems.

Chapter 2. Characterization techniques of carbon materials

2.1 Carbon materials preparation

The graphitic carbon materials used in this thesis were prepared from the catalytic methane pyrolysis process using a low-cost Fe ore catalyst in a fluidized bed reactor. It is noted that a general introduction of the process is given here for the preparation of carbon materials, and the detailed synthesis and purification processes of specific graphitic carbon materials are discussed in the research chapter 3 and 4. As illustrated in **Figure 2-1**, during this process, methane molecules interacted with the suspended catalyst particles and decomposed into H_2 and carbon. With the deposition of solid carbon, catalyst particles disintegrated into nano-fragments with lower density and were carried out of the reactor. These solid graphitic carbon materials encapsulating Fe particles were collected for studies.

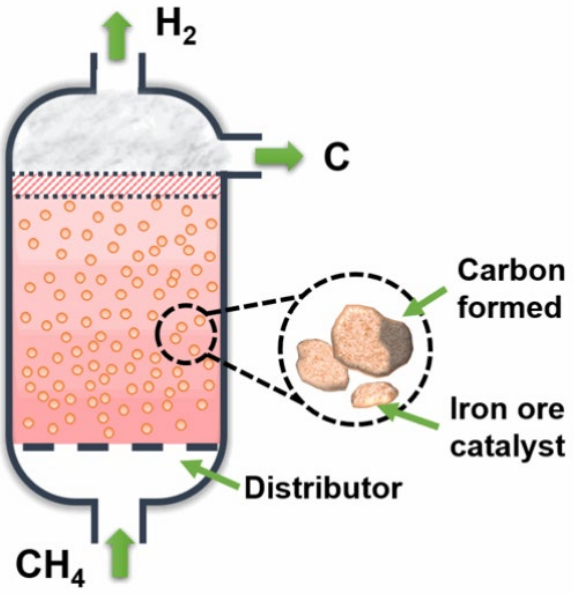

Figure 2-1. Schematic illustration of the synthesis of graphitic carbon materials from catalytic methane pyrolysis process using Fe ore catalysts.

2.2 Scanning electron microscopy (SEM)

Scanning electron microscopy (SEM) is the most widely used type of electron microscope, examining the microscopic structure by scanning the surface of materials. The basic components of a scanning electron microscope include an electron gun and a series of electromagnetic lenses and apertures, as depicted in **Figure 2-2**a [156]. In SEM, an acceleration voltage generally in the 1-40 kV range is applied to an electron-emitting filament typically made of tungsten (W) or hexaboride (LaB_6) to generate an electron beam. After being collimated and focused by condenser lenses and objective lenses, the electrons raster-scan over the sample by scanning coils and interact with the top few nanometers to microns regions of the sample. Secondary electrons emitting from the sample surface exhibit low energy and are then collected, amplified, and stored by a detector. Samples for SEM are required to be electrically conducting; otherwise, a thin metal layer is necessary to enclose samples to prevent electric charging [157].

SEM is commonly employed to characterize carbon materials, delivering information such as the surface morphology and nanostructures of carbon materials and cross-sectional observations [157, 158]. The SEM images of several typical carbon materials are shown in **Figure 2-2**b [159]. Rough surface morphologies are detected for activated carbon, carbon black, and mesoporous carbon, while filamentous structures with smooth surfaces are obtained for carbon nanofibre and multi-walled carbon nanotubes. Additionally, layered carbon structures could be observed for graphite and graphene nanoplatelets.

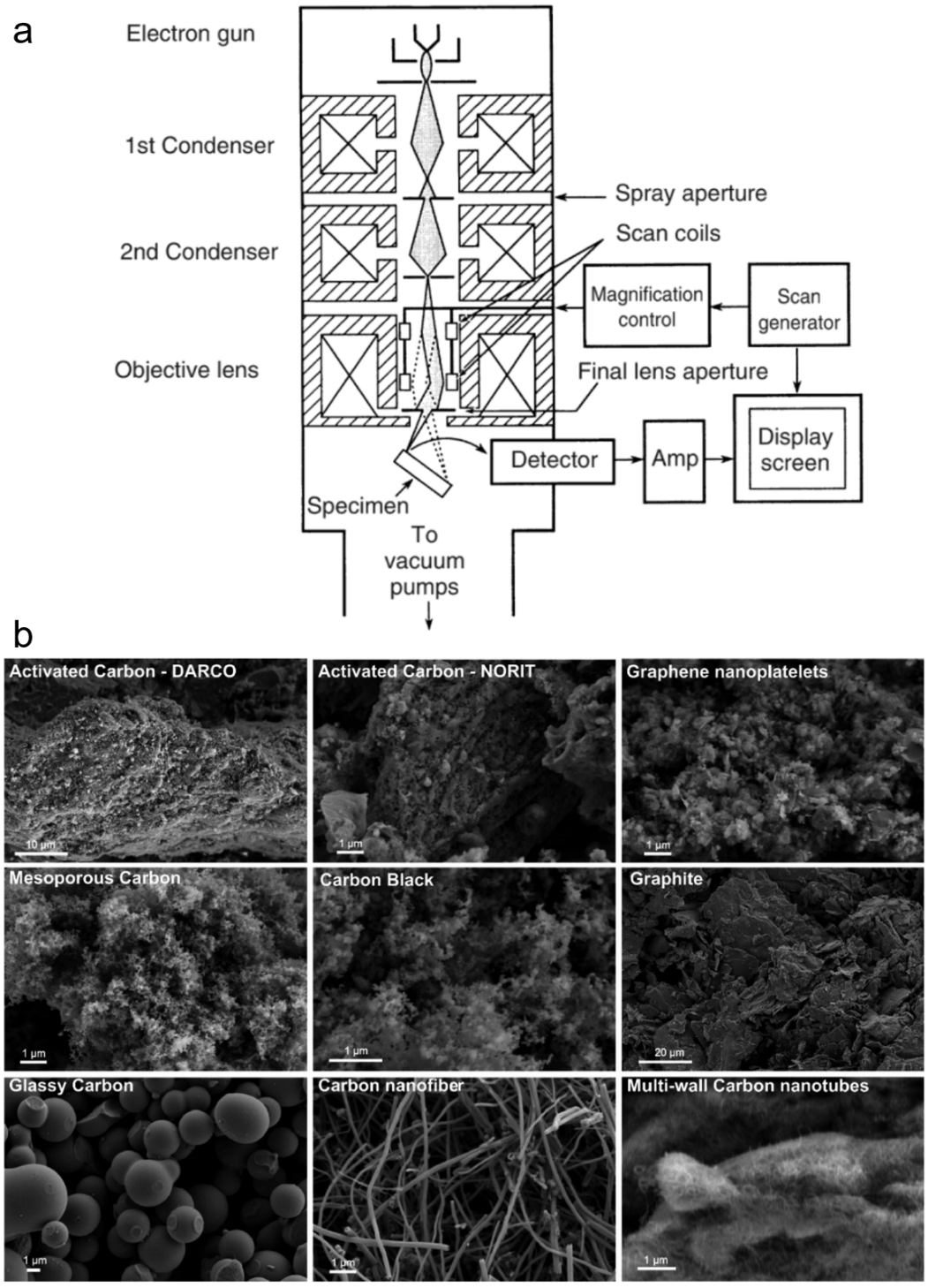

Figure 2-2. (a) Schematic diagram of the basic components of a scanning electron microscope [156]. (b) SEM images of typical carbon materials [159].

2.3 Transmission electron microscopy (TEM)

Transmission electron microscopy (TEM) has been widely used when the measurements require high resolution, capable of reaching atomic resolution at a goal of 1 nm. As shown in **Figure 2-3**a, TEM performs under a similar basic principle as a transmission light microscope but uses electrons instead of visible light [160]. A transmission electron microscope consists of an electron source, a specimen stage, and a series of electromagnetic lenses. For TEM, a high acceleration voltage of above 100 kV (usually 200 kV) is applied to generate electrons with an extremely short wavelength, leading to a high-resolution microscope [156]. Since electrons cannot move in the atmosphere, a vacuum environment generally above 10^{-5} Pa is required for the chamber of TEM [160].

TEM provides high-resolution information about the morphology and crystallography of carbon materials, which is particularly useful for examining nanostructured carbon materials [161]. For instance, as illustrated in **Figure 2-3**b, TEM was applied to characterize synthesized graphitic carbon nanofibres, showing the hollow-tunnel and graphitic structure of carbon materials, and further used for the determination of the interlayer spacing of the graphene sheets [162].

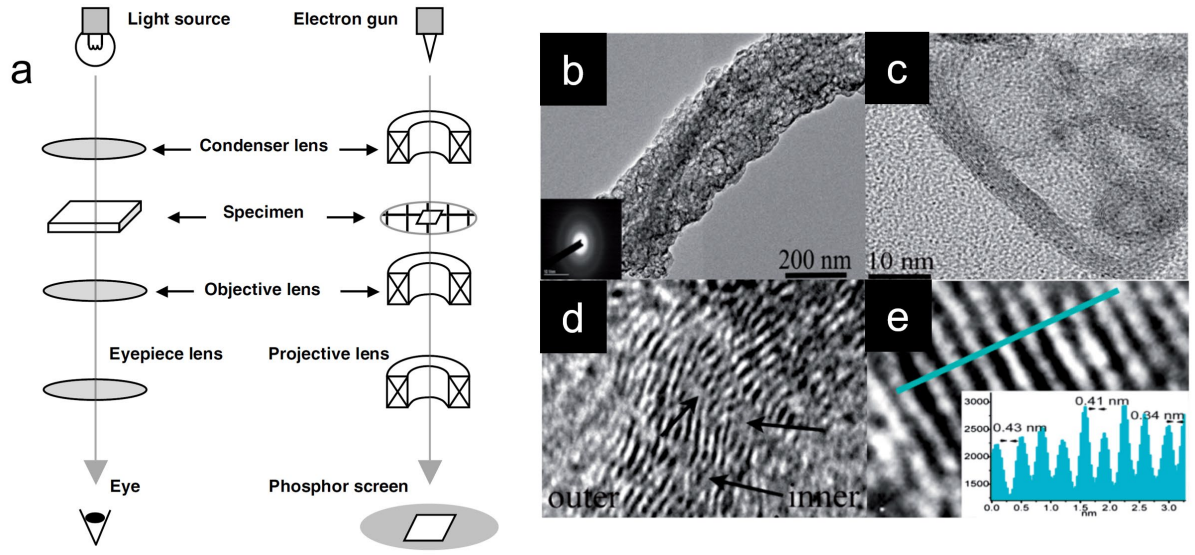

Figure 2-3. (a) Schematic illustrations of a light microscope (left) and a transmission electron microscope [160]. TEM images of graphitic carbon nanofibres, (b) hollow-tunnel structures, (c) walls of the hollow structures, (d) graphene sheets and (e) determination of interlayer spacing of graphene sheets [162].

2.4 X-ray diffraction (XRD)

X-ray diffraction (XRD) is the most effective technique for determining the crystal structure of carbon materials. The basic components of an X-ray diffractometer contain an X-ray source, specimen, and detector, with their geometrical arrangement demonstrated in **Figure 2-4**a [156]. An X-ray beam produced from an X-ray tube passes through special splits and strikes the specimen. The X-ray beam diffracted by the specimen becomes a convergent beam at the receiving slits and is collected by a detector. Movements among the three components are applied to record the diffraction intensity in a range of the diffraction angle (2θ), where θ represents the angle between incident beam and the crystallographic plane that generates diffraction [156].

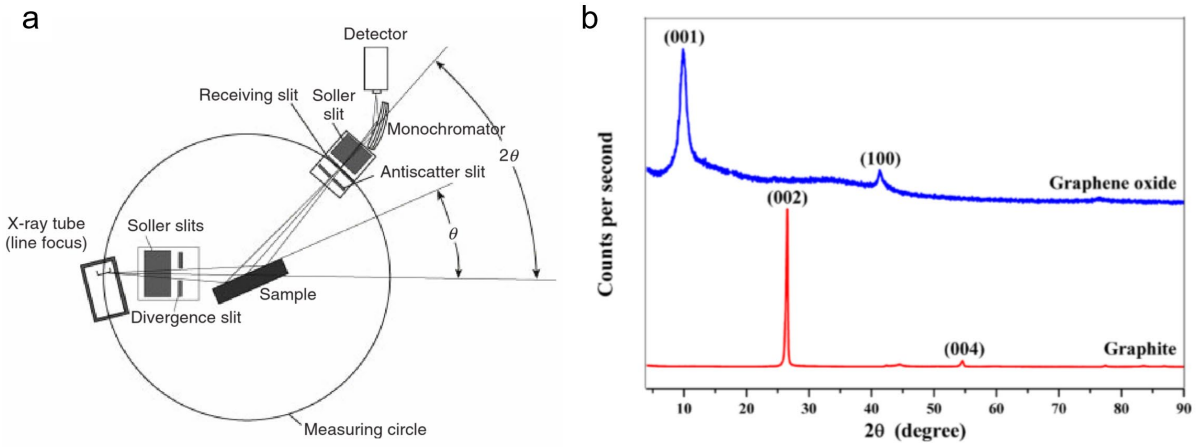

Figure 2-4. (a) Basic components of an X-ray diffractometer and their geometric arrangement [156]. (b) XRD profiles of pure graphite and synthesized graphene oxide [163].

Practically, the XRD patterns of pure graphite and synthesized graphene oxide materials are shown in **Figure 2-4**b [163]. Pure graphite presents two characteristic peaks centred at 2θ=26.5° and 2θ=54.5°, corresponding to the (002) and (004) graphitic planes, respectively. The deviation of (002) peak into two peaks at 9.9° and 42.0° reveals the successful synthesis of graphite oxide. In addition to identifying certain carbon materials, XRD could be used to determine the crystalline information of carbon materials. The interlayer spacing between the graphene sheets (d_{002}) could be calculated using Bragg's equation:

$$2d \sin\theta = n\lambda$$

where θ is the peak position, n is the order of diffraction, and λ is the wavelength of the incident X-ray [164]. The apparent crystalline length and thickness could be estimated using the Scherrer equation:

$$L = \frac{K\lambda}{\beta \cos\theta}$$

where β is the full width at half-maximum of the XRD peaks and K represents the Scherrer constant [164].

2.5 Nitrogen (N_2) physisorption technique

Nitrogen (N_2) physisorption has been widely used to analyse carbon materials, determining their specific surface area and pore size distribution. **Figure 2-5** depicts the components of a physical adsorption analyser used for nitrogen physisorption [165]. The principle of this device is based on measuring the adsorption of nitrogen gas at 77 K (-195.79 ºC) on the material surface. After introducing a known amount of nitrogen into the sample tube, the pressure inside the tube decreases due to gas adsorbing on the surface of the sample material. The surface adsorption capacity of nitrogen in a solid surface depends on the nitrogen-relative pressure (P/P_0), where P is the partial pressure of nitrogen, and P_0 is the saturated nitrogen vapour under the temperature of liquid nitrogen (77 K). With P/P_0 in the range of 0.05 to 0.35, brunauer, emmett and teller (BET) equations are suitable for fitting adsorption and the relative pressure, thus determining the specific surface area of carbon materials [166]. Pore size distribution could be obtained through a theoretical model, which gives information on the pore structure with different sizes in carbon materials, such as micropores (<2 nm), mesopores (2-50 nm), and macropores (>50 nm) [167].

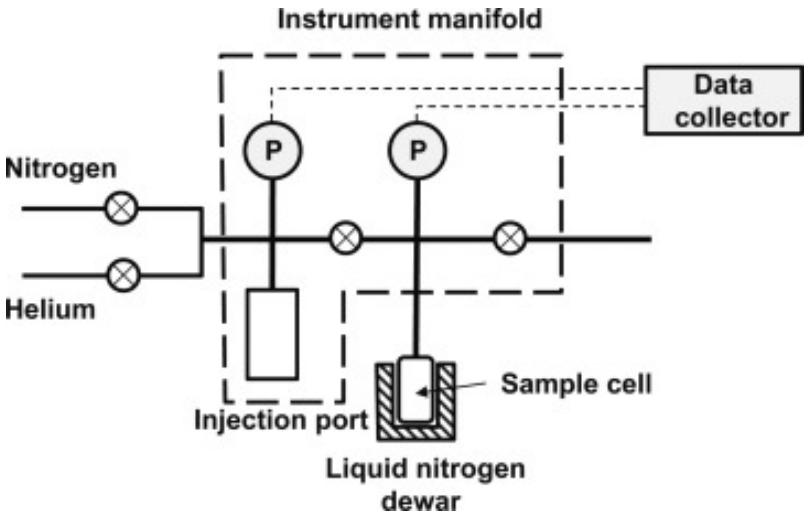

Figure 2-5. Schematic diagram of a physical adsorption analyser for determining the specific surface area and pore size distribution of carbon materials [165].

2.6 Raman spectroscopy

Raman spectroscopy is a powerful, non-destructive, ambient probing technique to characterize the structure of carbon materials [168-171]. A Raman microscopic system is capable of examining the materials from a microscopic area, with its components shown in **Figure 2-6**a [156]. As a highly monochromatic light is required for Raman spectroscopy, a laser source is used to generate the laser beam, which passes through a filter to form a single-wavelength beam. The microscope focuses the laser beam on the surface of the sample, and the Raman scattering light induced by inelastic scattering reflects from the specimen and is collected by the microscope. Holographic filters prevent the access of incident laser light. The Raman scattering light with a wavelength selected by a diffraction grating system is recorded by a charged couple device detector.

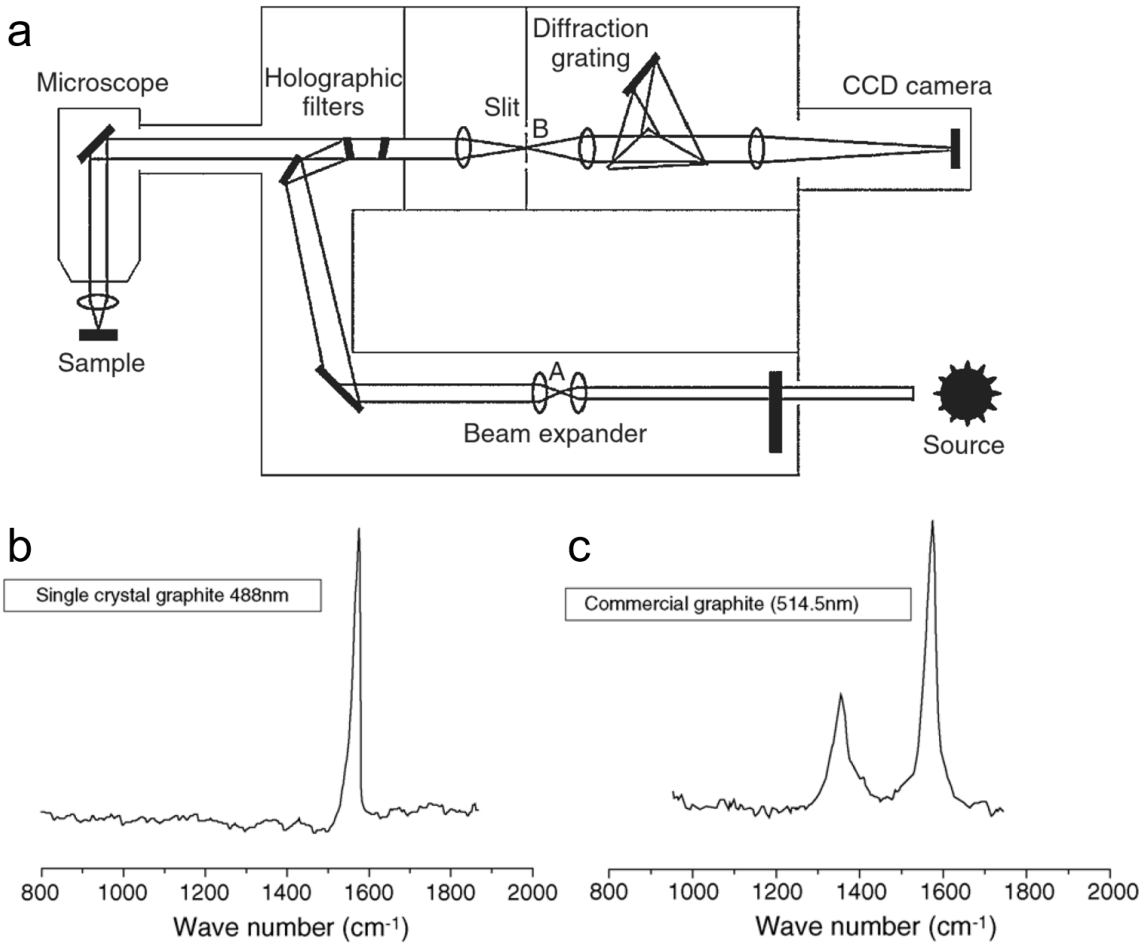

Figure 2-6. (a) Schematic diagram of a Raman microscopic system [156]. Typical Raman spectra of (b) single crystal graphite and (c) commercial graphite [158].

Raman spectroscopy is effective in distinguishing the carbon materials by examining their detailed bonding structures. **Figure 2-6**b and c demonstrate the Raman spectra for single-crystal graphite and commercial graphite materials [158]. In single-crystal graphite, one peak occurs near 1580 cm^{-1} and is designated as the G band, associated with the in-plane vibrations of crystalline graphite, indicating the graphitic nature of sp^2-hybridized carbon networks. By contrast, two characteristic peaks are observed in multi-crystalline commercial graphite. Despite the fact that one peak represents the G band, the other peak centred at 1355 cm^{-1} is referred to as D band, related to the disordered structures in the graphitic lattice. In addition,

the intensity ratio between D and G bands (I_D/I_G) could be used to indicate the defect density, structural vacancies, and/or surface functional groups in the carbon materials [164]. A larger value of I_D/I_G reveals higher defects in the carbon materials.

2.7 X-ray photoelectron spectroscopy (XPS)

X-ray photoelectron spectroscopy (XPS) is a quantitative spectroscopic technique widely used for the surface analysis of carbon materials. A typical X-ray photoelectron spectrometer is composed of an X-ray source, an electron energy analyser, and a photoelectron detector, as depicted in **Figure 2-7**a [172]. The X-ray source produces a characteristic X-ray line to excite atoms of the material surface. Electrons eject from the electron shell of the excited atom as photoelectrons. The photoelectrons are captured, and their kinetic energies are analysed to calculate the bonding energy of atomic electrons. From the binding energy spectra of X-ray photoelectrons, the chemical elements from the materials could be identified [160]. An ultrahigh vacuum environment with a vacuum pressure in the range of 10^{-8} to 10^{-10} mbar is required for XPS to eliminate the collision between photoelectrons and gas molecules in the spectrometer and prevent surface contamination from residual gas molecules [156].

XPS could provide surface chemical information of the carbon materials, such as elemental composition, chemical stoichiometry, chemical state, and electronic state of existing elements [160, 173]. As demonstrated in **Figure 2-7**b, XPS is used to detect the elements presented on the carbon nanotubes (CNTs) and oxidized CNTs (O-CNTs) [174]. Compared to CNTs, a new peak indexed to oxygen 1s occurs in O-CNTs, indicating the oxidation of CNTs after nitric acid treatment. Also, an atomic ratio of carbon to oxygen ratio is obtained as 92:8 for O-CNTs. Additionally, the carbon 1s spectrum of O-CNTs shown in **Figure 2-7**c is deconvoluted to analyse the oxygen-containing functional groups in O-CNTs. Various bands are identified for

O-CNTs, such as carbon in graphite (C-C), defects, C singly bound to oxygen (C-O), carbon bound to two oxygens (i.e., -COOH), and the characteristic shakeup line of carbon in aromatic compounds (π–π* transition) [174].

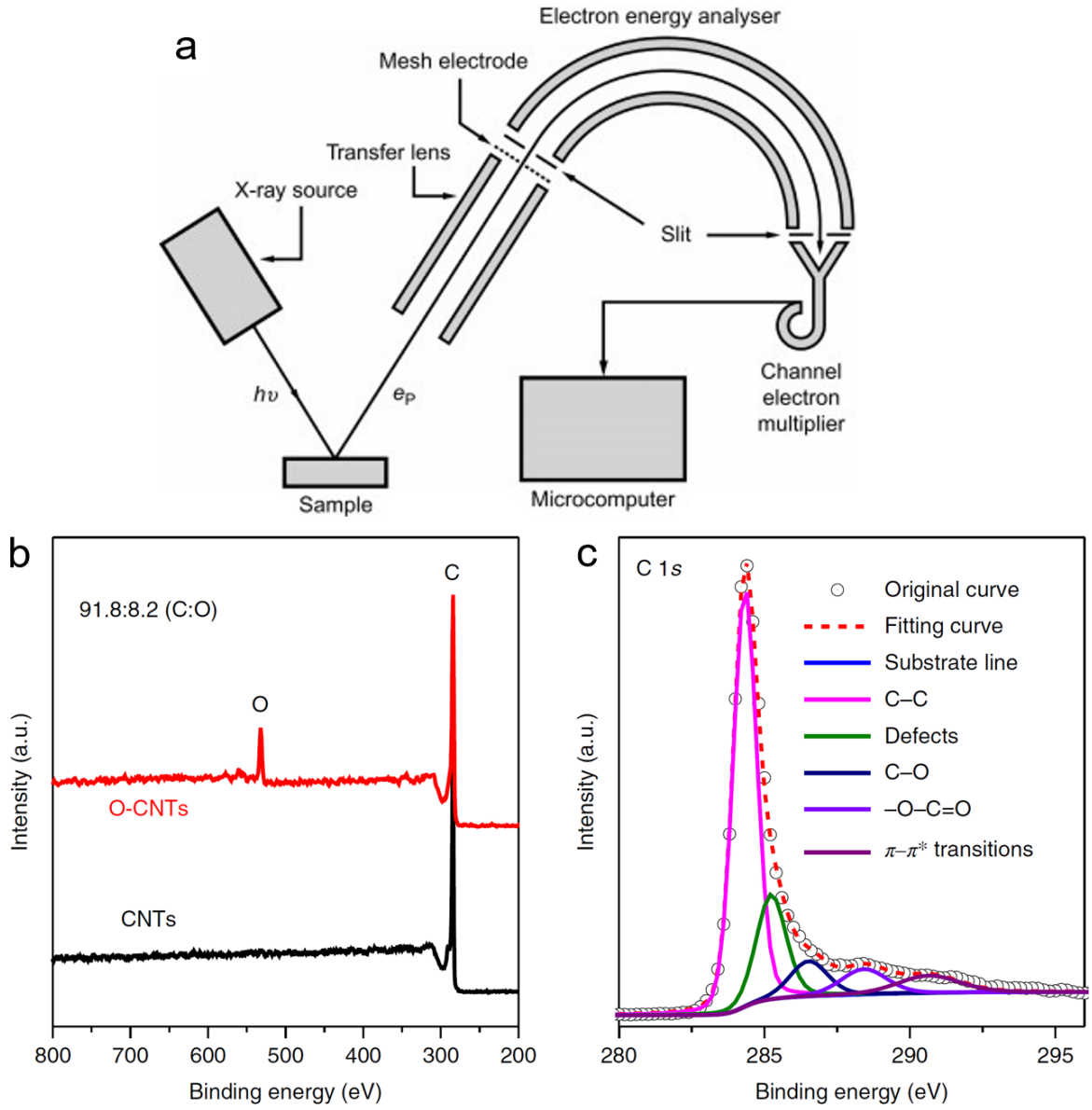

Figure 2-7. (a) Schematic diagram of an X-ray photoelectron spectrometer [172]. (b) XPS survey of carbon nanotubes (CNTs) and oxidized CNTs (O-CNTs), and (c) XPS spectra of C 1s of O-CNTs [174].

2.8 Thermogravimetric analysis (TGA)

Thermogravimetric analysis (TGA) is a technique widely employed to evaluate the quality and purity of carbon materials by monitoring the mass change of carbon materials with temperature. As illustrated in **Figure 2-8**a, the TGA instrumentation contains a furnace, a microbalance, a temperature programming unit and a recording unit [156]. A sample is placed in the furnace, and its mass changes with increasing temperature, which is monitored by a thermobalance and recorded for analysis. With upper testing temperatures generally up to 1000 ^{o}C, TGA can give information about carbon materials' decomposition and thermal stability, moisture and volatile components, and metallic impurity content in carbon materials [160]. From the TGA curve shown in **Figure 2-8**b, the decomposition of materials is identified by two characteristic temperatures, T_i and T_f, representing the onset and finishing temperatures of material decomposition, respectively [156].

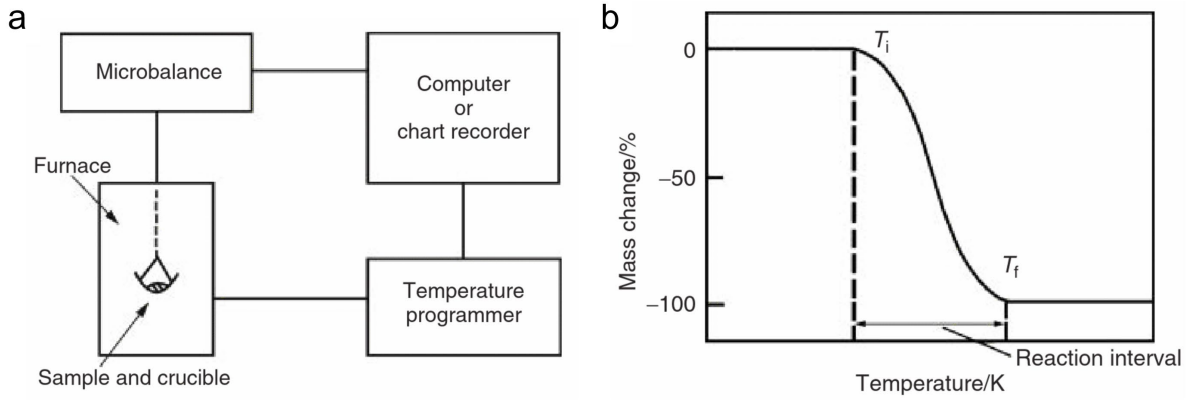

Figure 2-8. (a) Main components of a TGA instrumentation, and (b) a TGA curve representing the decomposition of materials [156].

2.9 Electrode fabrication and electrolyte preparation

Electrodes were fabricated to investigate the electrochemical performances of carbon materials. As shown in **Figure 2-9**a, electrodes consisted of three components, active material, conductive additive, and binder. As discussed in section 1.4, carbon materials could serve as conductive additives or active materials in electrodes, and thus the electrodes were prepared depending on the role of carbon materials. The three components of electrodes and the solvent were mixed manually using the mortar and pestle to form a slurry. Next, the doctor blade method was used to cast the obtained slurry on the current collector, as illustrated in **Figure 2-9**b. After drying overnight under vacuum, the current collector coated with electrode material slurries were cut into small pieces using a punching machine. These small discs were collected as electrodes and ready for use.

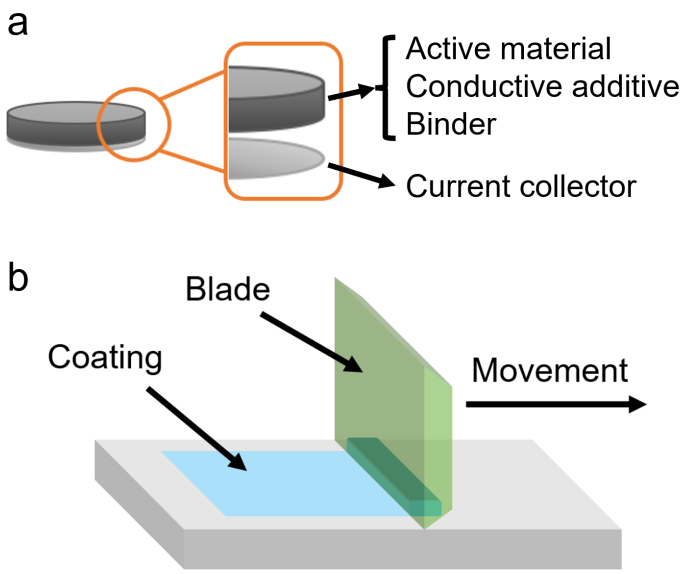

Figure 2-9. Schematic illustrations of (a) the electrode components and (b) the doctor blade method for slurry coating.

For the electrolyte preparation, 1 M zinc sulfate ($ZnSO_4$) solution was used as the electrolyte for the zinc-carbon batteries in the research chapter 3. It was prepared by dissolving zinc sulfate heptahydrate ($ZnSO_4 \cdot 7H_2O$) in deionized water, followed by sufficient stir to obtain the electrolyte. In the research chapter 4, 1 M lithium hexafluorophosphate ($LiPF_6$) in ethyl methyl carbonate (EMC) was used as the electrolyte for the dual-carbon batteries, which was directly purchased from Sigma-Aldrich.

2.10 Coin cell assembly

CR2032-type coin cells were assembled to evaluate the electrode electrochemical performances. **Figure 2-10** shows a typical coin cell configuration, composed of a negative case, two spacers, an anode, a separator, a cathode, a spring, and a positive case. These components were stacked in sequence, and the electrolyte drop was added on the separator to wet the separator. Eventually, a coin cell crimper was used to seal the cells. All assembled cells were placed to rest for 20 h before testing.

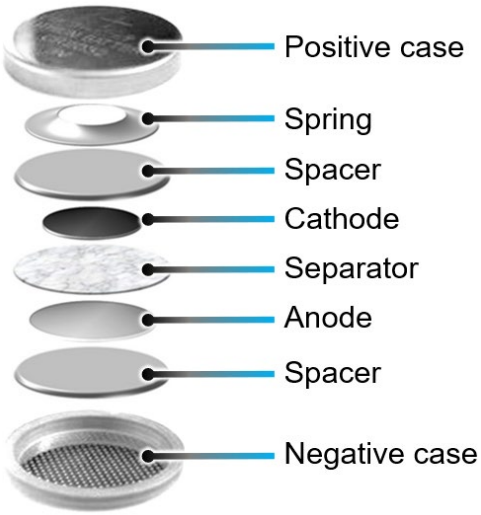

Figure 2-10. Schematic diagram of a typical coin cell configuration.

2.11 Electrochemical characterization

Electrochemical measurements were performed to characterize the electrochemical performances of battery cells. Here, the commonly used electrochemical characterization techniques were discussed, including linear sweep voltammetry and cyclic voltammetry, electrochemical impedance spectroscopy, and galvanostatic charge–discharge measurements.

2.11.1 Linear sweep voltammetry (LSV) and cyclic voltammetry (CV)

Linear sweep voltammetry (LSV) and cyclic voltammetry (CV) were proposed at the beginning of the 1950s and have become the most widely used voltametric techniques to study the redox reactions of materials and provide information on the steps involved in the electrochemical processes [175]. A typical three-electrode electrochemical cell for conducting LSV and CV is illustrated in **Figure 2-11**a [176]. The cell consists of three electrodes inserting into the electrolyte solution, including a working electrode, a reference electrode, and a counter electrode. During the experiment, the potential difference between the working and reference electrodes varies at a constant rate and in the meantime, the current between the working and

counter electrodes is measured, resulting in the data plotted as current vs. potential [177]. LSV and CV are similar techniques. The potential is scanned from a lower limit to an upper limit in LSV, while in CV, the direction of the potential scan is reversed at the end of first scan and the potential range is scanned in the reverse direction. A typical cyclic voltammogram for a battery-type material is shown in **Figure 2-11**b, which helps to extract information such as redox peaks associated with oxidation and reduction, and the reversibility of the charge transfer reactions [178]. Since the relevant responses of electrode stimulation could happen within few milliseconds and the short-lived transient intermediates could be detected, LSV and CV are effective for mechanism studying including fast reactions [175].

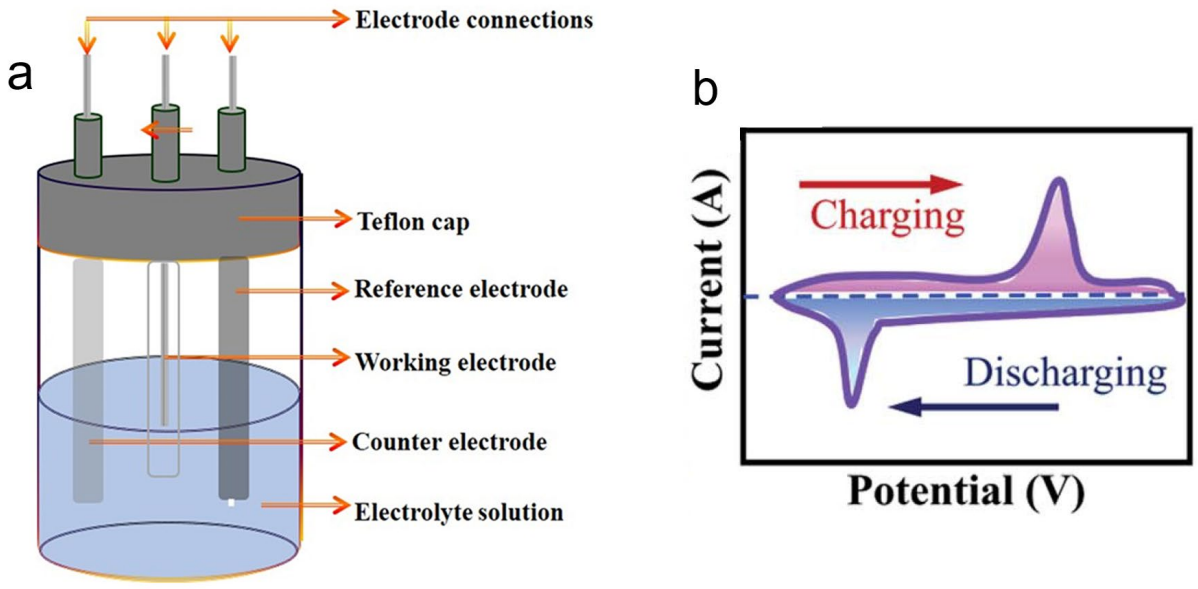

Figure 2-11. (a) A typical three-electrode electrochemical cell for LSV and CV measurements [176]. (b) A typical cyclic voltammogram for a battery-type material [178].

2.11.2 Electrochemical impedance spectroscopy (EIS)

Electrochemical impedance spectroscopy (EIS) is a powerful tool for investigating electrochemical systems, providing a wealth of information regarding electrochemical reactions and kinetics in a relatively short space of time [179]. In EIS, a small-amplitude sinusoidal signal of potential or current is applied to the electrochemical system over a wide frequency range, and the current or potential response of the system toward the applied perturbation is measured, from which the electrochemical impedance of the system can be deduced [180]. The impedance can be divided into a real part and an imaginary part,

$$Z = Z' + i\,Z''$$

which is usually presented in a complex plane plot, also referred to as a Nyquist plot, with the real part (Z') plotted on the x-axis and the imaginary part (Z'') plotted on the y-axis [181]. An example of a Nyquist plot is illustrated in **Figure 2-12** [182]. The semicircle in high frequency region is related to the electrochemical process controlled by charge transfer phenomena, while the straight line in low frequency region is associated with the electrochemical process controlled by mass transfer phenomena. The EIS measurements of an electrochemical system can be simulated to an equivalent electrical circuit that comprises a combination of resistances, capacitances, inductors and mathematical components [183]. From an example of Randles equivalent circuit shown in **Figure 2-12**, R_u is the equivalent series resistance determined by the intercept of semicircle on the real axis, and R_{ct} is the charge transfer resistance related with the kinetics of the electrochemical process. C_{dl} is the capacitance of the electrical double layer, and Z_W is the Warburg impedance, which represents the difficulty of mass transport of the redox species to the electrode surface [182].

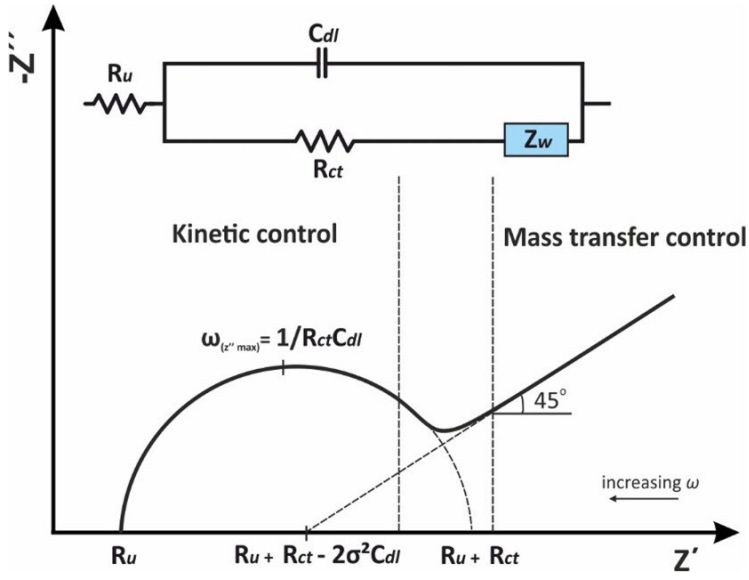

Figure 2-12. Nyquist plots for an electrochemical process and the Randles equivalent electrical circuit [182].

2.11.3 Galvanostatic charge–discharge (GCD) measurements

Galvanostatic charge-discharge (GCD) is an effective technique for evaluating electrochemical systems, offering information including electrochemical behavior, specific capacity, and cell cyclic stability [184, 185]. GCD involves the application of constant positive and negative currents to charge and discharge the cells within a set potential range, and the potential variation with time is recorded. **Figure 2-13**a shows a typical GCD profile for a battery system with charging/discharging plateaus [178]. The specific capacity $C_{specific}$ (mAh g^{-1}) of the cell during charge and discharge could be calculated by multiplying the applied current density I (mA g^{-1}) and the duration t (h) of a single charge or discharge step:

$$C_{specific} = I \times t$$

Repeating the GCD process for multiple cycles could determine the cyclic stability of the cells. Furthermore, a set of different current densities could be used to perform the GCD measurements, which helps to analyse the rate performance of the cells. As illustrated in **Figure**

2-13b, different current densities were used to determine the rate performance of a lithium-ion battery cell, with the corresponding GCD curves shown in **Figure 2-13**c [186].

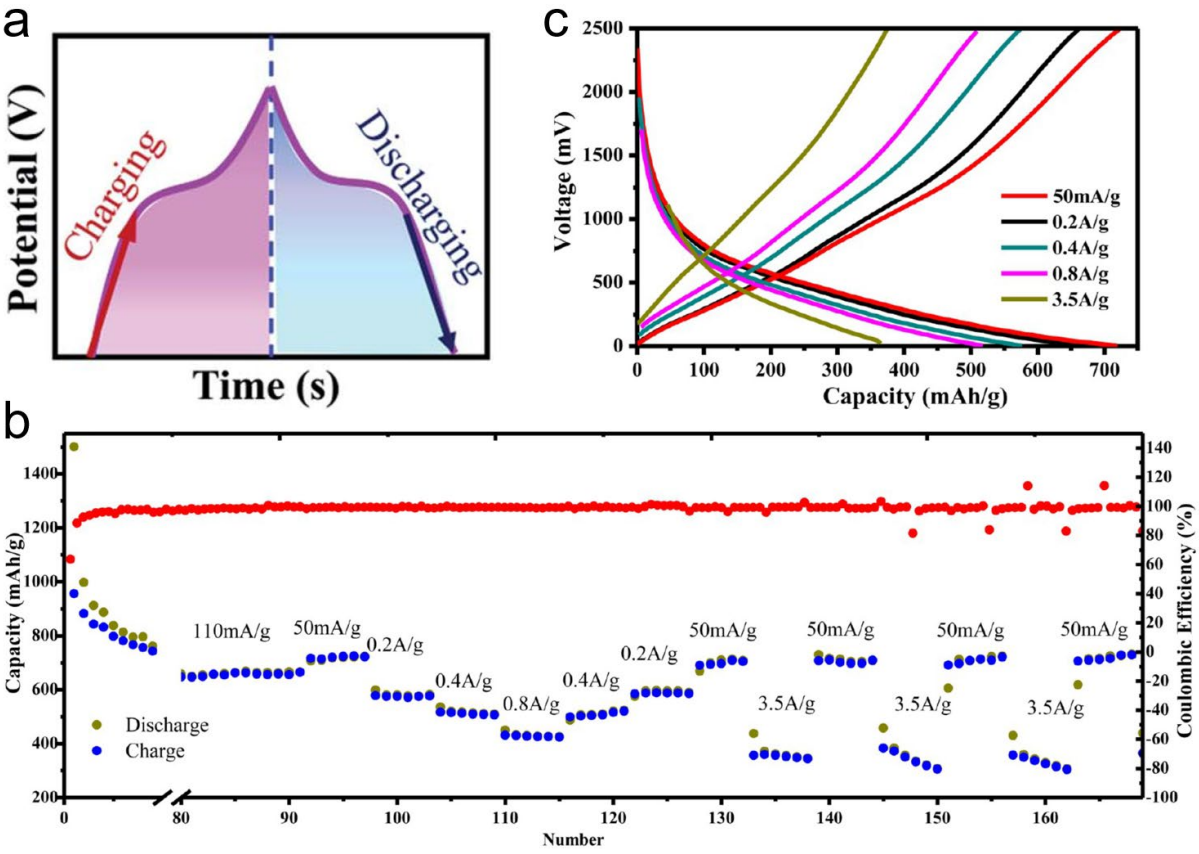

Figure 2-13. (a) A typical GCD profile for a battery-type material [178]. An example of (b) the rate performance of a lithium-ion battery cell under different current densities, and (c) the corresponding GCD curves [186].

Chapter 3. Graphitic carbon from catalytic methane decomposition as an efficient conductive additive for zinc-carbon batteries

3.1 Introduction

Hydrogen (H_2) gas is an environmentally friendly chemical fuel widely used in ammonia production, oil refining, and metallurgy [187]. Currently, H_2 is mainly produced from steam reforming of methane (CH_4) or coal gasification with significant carbon dioxide (CO_2) emissions [188, 189]. Besides water electrolysis using electricity, a promising H_2 production approach is the catalytic decomposition of CH_4 (CDM), directly decomposing CH_4 into H_2 and solid carbon materials ($CH_4 \rightarrow 2H_2 + C$) [190-195]. Although CDM can occur on various catalysts, the deposition of solid carbon materials on catalytic metal surfaces quickly deactivates catalysts, making the process uneconomical [196-201]. Low-cost catalysts, such as natural iron (Fe) ores, have been explored to address this challenge, eliminating expensive catalyst regeneration [202]. Considering that the mass ratio between H_2 and solid carbon material co-product in CDM is 1 to 3, even a small industrial-scale CDM-based H_2 production facility would produce thousands of carbon materials. Thus, using these carbon materials in suitable applications is essential in reducing waste generation and brings economic benefits.

Zinc-carbon (Zn-C) batteries are among the most widely used primary batteries to power radios, remote controls, alarm clocks, and small electronic devices [203]. Zn-C batteries usually use a Zn metal anode, a manganese dioxide (MnO_2) cathode, and an aqueous salt electrolyte with a simplified overall cell reaction: $Zn + 2MnO_2 \rightarrow ZnO + Mn_2O_3$ [203]. Carbon conductive additives are a crucial component of Zn-C batteries, even though they do not participate in electrochemical reactions. Carbon conductive additives increase the electrical

conductivity of non-conductive electrolytic manganese dioxide (EMD). They also hold aqueous paste electrolytes and EMD, improving their compressibility and elasticity during electrode processing and battery assembly [203]. Various carbon materials have been used as conductive additives in batteries, including amorphous carbon black, onion-like carbon spheres, carbon nanotubes, carbon fibres, and graphene materials [204-213]. High-quality carbon conductive additives play critical roles in battery performance and contribute to the high cost of battery manufacturing. Thus, it is speculated that carbon materials produced in the CDM-based H_2 production process may serve as a new high-performance and low-cost carbon conductive additive for batteries.

Herein, graphitic carbon materials were synthesized via CDM using Fe ores as catalysts. The resulting carbon materials were further purified by a standard high-temperature thermal treatment and an alternative electrochemical method. Various characterization tools first examined the resulting carbon materials to determine their physiochemical proprieties. Next, EMD cathodes were fabricated using purified and unpurified graphitic carbon materials and compared them with a commonly used carbon conductive additive (Super P). Last, Zn-C batteries were assembled using EMD cathodes, and their performance was compared in standard battery tests [76, 203]. The results show that the carbon co-product from the CDM-based H_2 production process can serve as an efficient conductive additive for Zn-C batteries.

3.2 Experimental section

3.2.1 Material synthesis

Carbon materials were synthesized by CDM using a Fe ore as the catalyst in a fluidized bed reactor system. A simplified illustration of the reactor system is illustrated in **Figure 3-1**a. It should be noted that CDM is highly sensitive to various factors, from catalysts, reactors, gas

precursors, to operational parameters [200, 202]. However, it is not difficult to obtain graphitic carbon materials under typical operating conditions. In general, various Fe ores can be used as catalysts in CDM. This study used a Limonite ore from Western Australia, containing about 61.5 wt.% Fe, 3.34 wt.% SiO_2, and 1.16 wt.% Al_2O_3 based on X-ray fluorescence spectroscopy (XRF) analysis results shown in **Table 3-1**. The Fe ore was milled and screened to around 100–200 μm. The customized fluidized bed reactor has an internal diameter of 2 inches. The reactor material (Inconel 625) prevented CDM on the reactor wall. The catalysts were not reduced before CMD. 150 g of Fe ore particles were injected into the reactor every 20 min. CMD was carried out under 6 bar natural gas at 890 ^oC with the gas feed rate of 5.5 m^3/h (standard conditions) at an hourly gas space velocity of 12.22 $L/g_{cat.}$. The reactor was operated at a steady state for about 6 h. CH_4 catalytically decomposed on Fe surfaces into H_2 and carbon materials. With the deposition of carbon materials, Fe ore particles disintegrate into lower density nano-fragments and are carried out of the reactor to a cyclone separator by the gas stream. Fe ore particles coated with carbon materials are separated from the gas stream and fall to the bottom of the cyclone separator. The resulting graphitic carbon materials encapsulating Fe particles are named "GCs". The higher reaction temperature of 890 ^oC and pressure of 6 bar was used because it was noticed that graphitic layers were less defective under these conditions, which helped improve their electrical conductivity.

During CDM ($CH_4 \rightarrow 2H_2 + C$), excess amounts of CH_4 were supplied to run the fluidized bed. Unused CH_4 can be separated from H_2 and reused. The deposition of CH_4 on Fe surfaces is affected by various factors, such as CH_4 flow rate, duration of reaction time, heating temperature, and pressure. From the TGA result of GC (**Figure 3-4**d) and XRF analysis of ash residues obtained after TGA (**Table 3-1**), the purity of GC was determined to be 78.25 wt.%. Thus, the molar ratio of produced carbon to Fe in GC is roughly 16.73 (n_C : n_{Fe} = [78.25%/12.01]/[(1-78.25%)/55.845]=16.73).

In the steady state synthesis condition, catalysts (450 g/hour) contain 88 wt.% of Fe_2O_3, 2.48 mol (450×88%/159.69) of Fe_2O_3, or 4.96 mol of Fe. Thus, solid carbon materials produced was 82.97 mol (16.73×4.96). CH_4 (245.37 mol, assuming an ideal gas) was supplied at 5.5 m^3 (standard temperature and pressure) on 450 g of catalysts in 1 h. Thus, the conversion of CH_4 to C was around 33.8% (82.97 mol/245.37 mol).

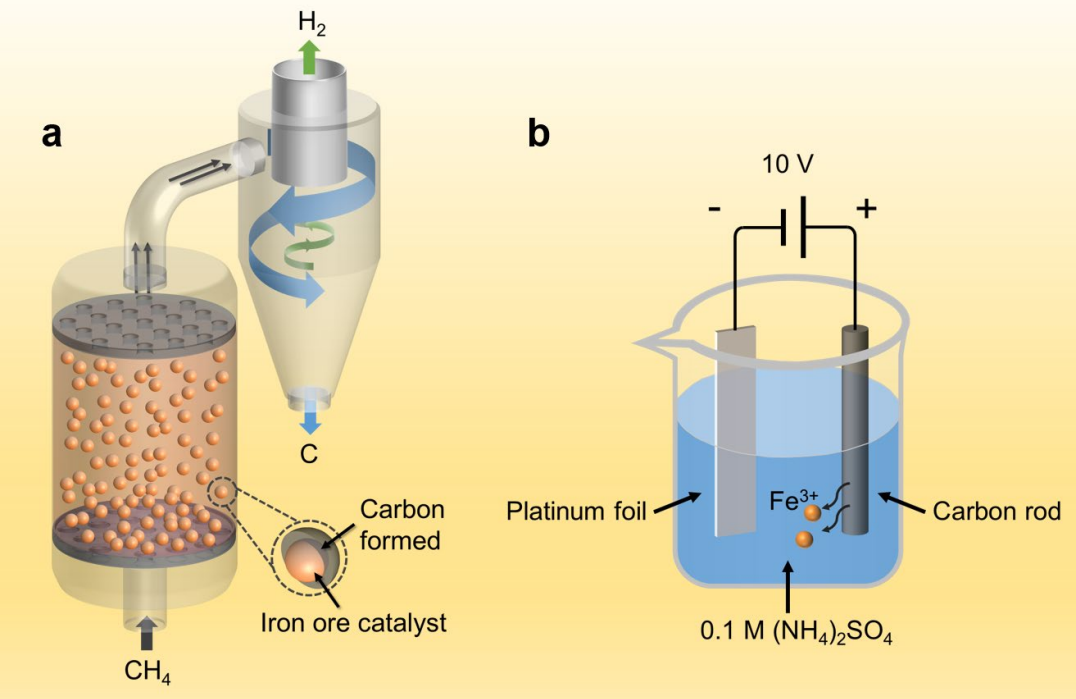

Figure 3-1. Schematic illustrations of (a) the synthesis of graphitic carbon materials encapsulating Fe particles by catalytic decomposition of CH_4 on Fe ore catalysts and (b) the electrochemical cell used to purify the graphitic carbon materials.

Table 3-1. XRF analysis of Fe ore catalyst used for CDM process (left), and XRF analysis of GC ash composition after combustion at 900 ºC for TGA test (right).

Oxides	Composition (wt.%)	Oxides	Composition (wt.%)

Fe_2O_3	88.00	Fe_2O_3	95.32
Al_2O_3	1.16	Al_2O_3	2.9
SiO_2	3.34	SiO_2	1.03
P_2O_5	0.28	P_2O_5	0.32
Na_2O	0.24	Na_2O	0.12
TiO_2	0.08	TiO_2	0.02
MgO	0.20	Mn_3O_4	0.01
CaO	0.02	MgO	<0.01
Loss on ignition at 1,050 °C	5.95	CaO	<0.01

GC was first purified by the standard thermal purification method used for graphite purification [214-216]. GC was loaded in a high-temperature vacuum furnace, and the temperature was slowly increased to 2800 °C at 100 °C h^{-1} and kept at 2800 °C for 3 h, removing encapsulated Fe particles. The resulting material is denoted as "TG". Alternatively, GC was also purified using an electrochemical cell similar to those used to synthesize graphene or graphene oxide flakes from graphitic carbon materials [217-219]. GC was compressed into carbon rods. As illustrated in **Figure 3-1**b, the carbon rod containing GC serves as a positive working electrode. A platinum foil serves as a negative counter electrode in a 0.1 M ammonium sulfate ($(NH_4)_2SO_4$) electrolyte. A DC power of 10 V was applied to the two electrodes. Charged ions in the electrolyte were intercalated among graphene layers of carbon materials in the carbon rod, and encapsulated Fe particles were slowly leached over 20 h. The resulting carbon materials in the carbon rod was collected and denoted as "EG". Apart from the above three types of graphitic carbon materials, a commercial carbon conductive additive (Super P,

Thermo Fisher) was used as a reference. EMD was purchased from Changsha Easchem Co. Limited and used as active cathode materials for Zn-C batteries.

3.2.2 Material characterization

The morphology of the carbon materials was examined by scanning electron microscopy (SEM, Zeiss, Gemini Ultra Plus). Their microstructures were further characterized by transmission electron microscopy (TEM, JEOL, JEM-2100), operated at an accelerating voltage of 200 kV. The average particle size of carbon materials dispersed in water was analysed using a particle size analyser (Malvern Mastersizer 3000). Their surface area and pore structures were characterized by N_2 physisorption using a pore size analyser (Quantachrome Autosorb iQ). The density functional theory method was used to calculate their pore size distribution from their N_2 physisorption isotherms. Their chemical properties were characterized by Raman spectroscopy (Renishaw Raman inVia Reflex) under a 532 nm excitation laser. Their chemical composition was investigated by thermogravimetric analysis (TGA) on a thermogravimetric analyser (TA Instruments Q500) under an airflow with temperatures increasing from 25 to 900 ^{o}C at a ramping rate at 15 ^{o}C min^{-1}. The elemental composition of the ashes obtained after TGA was characterized by XRF using a wavelength dispersive XRF spectrometer (PANalytical AXIOS, PW2400) fitted with a 4-kW X-ray source.

3.2.3 Electrode fabrication and characterization

EMD was first homogenized in a planetary ball milling (Changsha Tianchuang Power Technology XQM-0.4) at 400 rpm for 5 h. Next, EMD, carbon conductive additives, and polyvinylidene fluoride (PVDF) binder were mixed with a weight ratio of 7: 2: 1 in N-methyl-2-pyrrolidone (NMP). The four carbon materials (Super P, GC, TG, and EG) were used as

conductive additives separately. The obtained slurry was cast on titanium (Ti) foils with a thickness of 10 μm using the doctor blade method, followed by drying at 80 ^{o}C for 12 h in a vacuum furnace. The mass loading of active electrode materials on Ti foils was ~ 2.5 mg cm^{-2}. Finally, Ti foils coated with electrode material slurries were cut into small pieces of 1.1 cm^2 in size using a punching machine.

The in-plane electrical conductivity of EMD cathodes fabricated using different carbon materials was examined by a four-point probe sheet resistance meter (Guardian SRM-232). The conductivity (σ, S m^{-1}) was calculated by $\sigma = 1/R_S t$, where R_S (Ω/sq) is the sheet resistance, t is the thickness of electrode materials. The electrolyte absorption capability of carbon conductive additives was measured by immersing carbon electrodes (without EMD) fabricated using carbon materials (90 wt.%) and PVDF (10 wt.%) into the same volume of 1 M zinc sulfate ($ZnSO_4$) solution and recording the weight gain as a function of time.

3.2.4 Zn-C battery assembly and characterization

Coin cells (2032-type) were assembled using prepared EMD cathodes, Zn metal foil (1.1 cm^2) as anodes, and 1 M $ZnSO_4$ solution as the electrolyte to evaluate their electrochemical performance. Galvanostatic charge/discharge (GCD) in a voltage range of 1.5–0.7 V and electrochemical impedance spectroscopy (EIS) measurements in a frequency range between 10^6–0.008 Hz were collected using an electrochemical workstation (CHI 760D). The specific capacity of batteries was calculated based on the mass of EMD in cathodes. Galvanostatic intermittent titration technique (GITT) tests were carried out on assembled batteries using a battery testing system (LANHE) with a series of galvanostatic discharge pulses of 120 s at 50 mA g^{-1} followed by a 4 h rest. Battery long-term stability tests were conducted using the battery

testing system over a rest time of one month by continuously recording the open-circuit voltage (OCV). All electrochemical tests were performed at room temperature.

3.3 Results and discussion

3.3.1 Properties of carbon materials

SEM images in **Figure 3-2**a - d show the morphology of the four types of carbon materials (Super P, GC, TG, and EG). Super P displays a powdery and fine-grained morphology with particle sizes on the nanometer scale, different from the other three graphitic carbon materials synthesized by CDM. Those carbon materials mainly consist of a micrometer-sized cloddy structure with numerous irregularities on their surfaces. GC shows a rougher surface topography, while TG and EG have relatively smoother surfaces formed by irregularly shaped particles made up of carbon flakes. The internal morphology and structure of synthesized carbon materials were characterized by TEM. As shown in **Figure 3-2**e, a carbon nano-onion-like structure was observed for GC, which was formed by Fe encapsulated in graphitic carbon. **Figure 3-2**f and g present TG and EG displaying hollow nanoparticles with graphitic carbon shells, suggesting the removal of Fe by thermal and electrochemical purification. The graphitic structure of GC, TG and EG was further confirmed by **Figure 3-2**h - j, respectively. Their average particle size was analysed using a particle size analyser. As shown in **Figure 3-3**, when dispersed in an aqueous solution, Super P, GC, and TG all have a similar median diameter (D_{50}) ranging from 9.1–12.4 μm. In comparison, EG has a smaller size of around 1.9 μm.

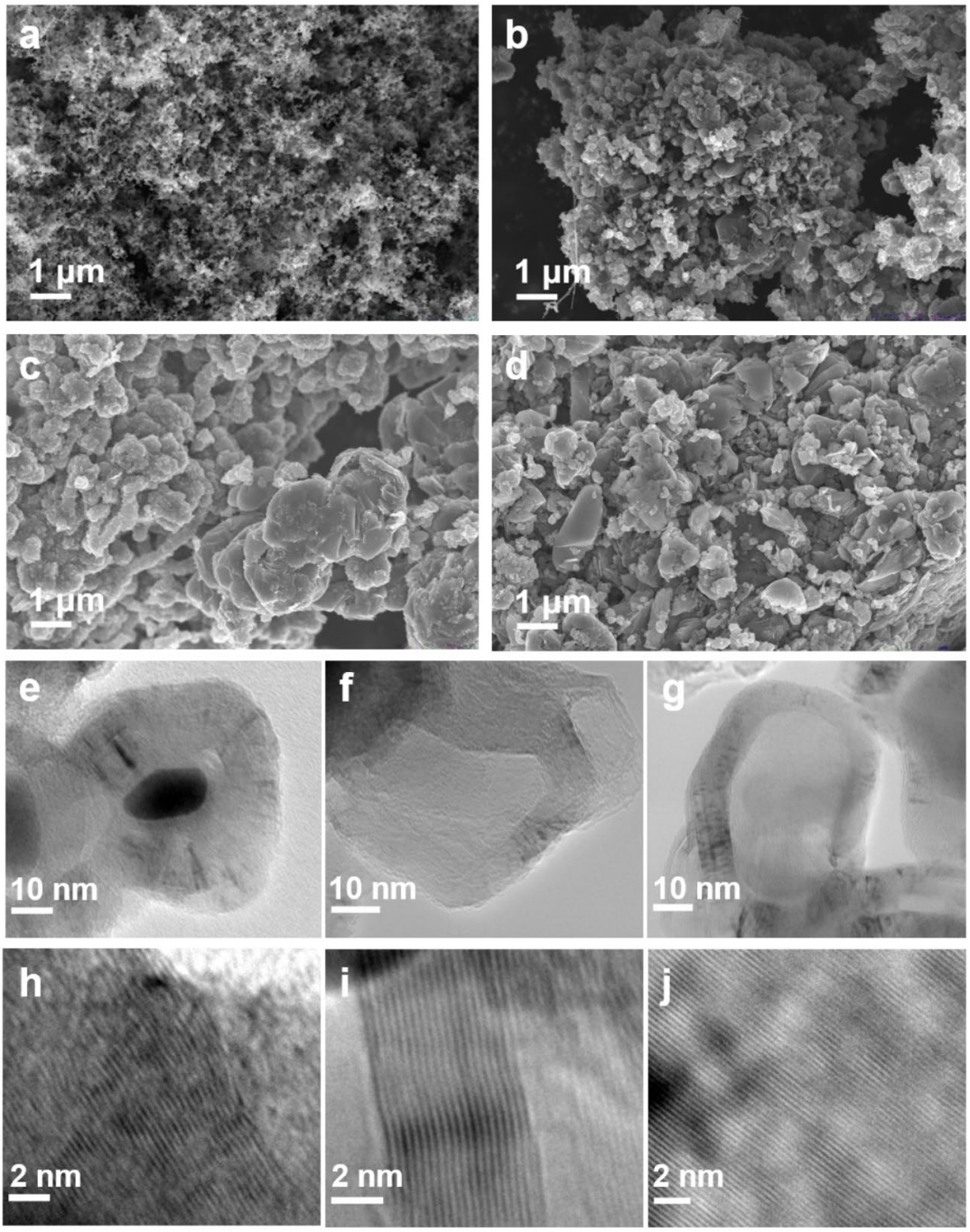

Figure 3-2. SEM and TEM images of carbon materials used as conductive additives in this study. SEM images of (a) Super P, (b) GC, (c) TG, and (d) EG. TEM images of (e) GC, (f) TG, (g) EG, and their graphitic structures (h) GC, (i) TG, and (j) EG.

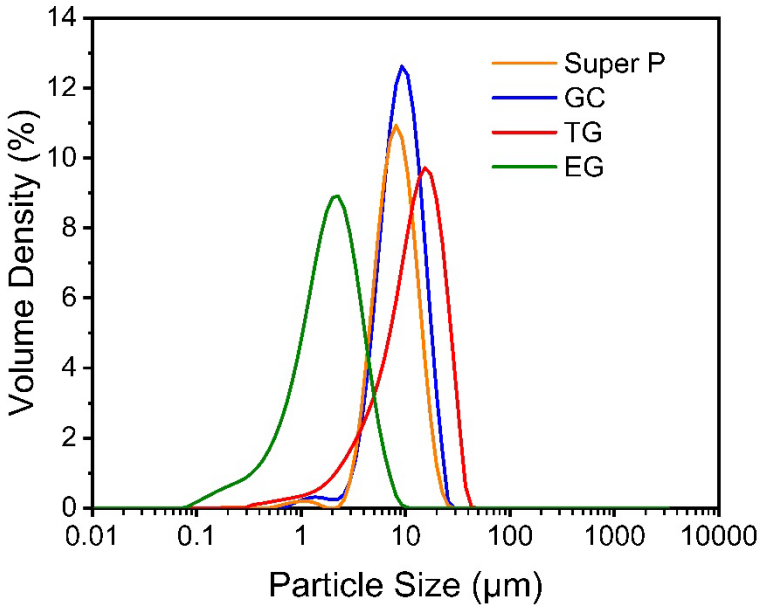

Figure 3-3. Particle size distribution profiles of carbon materials used as conductive additives in this study: Super P, GC, TG, and EG.

The specific surface area and pore structure of carbon materials were characterized by N_2 physisorption. **Figure 3-4**a shows their N_2 physisorption isotherms. Their BET-specific surface area varies from 19–37 $m^2\ g^{-1}$, following TG < GC < EG. Super P has a much larger surface area of 78 $m^2\ g^{-1}$. Their pore size distribution determined by the DFT method is illustrated in **Figure 3-4**b. Super P has the largest pore volume of 1.83 $cm^3\ g^{-1}$ with an average pore size of 36 nm, indicating its mesoporous nature. GC and EG exhibit broad pore size distributions ranging from micropores to macropores. The pore volume and average pore size of GC and EG are similar at 0.13 $cm^3\ g^{-1}$, 3.8 nm, and 0.15 $cm^3\ g^{-1}$, 2.9 nm, respectively, which indicates that the electrochemical purification process does not significantly change the porous structure of GC. In contrast, TG shows a pore size distribution centred around 30.1 nm and a larger pore volume at 0.30 $cm^3\ g^{-1}$. The disappearance of small pores in TG and the increased pore volume may be related to the complete removal of metal residues encapsulated in carbon and the restructuring and closing of small pores at high temperatures.

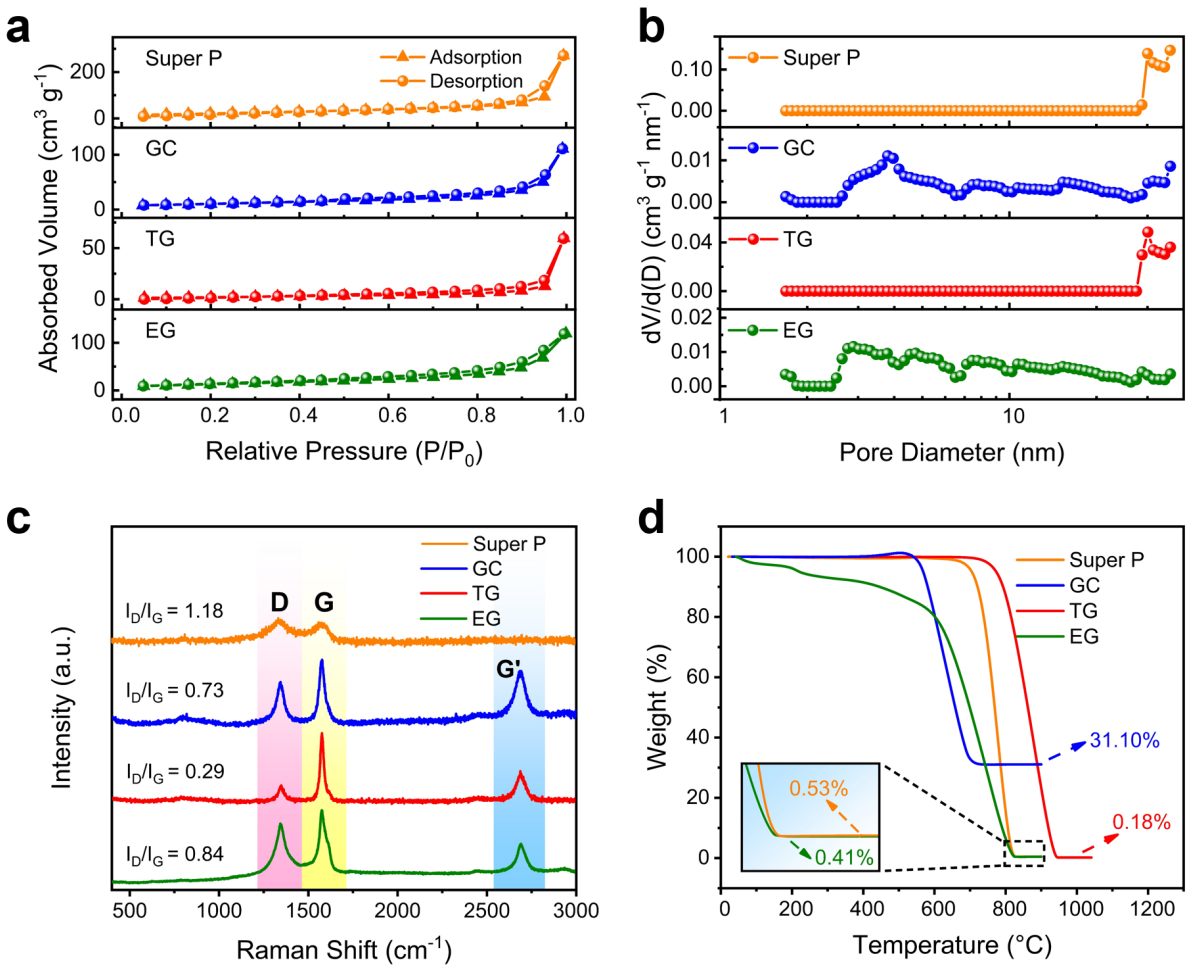

Figure 3-4. (a) N_2 physisorption isotherms, (b) Pore size distribution, (c) Raman spectra, and (d) TGA profiles of different carbon materials: Super P, GC, TG, and EG.

The chemical structure of carbon materials was first analysed by Raman spectroscopy. **Figure 3-4**c shows their Raman spectra with three typical carbon material features: G band corresponding to zone centre vibration of carbon atoms in graphene planes, D band associated with the disorder in a graphitic lattice, and G' band related to the number of graphene layers and their stacking order [220, 221]. Super P only displays D and G bands, suggesting a lack of long-range graphitic structures. The intensity ratio of D and G bands (I_D/I_G) can be correlated to defects, structural vacancies, and surface functional groups in carbon materials. The I_D/I_G of

Super P is 1.18, which is higher than GC at 0.73, EG at 0.84, and TG at 0.29. These results indicate that TG has the lowest level of defects due to its high-temperature treatment condition. In contrast, EG has a relatively higher concentration of defects due to the exfoliation of graphene layers during purification. Super P has the most defective structure.

Their chemical structures and metal residues were further examined by TGA. **Figure 3-4**d and its inset show their weight loss profiles in the air when the temperature increases from 25 to 900 ºC (25 to 1040 ºC for TG due to its higher thermal stability). Derivative thermogravimetry (DT) profiles are shown in **Figure 3-5**. The primary weight loss of TG takes place at the highest temperature at 882 ºC, suggesting the highest graphitic level. The central weight loss temperature of Super P at 776 ºC is also higher than those of EG and GC. The main weight loss temperature of GC is the lowest at 632 ºC, attributing to the oxidative decomposition of carbon catalysed by Fe residues. Further, EG has some weight loss starting from 48 ºC, originating from volatile components formed during its electrochemical purification. TG has the lowest ash content of 0.18 wt.%, indicating the highest carbon purity of 99.82 wt.%. EG and Super P also have a high purity of 99.59 wt.% and 99.47 wt.%, respectively. GC has the top ash content of 31.10 wt.%. XRF was used to analyse the chemical composition of the ash residues obtained after TGA. As listed in **Table 3-1**, since Fe_2O_3 counts for 95.32 wt.% of the ash, it is assumed that all the ash residues of GC are Fe_2O_3 to calculate the purity of GC. Fe_2O_3 was formed by the oxidation of Fe residues encapsulated in carbon materials. The molar mass of Fe and Fe_2O_3 is 55.85 g mol^{-1} and 159.69 g mol^{-1}, respectively. Therefore, the purity of GC is estimated to be:

$$100\ wt.\% - 31.10\ wt.\%\ (Fe_2O_3) \times \frac{2 \times 55.85}{159.69} = 78.25\ wt.\%$$

The physiochemical properties of carbon materials are summarised in **Table 3-2**.

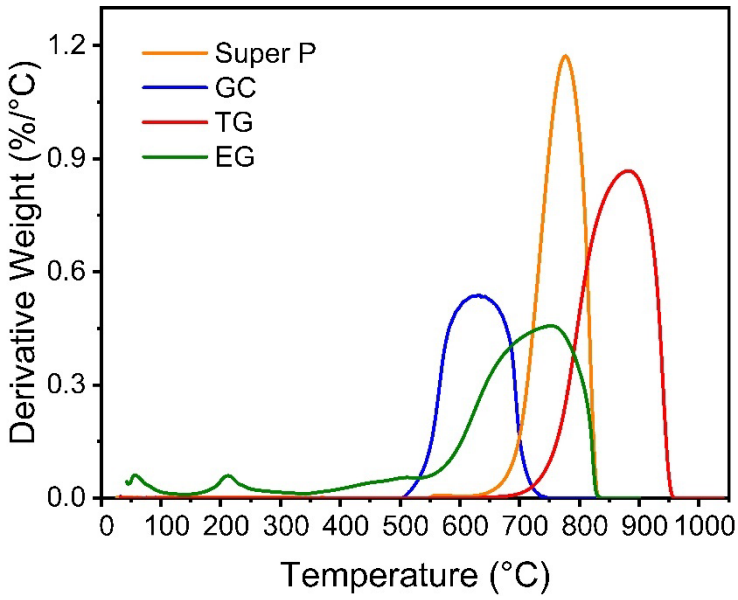

Figure 3-5. Derivative thermogravimetry (DT) profiles of different carbon materials: Super P, GC, TG, and EG.

Table 3-2. A summary of physiochemical properties of carbon materials, the electrical conductivity of EMD/carbon electrodes, and electrolyte absorption capacity of carbon electrodes.

Carbon materials	D_{50} (μm)	SSA ($m^2 g^{-1}$)	V_{pore} (cc g^{-1})	d_{pore} (nm)	Raman I_D/I_G	T_{TGA} (°C)	P_{carbon} (wt.%)	$C_{electrode}$ (S m^{-1})	AC (mass ratio)
Super P	9.1	78	1.83	36.0	1.18	776	99.47	72	10.94
GC	9.3	30	0.13	3.8	0.73	632	78.25	143	1.84
TG	12.4	19	0.30	30.1	0.29	882	99.82	98	2.14
EG	1.9	37	0.15	2.9	0.84	749	99.59	90	4.20

D_{50} = Median diameter (μm), SSA = Specific surface area ($m^2 g^{-1}$), V_{pore} = Total pore volume (cc g^{-1}), d_{pore} = Average pore size (nm), T_{TGA} = TGA main peak temperature (°C), P_{carbon} = Carbon

purity (wt.%), $C_{electrode}$ = Electrode conductivity (S m^{-1}), AC = Electrolyte absorption capacity (mass ratio).

3.3.2 Properties of fabricated electrodes

The different carbon materials were used as conductive additives at the same mass ratio to fabricate EMD electrodes. The electrical conductivity of fabricated electrodes may be influenced by multiple factors, such as graphitic structures of carbon additives and their particle size, surface area, and porosity [76, 222, 223]. The in-plane electrical conductivity of EMD electrodes fabricated using Super P is the lowest at 72 S m^{-1}, which can be ascribed to its porous and defective structures [224, 225]. In comparison, the EMD electrodes fabricated using the two purified carbon materials, *i.e.*, TG and EG, have a similar electrical conductivity of 98 and 90 S m^{-1}, respectively. The higher electrical conductivity is correlated with their more graphitic characteristics, as shown in Raman results. The pore size difference between TG and EG seems not to affect the electrical conductivity significantly. The larger surface area of Super P also does not bring beneficial effects on the electrical conductivity of electrodes. The electrode fabricated using GC has the highest electrical conductivity of 143 S m^{-1}, which may be related to its substantial fraction of Fe residues, considering that it has a higher I_D/I_G ratio and similar specific surface area and average pore size as EG.

Another essential function of carbon conductive additives is absorbing and holding electrolytes to maintain stable solid-liquid interfaces in electrodes [76, 226]. However, extremely high electrolyte capacity would consume more electrolytes, increasing battery manufacture costs. The electrolyte absorption capacity is influenced by carbon additives' pore volume, pore size, and surface area. **Figure 3-6** shows the electrolyte uptake by the different types of carbon materials (in the unit of mg electrolyte per mg carbon) in 5 min when carbon

electrodes are immersed in 1 M $ZnSO_4$ solution. The substantially larger specific surface area and pore volume of Super P led to faster electrolyte update and the highest absorption capacity of 10.94, about 6 times that of GC at 1.84 after 5 min. The electrolyte absorption capacity of TG at 2.14 and EG at 4.20 are both higher than that of GC.

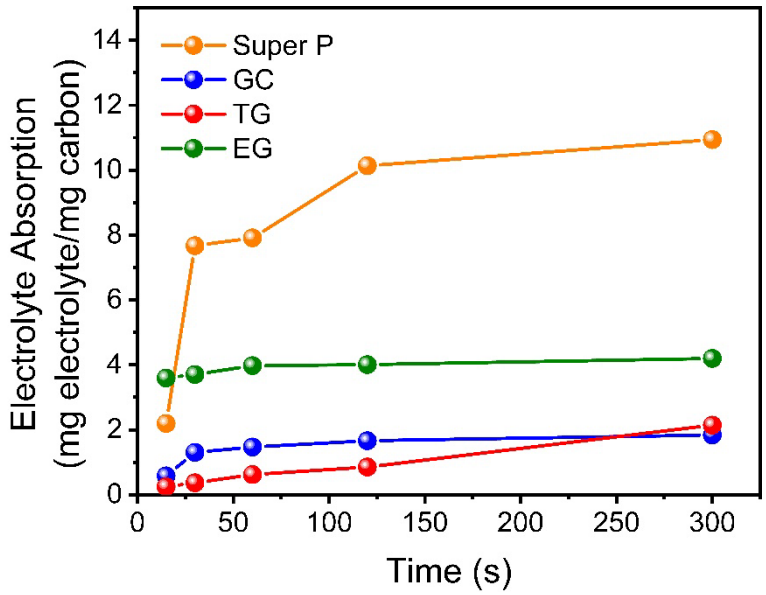

Figure 3-6. Electrolyte absorption capabilities of EMD electrodes fabricated using different carbon conductive additives over time.

3.3.3 Properties of assembled Zn-C batteries

Next Zn-C batteries were assembled using EMD cathodes fabricated with different carbon conductive additives and Zn metal anodes in 1 M $ZnSO_4$ aqueous electrolyte. **Figure 3-7**a – d show their galvanostatic discharge curves in the voltage window of 1.5–0.7 V under current densities of 1.0, 0.5, 0.1, and 0.05 A g^{-1}, respectively. All discharge curves feature a typical discharge behavior of Zn-C batteries with an ohmic voltage drop (IR drop) at the beginning of discharge to a flat discharge plateau, followed by a voltage decrease to the cutoff voltage [203,

227, 228]. Under high current densities of 1.0 and 0.5 A g^{-1}, Zn-C cells containing graphitic carbon materials synthesized by CDM show significantly higher specific discharge capacities than that contains Super P. The TG cell delivers a specific capacity 1.4 times that of the Super P cell at 1.0 A g^{-1}. In comparison, minor differences were observed under the lower current density of 0.1 A g^{-1}. The specific capacity varies from 99 to 104 mAh g^{-1} in a sequence of GC cell < TG cell < EG cell < Super P cell. Under the lowest current density of 0.05 A g^{-1}, the specific capacity of the GC, TG, and EG cells is 122, 114, and 109 mAh g^{-1}, respectively, comparable to the Super P cell at 124 mAh g^{-1}. **Figure 3-7**e compares their specific capacity under different discharge current densities. All batteries experience a capacity decrease with the increase of discharge current density from 0.05 to 1.0 A g^{-1}, particularly the Super P cell exhibits the most significant drop. **Figure 3-7**f shows Nyquist plots of EIS spectra of the Zn-C batteries. The intercept of the impedance curve with the real axis denotes ohmic resistance. As displayed in **Figure 3-7**f inset, the Super P cell shows a larger ohmic resistance, consistent with its lower measured in-plane electrical conductivity of the EMD electrode. Negligible differences were observed in the ohmic resistance of TG, EG, and GC cells. Further, based on the semicircles in the high-frequency region, TG, EG, and GC cells have much lower charge transfer resistance than the Super P cell. Previous studies have reported that the network of carbon conductive additives may not fully cover all EMD particles due to Super P particle agglomeration [229, 230]. In contrast, the other three types of carbon particles seem to fill the gaps between EMD particles more efficiently [231]. The charge transfer resistance of the GC cell is close to that of TG, and EG cells, suggesting that Fe residues in GC have negatable roles in facilitating electron transfer at electrode/electrolyte interfaces, despite the higher in-plane conductivity of EMD electrodes fabricated using GC.

Overall, Zn-C batteries fabricated using the graphitic carbon materials synthesized by CDM perform better than those fabricated using Super P under high discharge current densities

and are comparable under low discharge current densities. The improved performance at high discharge rates is related to the higher electrical conductivity of the CDM synthesized carbon materials and the effective electronic networks formed by them in batteries.

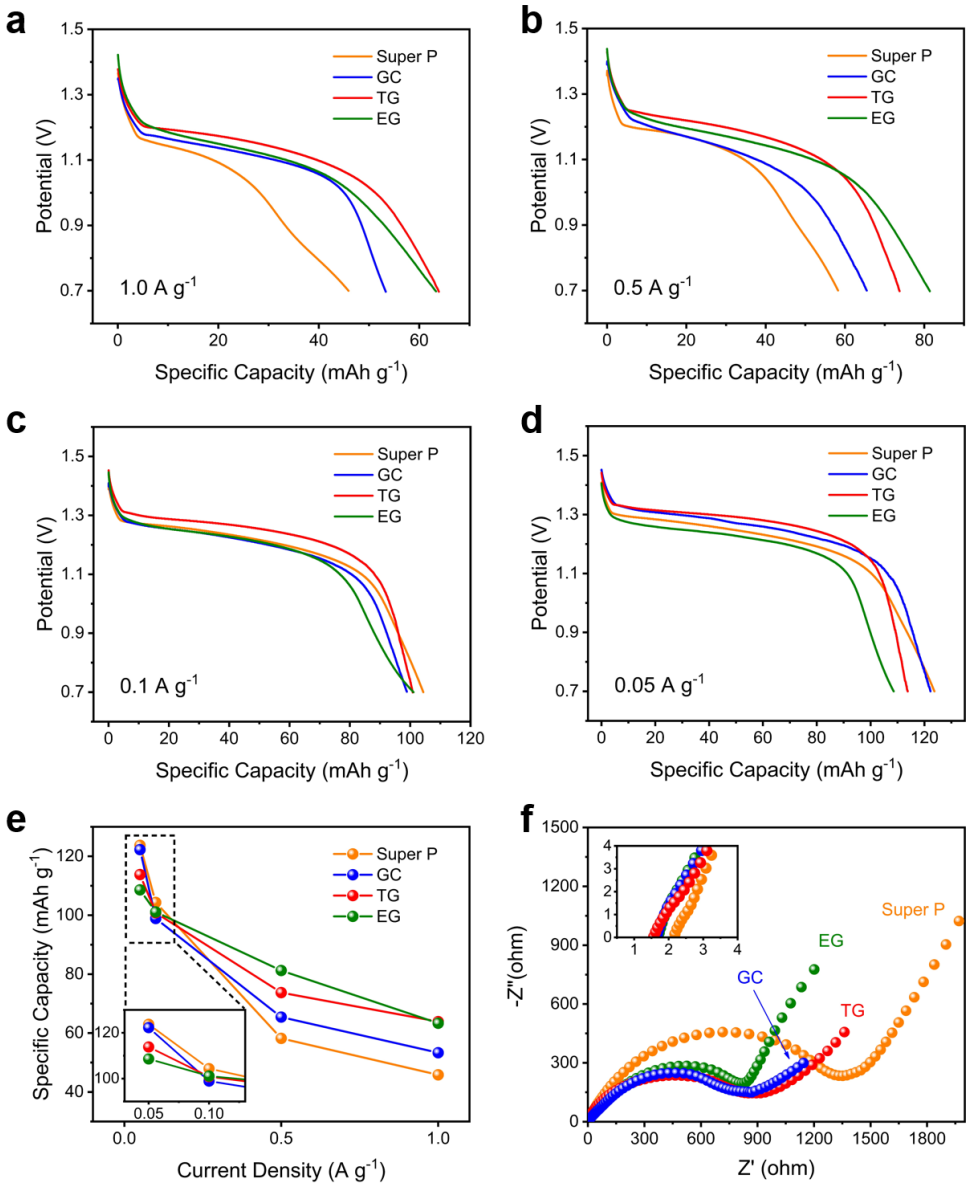

Figure 3-7. Galvanostatic discharge curves of Zn-C batteries fabricated using different carbon conductive additives under the discharge current density of (a) 1.0 A g^{-1}, (b) 0.5 A g^{-1}, (c) 0.1 A g^{-1}, and (d) 0.05 A g^{-1}. (e) The comparison of the specific capacity of Zn-C batteries under different discharge current densities. The inset shows a magnified plot at the low discharge

current density region. (f) Nyquist plots of Zn-C batteries. The inset shows the intercept of the impedance curve with the real axis.

The GITT technique was further utilized to investigate the voltage response of Zn-C batteries under intermittent operation conditions, which is more relevant for their practical working conditions [203]. As shown in **Figure 3-8**a, all cells are discharged under 0.05 A g^{-1} for 120 s followed by a 4 h rest, and this test cycle was repeated for 30 segments. **Figure 3-8**b shows the enlarged region of the GITT fragment at the 3rd test cycle, displaying the voltage relaxation process during the rest of the time. The instant voltage jump (IR drop) is correlated with ohmic and charge transfer resistance. The following gradual voltage change is associated with ion diffusion [232, 233]. TG and EG cells exhibit smaller IR drops of 26 and 27 mV, respectively, indicating lower internal resistances. The total voltage changes of Super P, GC, TG, and EG cells are 105, 94, 82, and 91 mV, respectively, showing a similar trend as their IR drops. The smallest voltage change of the TG cell can be attributed to its lowest resistance and better ion diffusion. The internal resistances of all cells increase with extended test time, which was calculated by Ohm's law, *i.e.*, $R=V/I$, where V (V) is the maximum voltage change in one segment, I (A) is the discharge current.[234, 235] As shown in **Figure 3-8**c, the Super P cell has the highest cell resistance and the fastest increasing rate, while the TG cell shows the lowest cell resistance and lowest increasing rate over the entire GITT segments.

Figure 3-8d compares the long-term stability of the Zn-C batteries fabricated using different carbon conductive additives over one month. The GC cell exhibits the largest OCV drop of 0.037 V, attributed to Fe residuals in GC, causing self-discharge or secondary reactions [236]. In contrast, an OCV drop of 0.020 V is observed for the EG cell, less than half of that for GC cell. The TG cell shows a negligible OCV drop of 0.001 V, better than the Super P cell at 0.014 V. The extremely low OCV drop of the TG cell suggests its excellent stability, which

may be attributed to the higher purity of TG, mitigating self-discharge or secondary reactions caused by Fe impurities. The improved stability of TG and EG cells indicates that both purification methods have successfully removed Fe residues to avoid their detrimental effect on battery long-term performance. After the stability test, all Zn-C cells were galvanostatically discharged at 0.1 A g^{-1} to evaluate their discharge characteristics after a long-term placement. **Figure 3-9** shows that the discharge curves of Zn-C batteries are similar, with a specific capacity of around 95 mAh g^{-1} when discharging to 0.7 V.

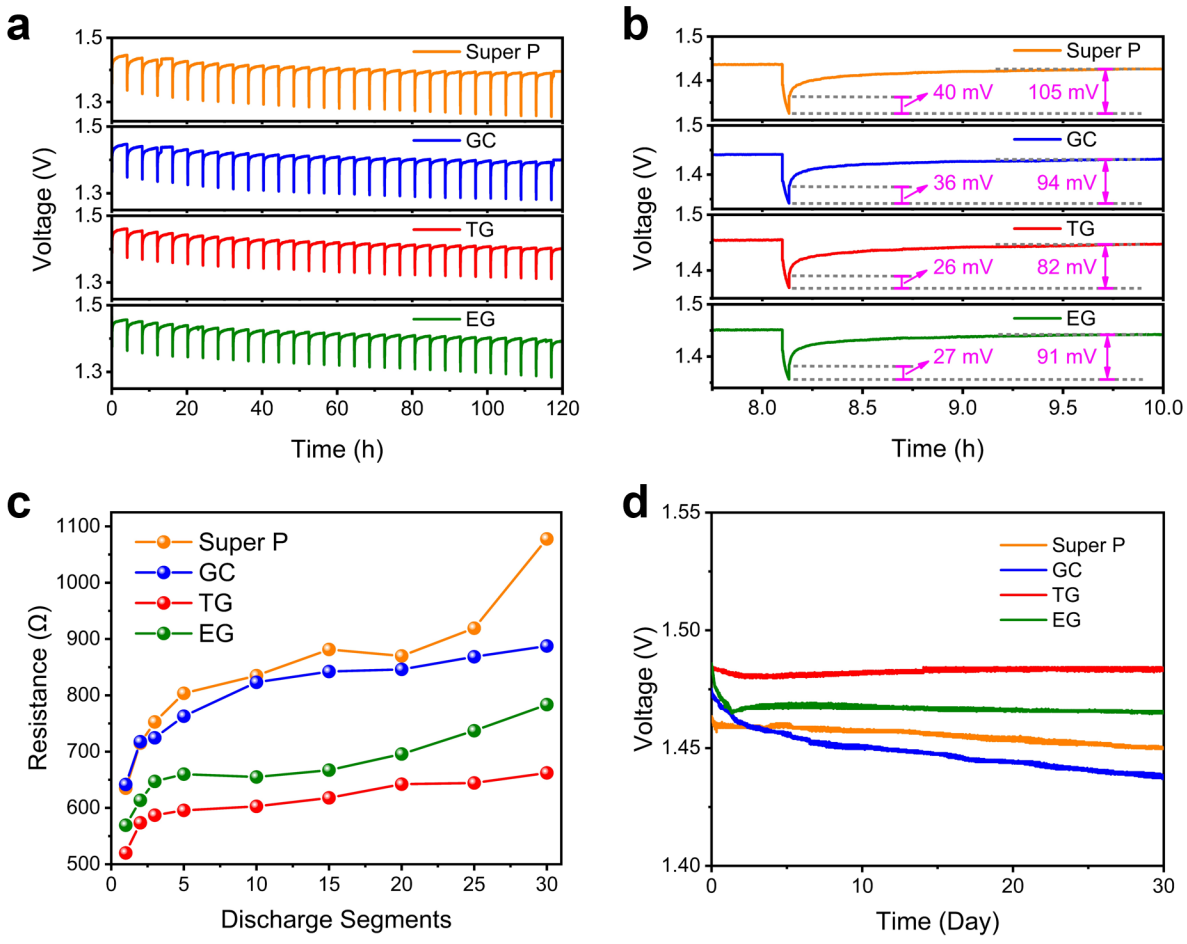

Figure 3-8. (a) GITT profiles of Zn-C batteries assembled using different carbon additives, (b) the enlargement of one GITT segment at the third test cycle, (c) cell resistances of Zn-C

batteries during 30 test cycles of GITT, and (d) OCV plots of Zn-C batteries in long-term stability tests over one month.

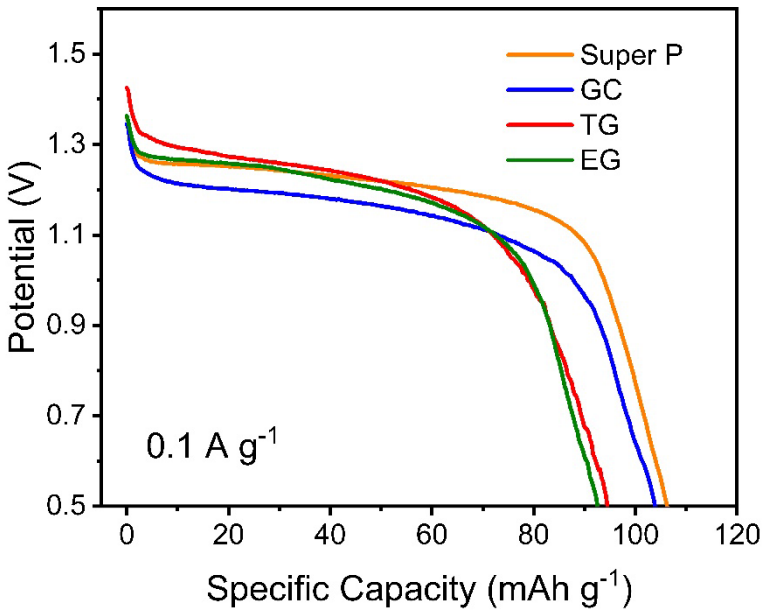

Figure 3-9. Galvanostatic discharge curves of Zn-C batteries under 0.1 A g^{-1} after their long-term stability test.

3.4 Conclusion

Graphitic carbon materials (GC) were synthesized as a co-product of H_2 by CDM using Fe ore catalysts. They were purified by the standard high-temperature thermal treatment at 2800 ^{o}C (TG) and the alternative electrochemical method (EG), increasing their carbon purity from 78.25 to 99.82 and 99.59 wt.%, respectively. They were evaluated as conductive carbon additives for Zn-C batteries. MnO_2 cathodes fabricated using TG or EG at the mass ratio of 7:2 show electrical conductivity of 98 and 90 S cm^{-1}, and their carbon electrodes have the electrolyte (1 M $ZnSO_4$) absorption capacity of 2.14 and 4.20 mg mg^{-1}, respectively. Zn-C batteries assembled using TG or EG exhibit a specific capacity of 114 and 109 mAh g^{-1} under

0.05 A g^{-1}, comparable to that with commercial carbon conductive additives (Super P). Importantly, they demonstrate better rate performance when the current density increases from 0.05 to 1.0 A g^{-1} due to their high electrical conductivity resulting from their graphitic structures. They also exhibit excellent performances under intermittent operation conditions and in long-term stability tests because the efficient removal of their Fe residues has prevented self-discharge behaviors. There is no significant difference between TG and EG, indicating both purification methods are efficient. Purified graphitic carbon materials from CDM are promising as efficient carbon conductive additives for batteries, which turn a solid by-product from CDM into a high-value-added commodity, increasing the economic viability of the CDM-based H_2 production process.

Chapter 4. Graphitic co-products of clean hydrogen production enabling high-rate-performance dual-carbon batteries

4.1 Introduction

Hydrogen (H_2) is a clean, efficient, eco-friendly energy vector widely used in ammonia synthesis, petroleum refining, and fertilizer production [187, 237, 238]. Currently, most current H_2 production methods, such as steam methane (CH_4) reforming, coal gasification, and partial oxidation of hydrocarbons, cause significant carbon dioxide (CO_2) emissions [239, 240]. CH_4 pyrolysis, which directly splits CH_4 into H_2 and solid carbon ($CH_4 \rightarrow 2H_2 + C$), is a promising alternative for H_2 production without emitting CO_2 [37, 45, 241-244]. The reaction products' mass ratio of H_2 to solid carbon is 1 to 3. Developing value-added applications for these large amounts of carbon materials can eliminate waste, and selling these carbon materials also significantly offsets H_2 production costs.

Lithium-ion batteries (LIBs) dominate the energy storage device market of portable electronics and electric vehicles. However, their safety concerns, high cost, and material resource shortages have motivated the development of various alternative batteries [245-247]. Among them, dual-ion batteries (DIBs) are one of the attractive candidates owing to their low cost, environmental friendliness, and high working voltage (*e.g.*, >4.5 V) [248-252]. Unlike rocking-chair-type LIBs driven by Li^+ shuttling between a cathode and an anode, DIBs work on a principle where both cations and anions in an electrolyte engage in the energy storage process. The cathode materials used in DIBs are mainly graphite, which can lower the cost of cathodes by around 70 % compared to lithium iron phosphate ($LiFePO_4$) utilized in cathodes for LIBs [245]. Anode materials in DIBs are usually metal oxides or metals containing Li, K, Na, Al, Mg, Ca, or Zn [246, 251, 253-259]. Non-Li alkali-metal or multivalent cations are

preferred due to their high energy storage capacity and abundance compared to Li [247]. However, metal-based anode materials still face various challenges. For example, metal oxide anodes may drag down the cell voltage, and metallic anodes come with the issues of fast dendrite formation and significant volume expansion [260]. Alternatively, supercapacitors are another type of energy storage device with the advantages of high power density and fast charge/discharge rates that are used in consumer electronics and emergency power supplies [261-263]. Although both cations and anions are involved in the energy storage of DIBs and supercapacitors, supercapacitors have a different energy storage mechanism, involving the physisorption of ions on electrode surfaces to form an electric double layer and fast electrode surface redox reactions. Electrode materials used in supercapacitors are usually activated carbon (AC), graphene, or carbon nanotubes with a large specific surface area (*e.g.*, >2000 m^2 kg^{-1} for AC) and high electrical conductivity [261-265]. Supercapacitors' low energy storage density is their key drawback [251, 261, 263, 266, 267].

Dual-carbon batteries (DCBs) are a subcategory in DIBs, utilizing carbon materials as both cathode and anode materials. They offer unique advantages, such as lower cost, better sustainability, and high working voltage (>4.5 V) [245-247, 250, 268, 269]. DCBs inherit the "non-rocking-chair" mechanism that both cations and anions contribute to energy storage. As illustrated in **Figure 4-1**a, anions intercalate into the cathode, and Li^+ inserts into the anode simultaneously during the charging process. Both anions and Li^+ de-intercalate from electrodes during discharging. Carbon material electrodes are crucial components of DCBs. Graphite cathodes can enable high working voltages for DCBs without using transition metals, considerably decreasing battery costs [245]. However, graphite cathodes often suffer from severe structural deterioration upon repeated charge and discharge, resulting in unsatisfied cyclability (*i.e.*, short cycling life) and poor rate performance (*i.e.*, quick loss of energy storage capacity under high charge/discharge current densities) [247, 260, 270]. Some recent studies

have optimised electrolytes to improve the rate performance of DCBs [270-273]. Previous studies also showed that lowering particle size and increasing the surface area of electrode materials can improve DCBs' rate performance [274, 275]. Carbon materials produced by CH_4 pyrolysis using iron (Fe) ore catalysts for H_2 production have graphitic structures with certain porosity and a relatively moderate specific surface area (*i.e.*, 10–30 m^2 g^{-1}) [276, 277]. It is speculated that such carbon materials might work efficiently in DCBs.

Herein, I demonstrate that carbon by-products from clean H_2 production via methane pyrolysis can serve as efficient anode and cathode materials in DCBs. Carbon materials were first synthesized using low-cost Fe ore as catalysts. Next, these carbon materials were purified by a standard high-temperature thermal treatment method and an alternative room-temperature electrochemical method. A comprehensive set of characterization tools characterized their physicochemical properties. Afterward, I systematically compared the performance of cathodes and anodes of Li/graphite half cells fabricated using purified carbon materials and two types of commonly used commercial graphite (natural and synthetic graphite). Their energy storage performance was further correlated with their structural characteristics. Last, DCB full cells were assembled using the two types of purified graphitic carbon from methane pyrolysis, which delivered the energy storage capacity of 75.1 and 74.7 mAh g^{-1} at 5 C rate (1 C = 100 mA g^{-1}) with a high capacity retention ratio of 79.2 and 93.4 % after high rate operations over 50 C, respectively. Further, they also demonstrated excellent cycling stability under 5 C over 300 charge/discharge cycles. These results show the great potential of the carbon co-products from the CH_4-pyrolysis-based clean H_2 production process as efficient electrode materials for high-rate performance DCBs.

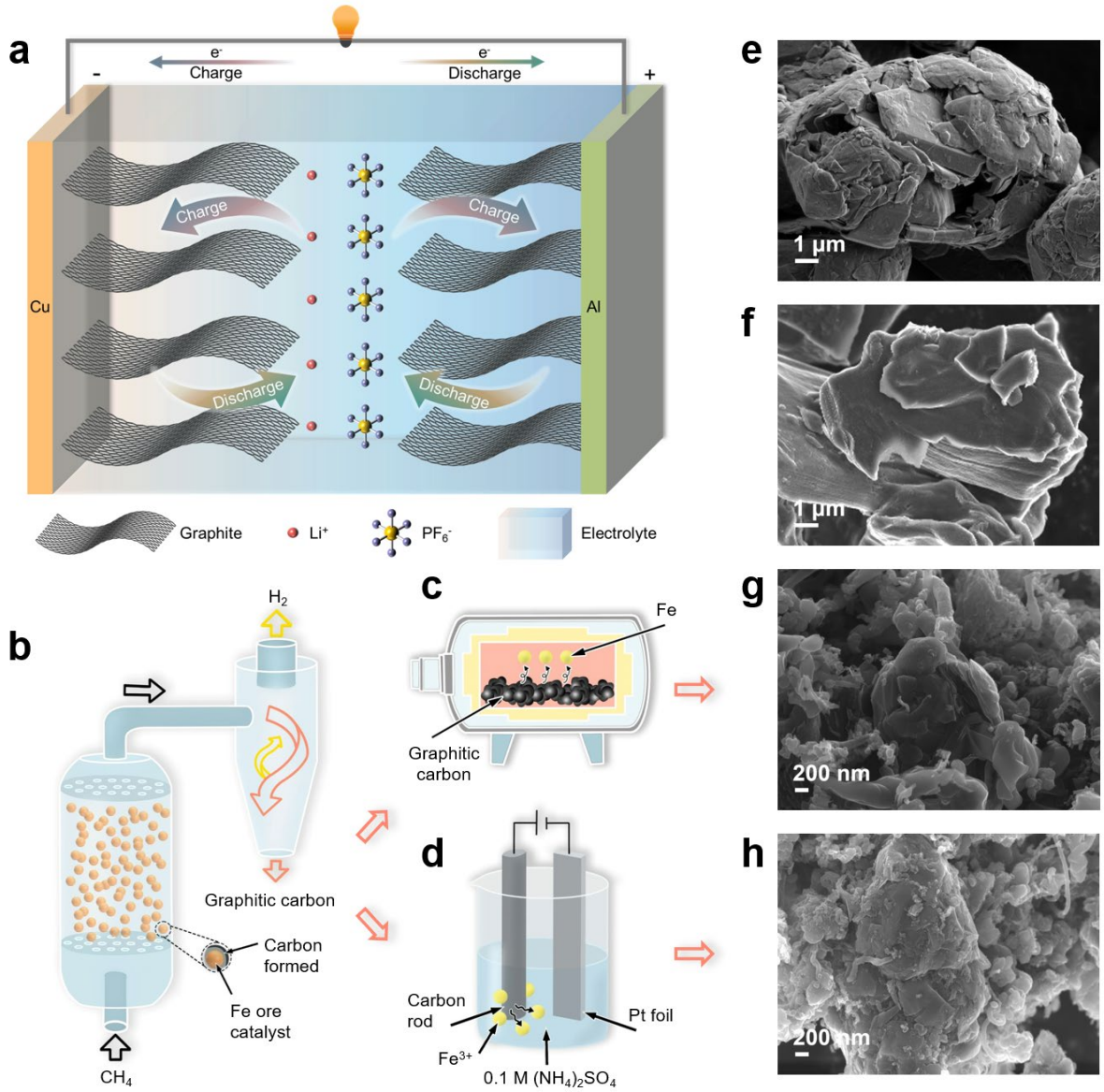

Figure 4-1. Schematic illustrations of (a) a dual-carbon battery, (b) the synthesis of graphitic materials encapsulating Fe ore particles by catalytic CH_4 pyrolysis, (c) high-temperature thermal purification, and (d) room-temperature electrochemical purification. SEM images of graphitic materials used in this study: (e) natural graphite, (f) synthetic graphite, (g) high-temperature purified, and (h) electrochemically purified graphitic materials from CH_4 pyrolysis.

4.2 Experimental section

4.2.1 Material synthesis

As illustrated in **Figure 4-1**b, graphitic materials were synthesized by catalytic methane pyrolysis using a low-cost Fe ore catalyst in a fluidized bed reactor. The elemental composition of the Fe ore was analysed by X-ray fluorescence spectroscopy (XRF). **Table 4-1** shows that it mainly contains about 68.7 wt.% Fe, 0.55 wt.% sodium oxide (Na_2O), and 0.32 wt.% magnesium oxide (MgO). Fe ore (150 g) was milled to a particle size of 100–200 μm. The Fe ore catalyst was fed into a 2-inch diameter fluidized bed reactor, which was operated at 890 ºC and 6 bar with a CH_4 gas feed rate of 5.5 $m^3\ h^{-1}$ (standard conditions) and a gas space velocity of 12.22 L g_{cat}^{-1} for about 6 h. CH_4 was catalytically decomposed into H_2 and solid carbon upon interacting with suspended Fe ore particles. Solid carbon deposited on Fe surfaces disintegrated Fe ore particles into nano-fragments with lower mass density. These nano-fragments coated with carbon materials were carried out of the reactor by the CH_4/H_2 gas mixture, then separated in a cyclone separator and collected at the bottom of the cyclone (**Figure 4-1**b).

Table 4-1. XRF analysis of Fe ore catalyst used for the methane pyrolysis process.

Oxides	Composition (wt.%)
Fe_2O_3	98.23
Na_2O	0.55
MgO	0.32
Mn_3O_4	0.19
SO_3	0.07
SiO_2	0.04

P_2O_5	0.04
TiO_2	0.03
Cr_2O_3	0.03
CuO	0.03
ZrO_2	0.02
Al_2O_3	0.01
K_2O	0.01
CaO	0.01
V_2O_5	0.01
NiO	0.01
ZnO	0.01
SrO	0.01
BaO	0.01
PbO	0.01

The collected carbon/Fe mixtures were first purified using a standard thermal purification method commonly used for graphite materials [214-216]. As illustrated in **Figure 4-1**c, a high-temperature furnace was used to heat samples at 3000 ^oC for 0.5 h with a temperature ramping rate of 10 ^oC min^{-1}. Fe particles trapped inside carbon materials were removed, and the resulting thermally purified carbon materials were denoted as "TG". Alternatively, the carbon/Fe mixtures were purified using an electrochemical method, similar to electrochemical exfoliation methods used to synthesize graphene from graphite materials [219, 278, 279]. As illustrated in **Figure 4-1**d, carbon/Fe mixtures were compressed into a carbon rod and utilized as a positive working electrode. A platinum foil served as a negative counter electrode. Both electrodes were

immersed in a 0.1 M ammonium sulfate aqueous solution electrolyte. A direct current (DC) power of 10 V was applied to the electrodes, and charged ions in the electrolyte were intercalated into the graphene layers of the carbon rod. Encapsulated Fe particles slowly leached into the electrolyte over 20 h. Afterward, the carbon rod was washed with water and dried, and the resulting carbon materials were denoted as "EG". Two commercial graphite materials, natural graphite (NG) and synthetic graphite (SG) (Targray Technology International, Inc.), were also studied as references.

4.2.2 Material characterization

The elemental composition of Fe ore catalysts used was acquired by a wavelength dispersive XRF spectrometer (PANalytical AXIOS, PW2400) equipped with a 4-kW X-ray source. The morphology of graphite materials was first examined by SEM using a Zeiss Gemini Ultra Plus microscope. Their microstructures were further investigated by TEM (JEOL, JEM-2100), operated at an accelerating voltage of 200 kV. HR-TEM images were obtained by an HR-TEM microscope (Thermo Fisher Scientific Spectra 300). The particle size of graphite materials dispersed in ethanol was analysed by a particle size analyser (Malvern Mastersizer 3000). The surface area of graphite materials was measured by N_2 physisorption using a pore size analyser (Quantachrome Autosorb iQ). Their pore size distribution was calculated using N_2 physisorption isotherms by a DFT method. Their chemical properties were characterized by Raman spectroscopy on a Renishaw Raman spectrometer (inVia Reflex) under a 532 nm excitation laser. Their crystalline structures were studied by XRD (PANalytical X'Pert PRO) equipped with a Cu Kα X-ray source. Their surface functionalities were examined by an XPS analyser (Specs PHOIBOS 100) with an X-ray excitation photon energy of 1486.6 eV. TGA was conducted to determine the purity of graphite materials using a thermogravimetric analyser

(TA Instruments Q500) in the temperature range of 35 to 950 ºC. Their elemental compositions were further detected by ICP-OES (Perkin Elmer Avio 500) and XRF (PANalytical Minipal4).

4.2.3 Electrode fabrication and battery cell assembly

The four types of graphite materials, TG, EG, NG, and SG, were used as active materials to fabricate electrodes. 80 wt.% active materials, 10 wt.% conductive additives (Super P, Thermo Fisher), and 10 wt.% sodium carboxymethyl cellulose (Sigma-Aldrich) were mixed in deionized water. The formed slurry was cast over an aluminum (Al) foil (thickness ~15 μm) or a copper (Cu) foil (thickness ~10 μm) to fabricate cathodes and anodes, respectively. The electrodes were dried at 120 oC for 12 h in a vacuum furnace. The mass loadings of active materials on the cathodes and anodes were around 2.0 and 1.5 mg cm^{-2}, respectively. CR2032-type coin cells were assembled to evaluate electrode electrochemical performances. Half cells consisted of different graphite electrodes as a working electrode, a lithium (Li) foil (thickness ~0.22 mm) as a counter electrode, and a glass fibre separator (Whatman GF/A). Around 200 μL 1 M lithium hexafluorophosphate ($LiPF_6$) in ethyl methyl carbonate (EMC) was used as an electrolyte and wetted with the separator. For DCB full cells, two graphite electrodes were used as cathode and anode, respectively, with a mass ratio of active materials in the cathode and anode at 1:1. They were separated by the glass fibre separator immersed with 200 μL electrolyte. All DCB cells were assembled in a glovebox under an argon (Ar) atmosphere with oxygen and moisture levels lower than 0.01 ppm.

4.2.4 Electrochemical measurement and characterization

Electrochemical measurements were performed in the voltage range of 3.0–5.2 V for cathode half cells and DCB full cells and 0.001–3 V for anode half cells. Galvanostatic charge-

discharge (GCD) tests were conducted using a battery testing system (LANHE) at room temperature (25 ºC). Rate performance tests for cathode half cells and DCB full cells were carried out under the current densities of 1–50 C. Note that most of the reported DCB studies used 100 mA g^{-1} as a basic rate for tests [272, 280-282]. Therefore, in this study, the same value (1 C = 100 mA g^{-1}) was used for the cathode side and DCBs. Anode half cells were evaluated at 0.1–10 C rates (1 C = 372 mA g^{-1} for the anode side). CV measurements for cathode half cells were recorded at different scan rates from 0.10 to 1.00 mV s^{-1} on an electrochemical workstation (CHI 760D). EIS analysis was also collected by the electrochemical workstation in a frequency range between 10^5–0.1 Hz with an amplitude of 10 mV.

Cathode half cells were disassembled in the glovebox after the rate performance tests to study the morphology and structure evolutions of graphite materials in cathode electrodes. The cycled cathodes were rinsed with dimethyl carbonate solvent several times to remove residual salts. SEM (Zeiss, Gemini Ultra Plus) and XRD (PANalytical X'Pert PRO) were used to compare the morphology and crystal structure changes in fresh and cycled graphite electrodes.

4.2.5 Calculations of energy density and power density of DCB full cells

The capacity of DCB full cells (C_{full}) is estimated as shown below [283, 284]:

$$C_{full} = \frac{C_{cathode} \times m_c}{m_c + m_a}$$

where $C_{cathode}$ (mAh g^{-1}) is the gravimetric capacity of the cathode, which can be obtained from the results for rate capability tests under different rates. m_c and m_a is the mass of active materials at the cathode and anode, respectively. Since the mass ratio of active materials in cathode and anode is 1:1, the above equation can be simplified as:

$$C_{full} = \frac{C_{cathode}}{2}$$

The energy density of full cells (E_{full}) can be calculated as:

$$E_{full} = C_{full} \times V_m$$

where V_m (V) is the medium discharge voltage of the cell discharging process at different current densities I_c (mA g^{-1}), which can be obtained from the battery testing system (LANHE).

The power density of full cells (P_{full}) can be calculated as:

$$P_{full} = \frac{E_{full}}{t}$$

where t (h) is the discharging time.

It should be noted that different considerations have been taken to estimate the energy density of DCBs. Several studies do calculations based on active material mass in both the anode and cathode [272, 283-286]. Meanwhile, some studies considered the total electrode mass [270, 287]. Thus, full cells' energy density and power density are also calculated based on the entire mass of the anode and cathode electrodes. The full cell capacity (C'_{full}) is calculated as:

$$C'_{full} = \frac{C_{cathode} \times m_c}{m'_c + m'_a}$$

where m'_c and m'_a are the entire mass of cathodes and anodes, respectively. Since the active materials account for 80 % of anode and cathode electrodes, the full cell capacity can be simplified as:

$$C'_{full} = \frac{C_{cathode}}{2.5}$$

The energy density (E'_{full}) and power density (P'_{full}) of full cells can be calculated as:

$$E'_{full} = C'_{full} \times V_m$$

$$P'_{full} = \frac{E'_{full}}{t}$$

4.3 Results and discussion

4.3.1 Characteristics of graphitic carbon materials

The morphology of the four types of graphitic materials was first characterized by scanning electron microscopy (SEM). **Figure 4-1**e and f show that NG and SG display typical compact graphite structures with large particle sizes of around 10 μm. In contrast, TG and EG have smaller particle sizes, as shown in **Figure 4-1**g and h. TG displays a relatively smooth surface with apparent carbon flakes, while EG shows a rougher surface with irregularly shaped particles. Transmission electron microscope (TEM) images in **Figure 4-2**a – c show that unpurified carbon/Fe mixtures contain Fe particles of around 15–20 nm in diameter encapsulated by graphitic layers in an onion-like structure. TG and EG exhibit hollow onion-like carbon shells, indicating that thermal and electrochemical purification methods have removed Fe particles. The graphitic structures of TG and EG were further analysed using high-resolution TEM (HR-TEM), as shown in **Figure 4-2**d and e. The details are discussed in a later section. The particle size distribution of the graphitic materials measured by a particle size analyser is shown in **Figure 4-3**. The median diameter (D_{50}) of NG, SG, TG, and EG is 10.9, 9.1, 3.8, and 3.5 μm, respectively, consistent with their SEM images in **Figure 4-1**.

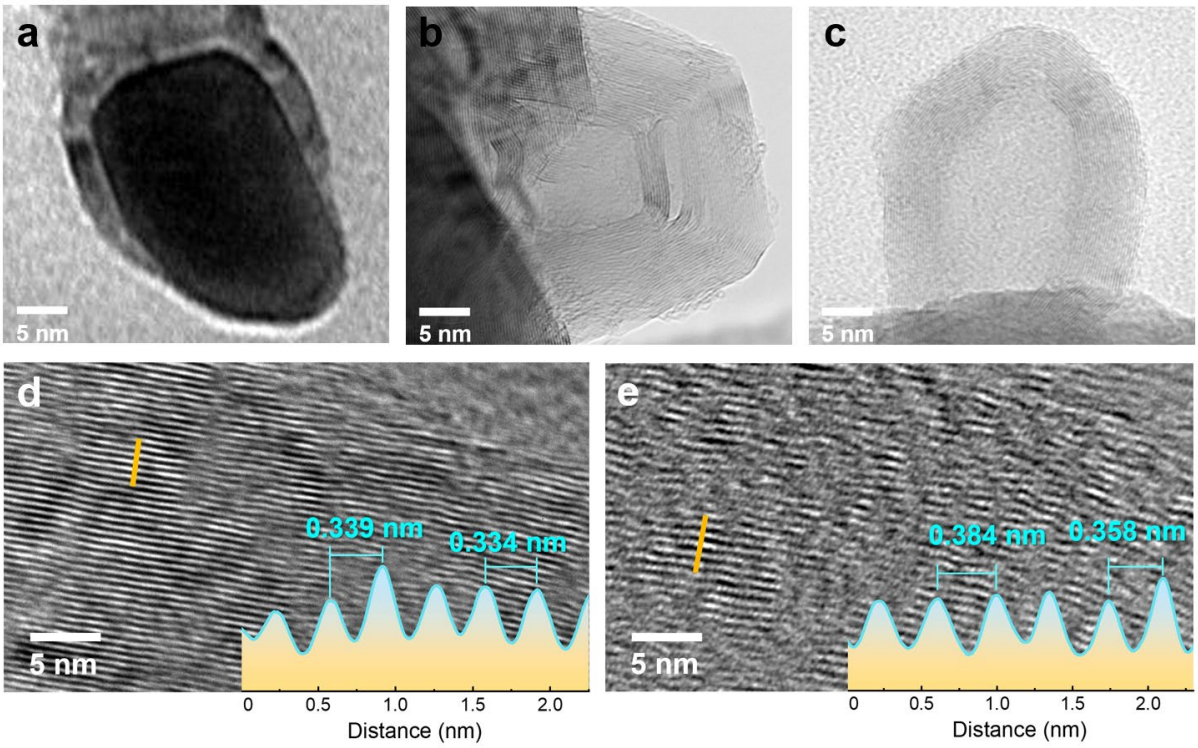

Figure 4-2. TEM images of (a) graphitic carbon encapsulating a Fe particle produced in the methane pyrolysis process, (b) TG, and (c) EG. HR-TEM images of (d) TG and (e) EG with their corresponding interplanar distances.

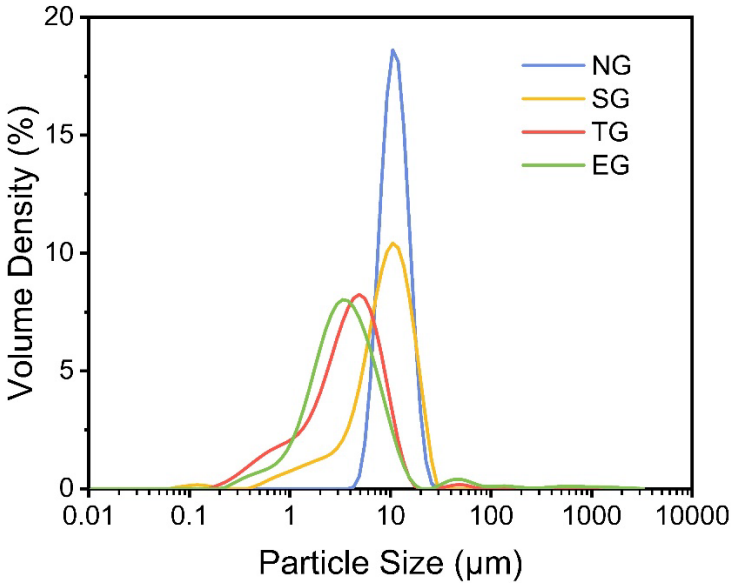

Figure 4-3. Particle size distribution profiles of graphitic carbon materials used in this study: NG, SG, TG, and EG.

Their specific surface area (SSA) and pore structure were studied by nitrogen (N_2) physisorption, and their isotherms are shown in **Figure 4-4**a. EG displays the largest SSA of 38 m^2 g^{-1}, which can be attributed to the partial exfoliation of graphene layers and the introduction of defects in carbon structures during the electrochemical purification [274]. TG also shows a large SSA of 23 m^2 g^{-1}, while NG and SG have much smaller SSA of 2.0 and 1.3 m^2 g^{-1}, respectively. Their pore size distribution was analysed by the density functional theory (DFT) method and shown in **Figure 4-4**b. TG and EG exhibit multimodal distributions of abundant mesopores with widths in the 2 to 40 nm range and moderate micropores of diameters around 1 to 2 nm, indicating their mesoporous structures. NG and SG possess relatively less peaky pore size distributions, with two prominent peaks at around 3 and 30 nm. Consequently, the average pore sizes for NG and SG are 29 and 2.8 nm, respectively. Although the peak positions for TG and EG are similar, TG has a much larger average pore size of 36 nm compared to EG of 3.8 nm, which suggests that the pore structure of TG has been restructured

during high-temperature treatment with the closure of micropores. TG and EG show total pore volumes of 0.13 and 0.16 m^3 g^{-1}, respectively, more than one order larger than those of NG and SG with 0.004 and 0.012 m^3 g^{-1}, respectively. Considering that pore structures of graphitic materials are favourable to providing access to electrolytes, enabling ion adsorption, and preventing volumetric changes during ion intercalations, TG and EG with presented pore structures are expected to be suitable electrode materials for DCBs [245, 247, 250].

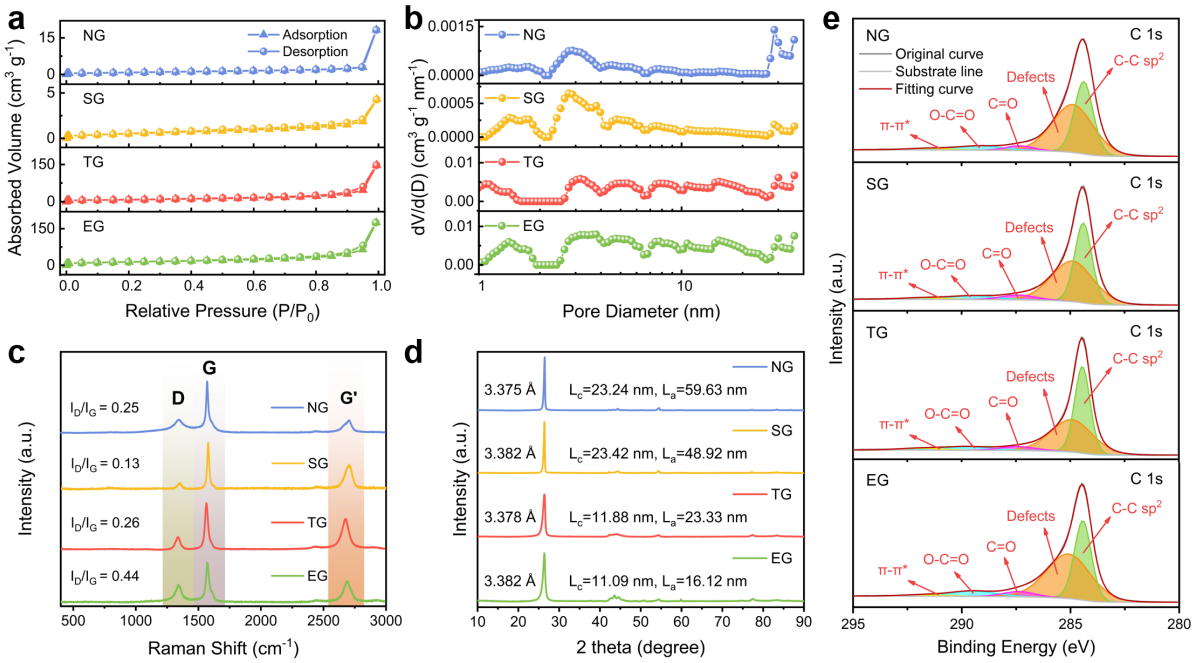

Figure 4-4. Physiochemical properties of graphitic materials used in this study. (a) N_2 physisorption isotherms, (b) pore size distribution, (c) Raman spectra, (d) XRD profiles, and (e) XPS spectra of C 1s of NG, SG, TG, and EG.

Their chemical structures were characterized by Raman spectroscopy. **Figure 4-4**c shows that their Raman spectra have three typical peaks of carbon materials: the G band from in-plane vibrations of crystalline graphite, the D band from disordered structures in the graphitic lattice,

and the G' band correlated to the number of graphene layers and their stacking order [220, 221]. The intensity ratio between D and G bands (I_D/I_G) often indicates defect density, structural vacancies, and/or surface functional groups in carbon materials. SG shows the smallest I_D/I_G value of 0.13, suggesting its highest structure regularity with few defects. TG and NG have similar I_D/I_G values around 0.25–0.26, while EG exhibits a larger value of 0.44, indicating a higher density of defects.

Their X-ray diffraction (XRD) patterns are shown in **Figure 4-4**d. The interlayer spacing between graphene sheets (d_{002}) was calculated using Bragg's equation:

$$2dsin\theta = n\lambda$$

where θ is the peak position, n is the order of diffraction (n = 1), and λ is the wavelength of the incident X-ray (0.15406 nm). TG and EG have a slightly larger d_{002} of 0.3378 and 0.3382 nm, respectively, than NG at 0.3375 nm. The larger interlayer spacing usually benefits ion penetration into the graphitic structure [288]. The apparent crystalline length (L_a) and thickness (L_c) were estimated using the Scherrer equation:

$$L = \frac{K\lambda}{\beta cos\theta}$$

where λ is the wavelength of the incident X-ray (0.15406 nm), β is the full width at half-maximum of the XRD peaks, and the K value is 1.84 and 0.90 for the (100) and (002) peaks of carbon materials, respectively [288]. The results are listed in **Table 4-2**. NG and SG have much larger L_a and L_c than TG and EG. The graphitic structures of TG and EG were further analysed using HR-TEM, as shown in **Figure 4-2**d and e. TG exhibits uniform interlayer spacing values around 0.334–0.339 nm, revealing a similar structure to graphite (d_{002} of 0.335 nm) [247]. In contrast to TG, EG shows larger and uneven d_{002} values from 0.384 to 0.358 nm, indicating that graphene sheets inside EG have experienced expansion to different extents. There are consistent findings of a larger d_{002} in EG than in TG by HR-TEM and XRD. The larger d_{002} in

EG is likely induced by the leaching of Fe from graphitic structures and the intercalation of electrolyte ions during the electrochemical purification, which expands the interlayer spacing between graphene layers [219, 278, 289-291]. It should be noticed that the d_{002} values obtained from XRD are smaller than those from HR-TEM because XRD provides the average interplanar spacing of bulk materials while HR-TEM reflects localized areal information [266].

Table 4-2. A summary of the physiochemical properties of the graphitic materials used in this study.

Graphitic materials	D_{50} (μm)	SSA ($m^2\ g^{-1}$)	V_{pore} ($cc\ g^{-1}$)	d_{pore} (nm)	Raman I_D/I_G	d_{002} (nm)	L_a (nm)	L_c (nm)	T_{TGA} (°C)	P_{carbon} (wt.%)
NG	10.9	2.0	0.012	29	0.25	0.3375	59.63	23.24	781	98.98
SG	9.10	1.3	0.004	2.8	0.13	0.3382	48.92	23.42	786	99.24
TG	3.82	23	0.13	36	0.26	0.3378	23.33	11.88	719	99.32
EG	3.45	38	0.16	3.8	0.44	0.3382	16.12	11.09	686	97.59

D_{50}: median diameter (μm), **SSA**: specific surface area ($m^2\ g^{-1}$), V_{pore}: total pore volume ($cc\ g^{-1}$), d_{pore}: average pore size (nm), d_{002}: interlayer spacing between graphene sheets (nm), L_a: crystalline length (nm), L_c: crystalline thickness (nm), T_{TGA}: TGA main peak temperature (°C), P_{carbon}: carbon purity (wt.%)

Surface functionalities of the graphitic materials were studied by X-ray photoelectron spectroscopy (XPS). From the XPS survey scans shown in **Figure 4-5**, all four materials display similar features, with a large sharp peak and a much smaller peak indexed to C and O elements, respectively. The atomic O contents for NG, SG, TG, and EG are detected to be 3.2 %, 3.0 %, 2.0 %, and 5.9 %, respectively. This indicates that TG has the highest C-to-O ratio (C:O) of 49, followed by SG at 32, NG at 30, and EG at the lowest ratio of 16. **Figure 4-4**e shows the C 1s XPS spectra, which were deconvoluted into the following bands: C in graphite (C-C) at 284.4 eV, defects at 284.9 eV ascribed to C atoms no longer in the regular structure, C doubly bound to O (C=O) at 287.3 eV, C bound to two O (O-C=O) at 289.5 eV, and the characteristic shakeup line of C in aromatic structure at 291.7 eV (π-π^* satellite) [174, 273, 291, 292]. Among the four materials, EG has larger peaks for defects, O-C=O and C=O bands, suggesting EG has a more defective surface with more O-containing functional groups. In contrast, TG has a smaller peak for defects and a larger peak for the C-C band, corresponding to a less defective surface with limited O functional groups.

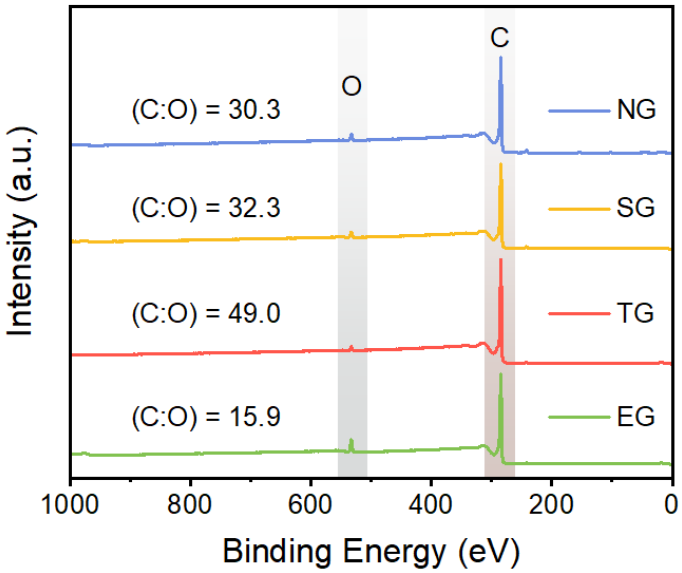

Figure 4-5. XPS survey of graphitic carbon materials used in this study: NG, SG, TG, and EG. (C:O): the atomic ratio of C to O.

Impurities in the graphite materials were first analysed by thermogravimetric analysis (TGA) up to 950 ºC. Their weight loss profiles and derivative thermogravimetry (DT) profiles are shown in **Figure 4-6**. TG has the lowest ash content of 0.68 wt.%, indicating the highest carbon purity of 99.32 wt.%, even higher than NG and SG at 98.98 and 99.24 wt.%, respectively. EG has a lower purity of 97.59 wt.%, resulting from Fe residues trapped in carbon structures. Further, using the standard elemental analysis method by inductively coupled plasma optical emission spectrometry (ICP-OES) involving intense acid treatments, it is still difficult to detect the remaining Fe in TG and EG because the remaining Fe particles are tightly encapsulated inside the completely intact carbon shells [243, 293, 294]. The details of the ICP-OES analysis are discussed as follows:

ICP-OES analysis was used to detect the elemental compositions of TG and EG. Before ICP-OES, sample pretreatments were performed. 20 mg of TG and EG were mixed with 10 mL of 70 % nitric acid (HNO_3), respectively. The mixtures were sealed in a hydrothermal kettle and were heated at 150 ºC for 6 h. After 6 h of heating, it was found that the graphitic materials could not be dissolved in the solution. 0.2 mL liquid was taken from the solution and diluted with deionized (DI) water. ICP-OES results for these sample solutions show zero Fe (ppm) detected. The experiment indicates that it is challenging for the Fe impurities to come out from the graphitic structures of TG and EG. This can be attributed to the fact that carbon shells tightly wrap the remaining Fe after thermal and electrochemical purifications with an onion-like structure, similar to the one shown in **Figure 4-2**a [243, 293, 294]. Thus, such Fe cannot easily break the intact carbon shells to escape.

XPS analysis also suggests that no Fe species are detected on the surface of these graphitic materials. Furthermore, XRF is used to detect all metallic elements embedded deep inside TG and EG. **Table 4-3** shows that EG has a low Fe concentration of 0.196 wt.%. Considering the remaining Fe is firmly encapsulated by the completely intact carbon shells. It is not easily

accessible to electrolyte ions; thus, it was considered these Fe would have negligible influences on the electrochemical performance of EG electrodes. TG shows an extremely low Fe concentration of 0.003 wt.% in XPS, approximating zero, indicating the more efficient removal of Fe by the high-temperature thermal treatment.

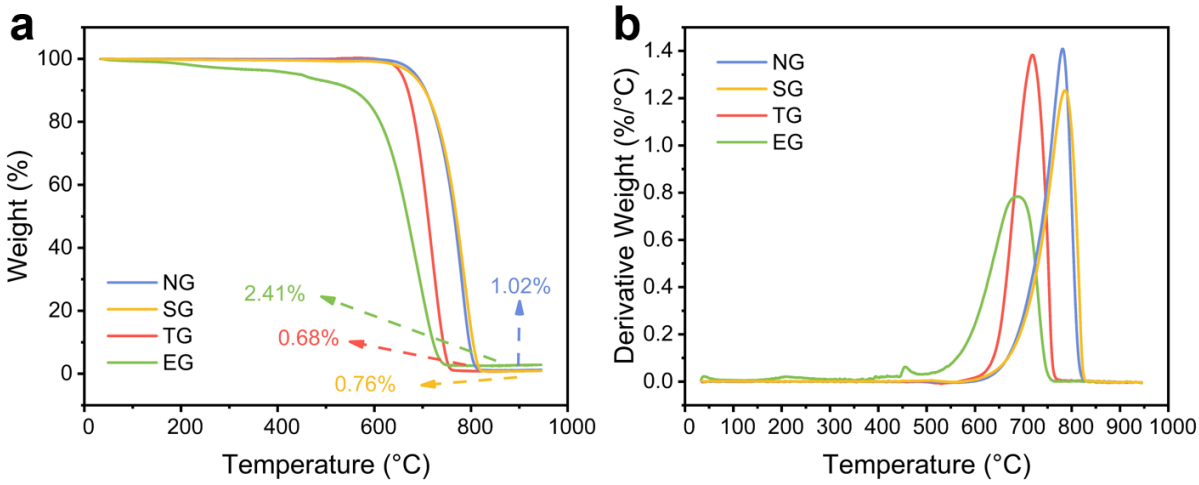

Figure 4-6. (a) TGA weight loss profiles and (b) DT profiles of different graphitic carbon materials: NG, SG, TG, and EG.

Table 4-3. XRF analysis of EG (left) and TG (right).

Elements	Composition (wt.%)	Elements	Composition (wt.%)
Fe	0.196	Mg	0.243
Mg	0.18	Al	0.031
Si	0.077	Ca	0.014
Ba	0.034	Mo	0.013
Al	0.03	Ti	0.009

Ca	0.028	Fe	0.003
Cl	0.012		
Pt	0.011		
Zn	0.007		
Mn	0.004		
Ti	0.003		

4.3.2 Electrochemical behaviors of graphitic cathodes

Electrolytes are an essential component of DCBs, acting as a medium for ion migration and as the source of the active ions. The electrolyte species and composition strongly influence the performance of DCBs. The performance of various electrolytes has been carefully compared [271, 295-299]. Ethyl methyl carbonate (EMC) was reported to be an appropriate solvent owing to its sufficient oxidative stability. EMC is also compatible with lithium hexafluorophosphate ($LiPF_6$), a common salt used in DCBs [266, 271, 297, 298]. Furthermore, the electrolyte of 1 M $LiPF_6$ in EMC has been found to display better electrochemical performances in terms of specific capacity and rate performance compared to several other solvents, such as dimethyl carbonate (DMC), diethyl carbonate (DEC), propylene carbonate (PC), and 1,3-dioxolane (DOL) [297, 299]. Therefore, 1 M $LiPF_6$ in EMC was selected as the electrolyte for the following DCB half-cell and full-cell studies.

Graphite/Li half cells was first assembled with the electrolyte of 1 M $LiPF_6$ in EMC to investigate the intercalation performance of anions into different graphitic cathodes. **Figure 4-7**a shows their typical galvanostatic charge-discharge (GCD) curves under the current density of 1 C within the voltage range from 3.0 to 5.2 V vs. Li/Li^+. All charge curves exhibit similar plateaus associated with the stage transformations in graphite intercalation compounds (GICs)

[296]. There are two obvious turning points at around 4.4 and 5 V on the charge curves and several others at about 4.8 and 4.4 V on the discharge curves, typical characteristics of graphitic cathodes [266, 274, 298]. The SG cathode half cell displayed a charge and discharge capacity of 104.6 and 89.7 mAh g^{-1}, respectively, representing a Coulombic efficiency of 86.1 %. The NG cathode half cell delivered a charge and discharge capacity of 111.6 and 82.8 mAh g^{-1}, respectively, with 74.2 % Coulombic efficiency. The irreversible charge capacity can be attributed to irreversible reactions on graphitic surfaces [298]. The TG cathode half cell delivered a comparable discharge capacity of 77.7 mAh g^{-1} and a higher efficiency of 89.4 %, indicating improved intercalation reversibility in TG. The EG cathode half cell displayed a sloping voltage profile without an apparent potential plateau on its discharge curve, a discharge capacity of 71.6 mAh g^{-1}, and an efficiency of 77.2 %. These results suggest that TG and EG can serve as cathode materials in DCBs, delivering comparable charge/discharge capacity and higher Coulombic efficiency than NG.

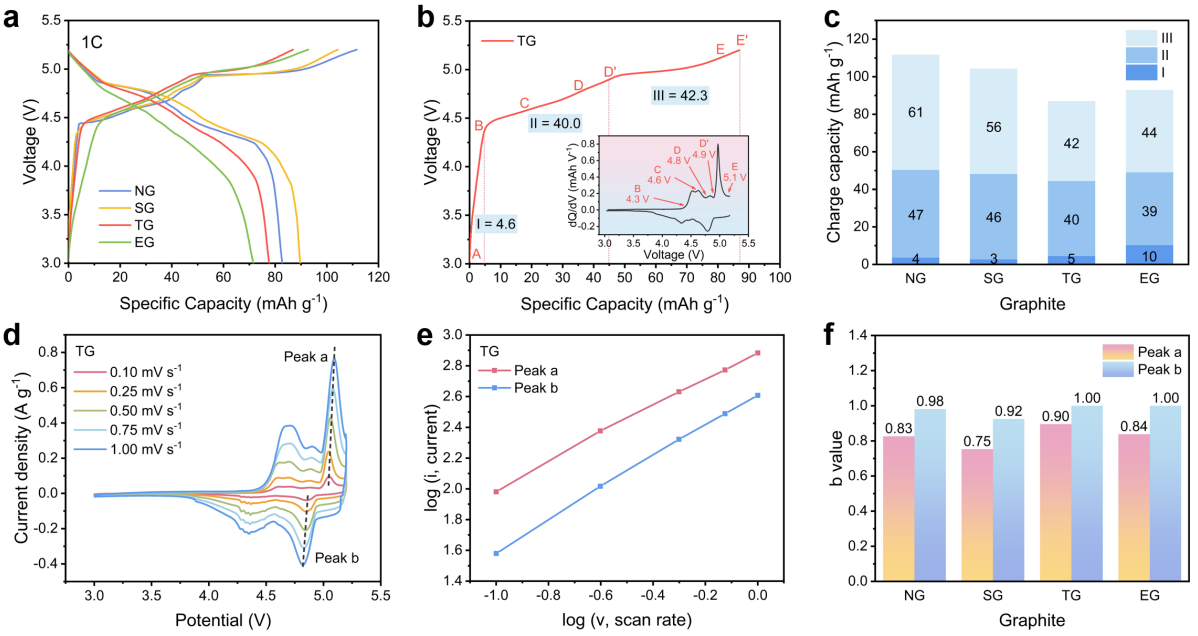

Figure 4-7. Electrochemical behaviors of graphitic cathodes in graphite/Li half cells. (a) GCD profiles of cathode half cells under 1 C. (b) A TG/Li half cell charge curve during anion intercalation segmented into three regions: I, II, and III. The labels from B to E correlate with the corresponding points on the *dQ/dV* curve shown as an inset. (c) Capacity in Region I, II, and III of NG, SG, TG, and EG during charging. (d) CV curves of TG/Li half cells at the scan rates of 0.1, 0.25, 0.5, 0.75, and 1 mV s^{-1}. (e) The corresponding log *i vs.* log *v* profiles used to determine the *b* values of TG cathodes. (f) The calculated *b* values of anion storage in different graphitic cathodes.

Next, differential capacity *vs.* voltage (*dQ/dV*) curves were plotted to study PF_6^- storage mechanisms in the four types of graphitic materials. As shown in the inset of **Figure 4-7**b, the peaks on the *dQ/dV* curve are associated with the coexistence of two intercalation phases in GICs. A valley between two peaks represents a single intercalation phase of GICs [300]. A systematic approach was used to segment charge curves into three regions to elucidate the charge storage mechanisms in these graphitic materials and further correlate them with their

structural characteristics. **Figure 4-7**b shows that points A to E' are identified on TG's charge pattern using different valley voltages on the corresponding *dQ*/*dV* curve. The charging process starts from Point A. PF_6^- in the electrolyte migrates to the surface of TG, and the intercalation begins from 4.3 V at Point B. Stage number (SN) is an index used to describe the formed GICs with different stage features, which is referred to the number of graphene sheets between two adjacent intercalated layers. **Figure 4-8** depicts the structures of GICs with different SNs [301]. For instance, GICs with a SN of 1 are related to compounds with each graphene interlayer occupied by intercalants. According to previous *in situ* XRD analysis of graphite cathodes under similar conditions, points C, D, and E respond to different SNs of GICs from 3, 2, to 1, respectively [296, 299, 300]. With the continuous PF_6^- insertion, the SN first drops from 3 at Point C to 2 at Point D. EMC solvent molecules can co-intercalate with PF_6^- into graphite [299]. From Point D to D', the SN remains at 2. At the same time, PF_6^- experiences a realignment in the graphite lattice. EMC molecules co-intercalated with PF_6^- are squeezed out of graphite to create more space for more PF_6^- storage [296, 299, 300]. With more PF_6^- being intercalated, the SN of the TG cathode drops from 2 to 1 until Point E at 5.1 V. Then, the SN maintains at 1 until Point E' at 5.2 V, during which a squeezing process of co-intercalated EMC molecules takes place, similar to that happens between Point D and D'. The charging curves and corresponding *dQ*/*dV* profiles of NG, SG, and EG are shown in **Figure 4-9**. For starting PF_6^- insertion, TG and SG show a lower onset potential of 4.3 V at Point B than 4.4 V of NG and EG, suggesting it is easier to intercalate PF_6^- into TG and SG.

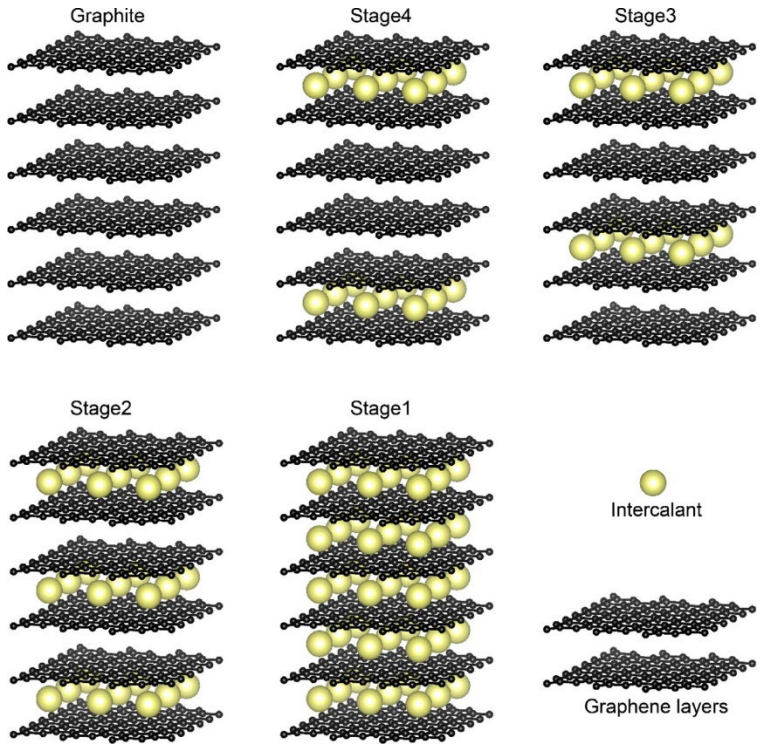

Figure 4-8. Schematic illustrations of graphite intercalation compounds (GICs) with different stage features (stage number SN 4, 3, 2, and 1) [301].

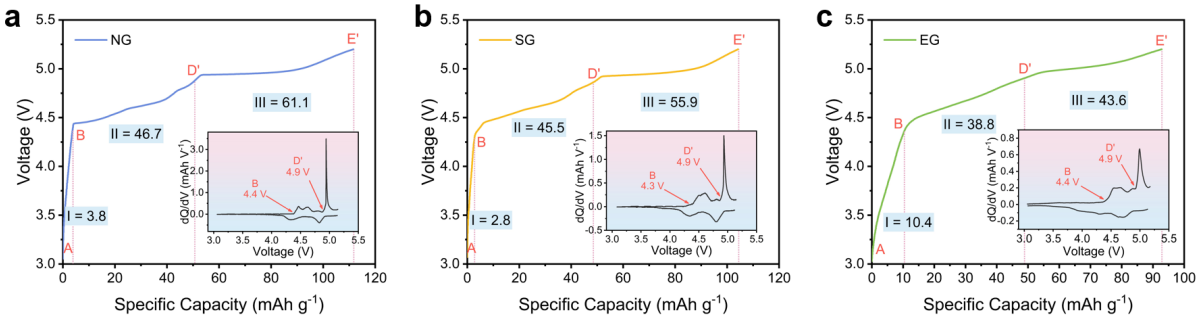

Figure 4-9. Charge curves of graphitic cathodes segmented into three regions and the corresponding *dQ/dV* profiles in the insets: (a) NG, (b) SG, and (c) EG in graphite/Li half-cells.

The voltage profiles were divided into three regions: Region I between Point A and B, related to anion migrating in the electrolyte, adsorption on graphite surfaces, and getting ready to be intercalated; Region II between Point B and D', involving the starting of anion

intercalation until the SN drops to 2; and Region III between Point D' and E', representing the phase transition from SN of 2 to SN of 1 with more anion storage in graphite. The energy storage capacities of each region for the different graphitic materials were calculated and summarised in **Figure 4-7**c. EG shows the highest energy storage capacity of 10 mAh g^{-1} in Region I, about 3 times larger than that of SG at 3 mAh g^{-1}. This can be ascribed to EG's largest surface area and most defective structures, providing more active sites for anion absorption. In contrast, SG, with the smallest surface area and the least defective structure, shows the lowest capacity in Region I. These results indicate that the surface area and defect degree are the two main determining factors that affect the energy storage capacity in Region I [247, 250]. The energy storage capacity in Region I follows the EG > TG > NG > SG sequence, aligning well with the four graphitic materials' SSA and I_D/I_G. In Region II, much more anions are stored in graphite via either intercalation or absorption. The capacity of the four graphitic materials varies from 39 to 47 mAh g^{-1}, with a relatively small difference among them. NG, with a larger L_a of 59.63 nm, delivers a higher capacity of 47 mAh g^{-1} than EG (39 mAh g^{-1}), with the largest SSA of 38 m^2 g^{-1}. This suggests that graphite crystalline length (L_a) is a more critical parameter than SSA in determining the capacity in Region II under the 1 C charging current density. A similar phenomenon was observed in Region III. NG shows the largest capacity of 61 mAh g^{-1}, suggesting that the L_a of graphitic materials may also control the storage capacity in Region III.

Next, the kinetics of anion storage in the graphitic cathodes were analysed using their cyclic voltammetry (CV) curves obtained under the scan rates from 0.1 to 1.0 mV s^{-1} in a voltage range from 3.0 to 5.2 V vs. Li/Li^+. The fifth cycle of CV curves under each scan rate was used to ensure the result consistency, shown in **Figure 4-7**d and **Figure 4-10**a - c. Multiple couples of redox peaks were observed, indicating the reversible intercalation and de-intercalation of PF_6^- into/from graphitic cathodes. The couples of redox peaks in each CV are

related to stage transformations in GICs. The largest anodic peak *a* (**Figure 4-7**d) for TG appears at 5.1 V, representing Stage 1, consistent with the valley potential obtained at Point E observed in the *dQ/dV* curve (**Figure 4-7**b inset). The relationship between redox peak currents (i) and scan rates (v) follows a power law [302, 303]:

$$i = av^b$$

where a and b are adjustable parameters. An electrochemical reaction can be distinguished according to two conditions: b = 1, representing fast surface redox reactions, and b = 0.5, suggesting diffusion-controlled redox reactions [272, 303]. The logarithmic forms of the last anodic peak a current (ia) and the first cathodic peak b current (ib) (see **Figure 4-7**d) were plotted against the logarithmic form of the scan rate (v). The plots are displayed in **Figure 4-7**e and **Figure 4-10**d - f. The b values were calculated for ia and ib of different graphitic materials to compare their kinetics between Stages 1 and 2 during anion intercalation. The values are shown in **Figure 4-7**f. TG exhibits the highest b values of 0.90 for ia and 1.00 for ib, suggesting that its anion storage capacity originates from surface redox reactions. In comparison, SG has the lowest b value of 0.75 for ia, NG is at 0.83, and EG is at 0.84, suggesting increasing contributions from diffusion-controlled redox reactions. Larger b values for ib were obtained for all graphitic materials than those of ia, suggesting that anion de-intercalation has faster kinetics than anion intercalation. TG and EG display relatively large b values for ia and ib, indicating significant contributions from surface redox reactions to their anion storage capacity. Based on these analyses, it is speculated that TG and EG cathodes should have excellent rate performances under a high current density.

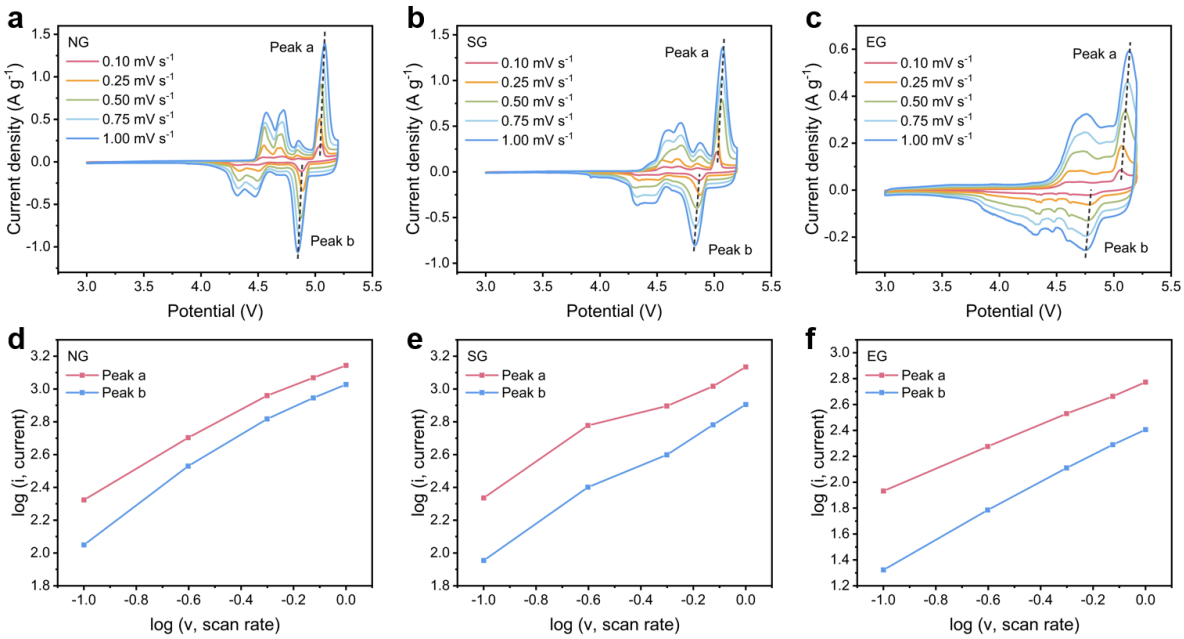

Figure 4-10. CV profiles of graphite/Li half-cells at the scan rates from 0.1–1.0 mV s^{-1}: (a) NG, (b) SG, and (c) EG. The corresponding log *i* versus log *v* profiles to determine *b* values for (d) NG, (e) SG, and (f) EG cathodes, respectively.

All graphite/Li half cells were pre-cycled for 60 cycles under 1 C to achieve a stable condition before rate performance tests, as shown in **Figure 4-11**. A gradual discharge capacity increase was observed in the first 60 cycles for NG and SG cathodes, which can be attributed to a graphite activation process in which the activation energy barrier is overcome, and graphite layers are opened up after repetitive intercalation/de-intercalation of PF_6^- [274, 275, 283, 304]. This phenomenon is inconspicuous on TG and EG cathodes, probably due to their aforementioned dominating fast surface-controlled kinetics, which enables anions to react near the graphite surface instead of tolerating energy penalty to expand graphite layers.

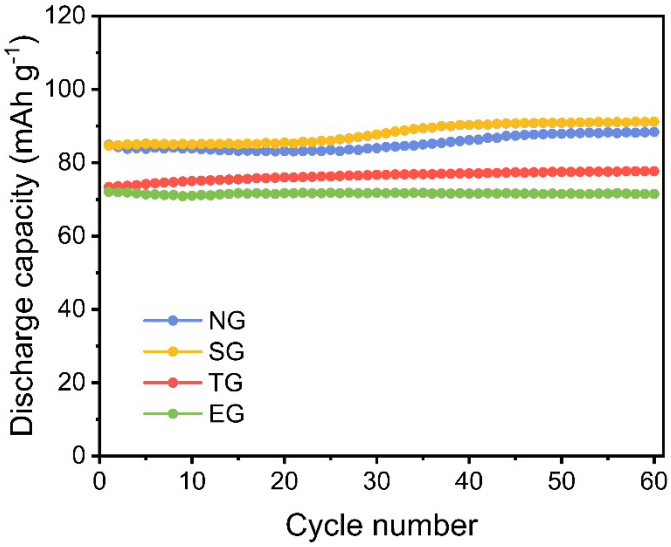

Figure 4-11. Pre-cycling of graphite/Li half cells for 60 cycles under 1 C before rate performance tests to ensure that all cells have reached a stable condition and eliminate the effect of graphite activation on measured cell capacities.

This conjecture is further supported by electrochemical impedance spectroscopy (EIS) analysis results of fresh graphite/Li half cells. **Figure 4-12**a shows the EIS Nyquist plots of the freshly assembled half cells. All fresh cells display impedance curves with features of a semicircle in the high-frequency region and a sloping line in the low-frequency region. As shown in **Figure 4-12**a inset, an equivalent circuit was used for quantitative analysis, where R_e represents the ohmic resistance, R_{ct} represents the charge transfer resistance, CPE is a constant phase element, and W is the Warburg impedance [266, 272, 305]. As shown in **Table 4-4**, EG and TG fresh half cells have lower R_{ct} of 327.7 and 374.5 Ω than NG and SG cells with larger R_{ct} of 417.1 and 427.9 Ω, respectively. Since R_e is mainly related to the resistance of the electrolyte, cell components, and their contact resistance, all fresh cells show similar values around 2 to 4 Ω. The fitting results of EIS spectra signify that TG and EG fresh half cells have lower charge transfer resistance, confirming the previous speculation that the anion storage could happen faster and easier for TG and EG cathodes.

Table 4-4. Parameters of EIS spectra for fresh Li/graphite half cells fitted by the equivalent circuit.

Graphitic materials	R_e (Ω)	R_{ct} (Ω)
NG	3.16	417.1
SG	2.26	427.9
TG	3.89	374.5
EG	4.18	327.7

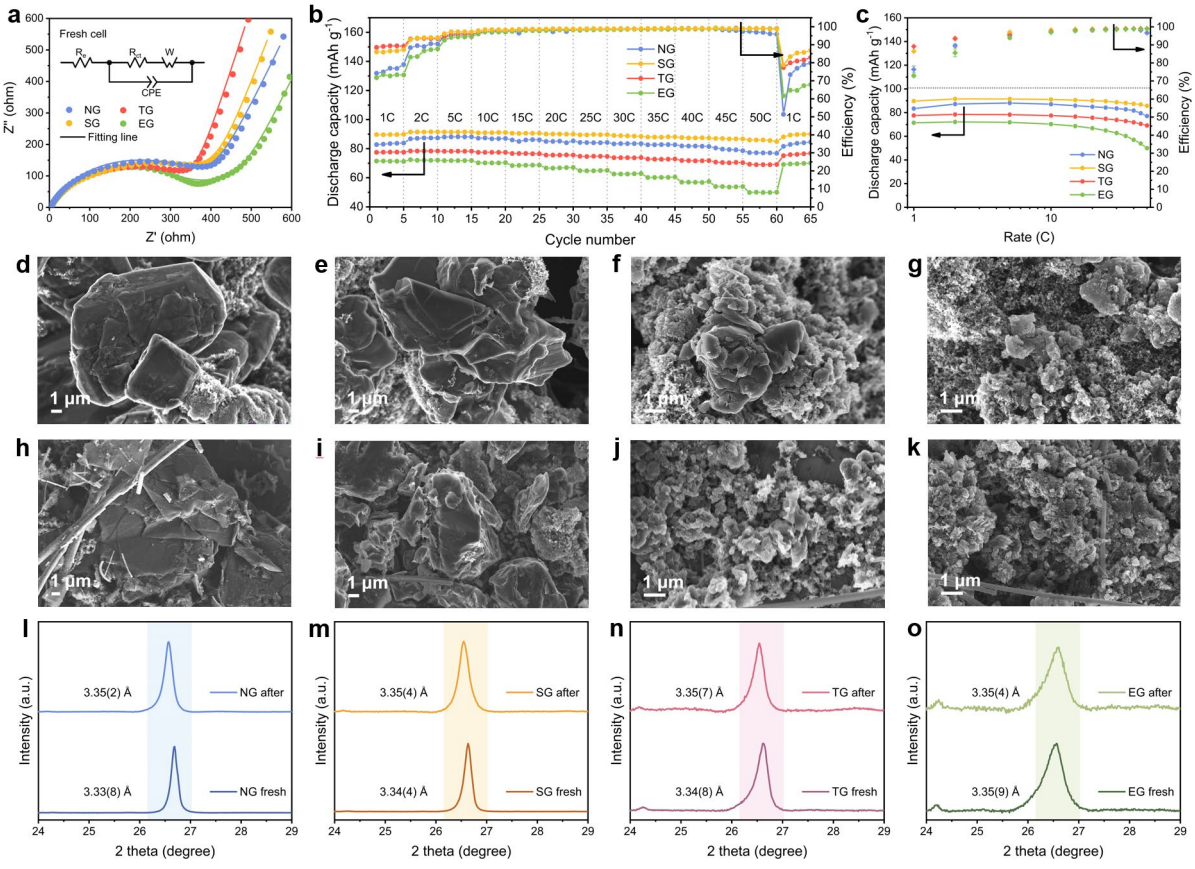

Figure 4-12. (a) Nyquist plots of EIS spectra of fresh graphite/Li half cells. The inset displays the equivalent circuit for fitting data. (b) The rate performance of graphite/Li half cells. (c) Comparison of the rate performance from 1–50 C. SEM images and XRD patterns of graphitic

cathodes before and after the rate performance tests: (d, h, l) NG, (e, i, m) SG, (f, j, n) TG, and (g, k, o) EG, respectively.

The rate performance of graphite/Li half cells was examined from 1 to 50 C in the voltage window of 3.0–5.2 V. **Figure 4-12**b shows that TG has a capacity of 78.4 mAh g^{-1} under 2 C and 5 C and a capacity of 69.2 mAh g^{-1} under 50 C (5000 mA g^{-1}) with 88.3 % capacity retention from 2 C to 50 C. NG shows some capacity fading after 40 C. Its capacity drops to 76.8 mAh g^{-1} at 50 C, around 87.1 % capacity retention. SG shows the highest capacity retention of 92.7 % from 2 C to 50 C. In comparison, EG experiences more significant capacity fading from 15 C, though its capacity is 72.4 mAh g^{-1} when the current density is returned from 50 C to 1 C, comparable to that of TG at 2 C. The average capacity measured in five cycles at various C rates is summarised in **Figure 4-12**c.

When the current density is returned from 50 C to 1 C, TG and EG deliver 76.8 and 70.1 mAh g^{-1}, achieving a capacity recovery of 98.0 and 96.8 %, respectively. Their capacity recovery ratio is higher than that of NG at 95.9 %. GCD profiles under the initial 1 C and the 1 C after rate performance tests at 50 C are shown in **Figure 4-13**. These two GCD profiles of TG, SG, and EG almost overlap, indicating their excellent reversibility after high rate charge/discharge. In contrast, NG shows a considerably increased charge capacity of 158.8 mAh g^{-1} with a low efficiency of 51.4%. The low efficiency of NG suggests severe side reactions, probably induced by irreversible graphite exfoliation during the charge/discharge under high current density.

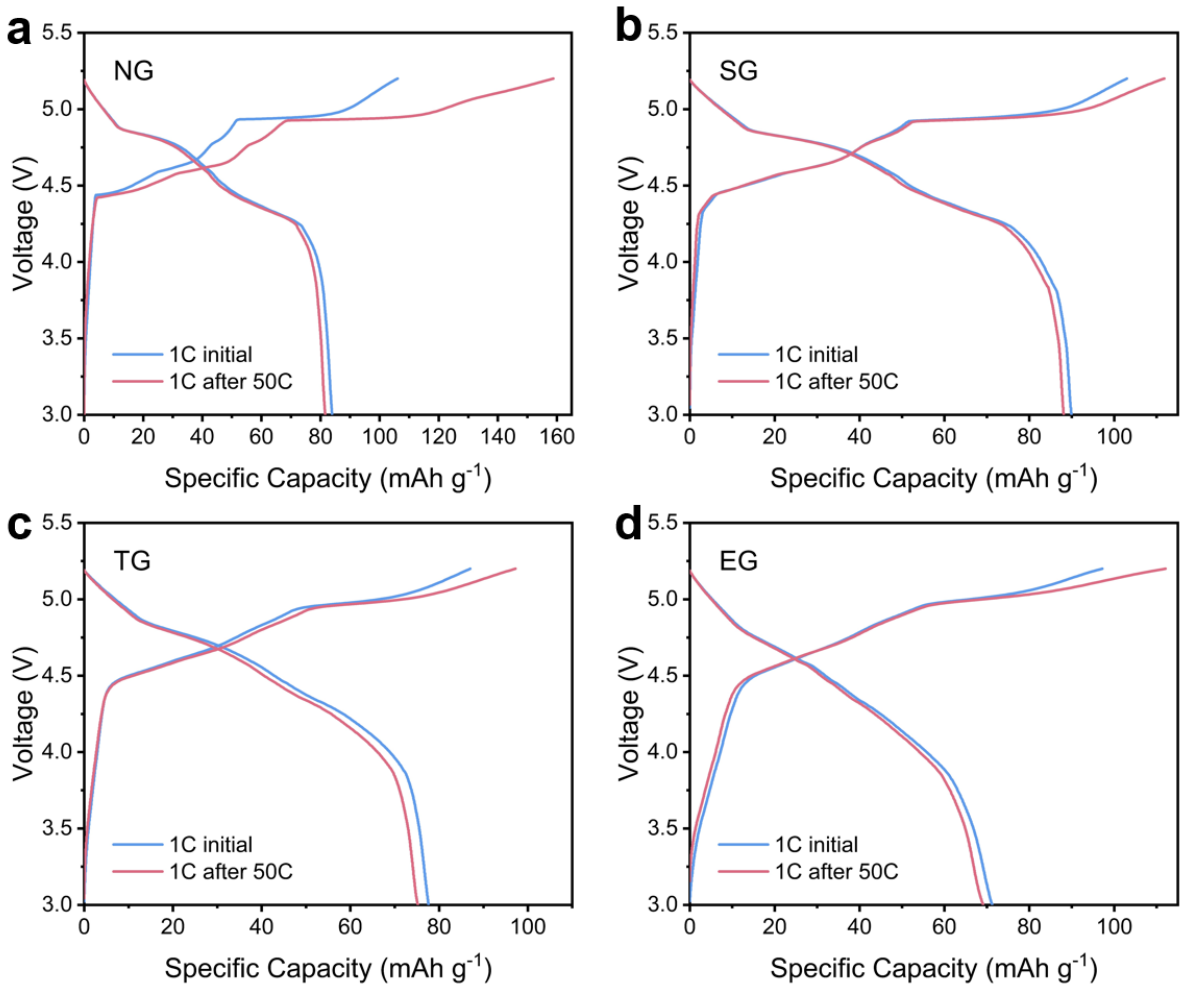

Figure 4-13. GCD curves from rate capability tests under the initial 1 C rate (5th cycle) and under 1 C rate after 50 C rate tests (61st cycle) for different graphite cathodes: (a) NG, (b) SG, (c) TG, and (d) EG.

To elucidate the reason for the lower efficiency after rate performance tests, all graphite cathodes were characterized by SEM. **Figure 4-12**d - k show SEM images of fresh and cycled graphitic cathodes. All fresh cathodes show similar morphology as pristine materials (**Figure 4-1**e - h), whereas dispersed nanoparticles are conductive additives (*i.e.*, carbon black, Super P). After cycling under the high rates, SG, TG, and EG show minor structural changes except for a slight decrease in particle sizes. In contrast, the cycled NG cathode displays an apparent

structural collapse with broken graphite debris and sharpened graphite edges. These structural changes would create more defects, resulting in more active sites for electrolyte decomposition and the formation of cathode electrolyte interfaces. This may explain NG's lower efficiency after the high-rate test. The excellent rate performance of TG can be attributed to its fast anion intercalation/de-intercalation, as indicated in its CV analysis (**Figure 4-7**d - f). TG also exhibits a quick recovery after the high-rate test, which can be attributed to its structural stability with a good tolerance for rapid and repetitive anion intercalation/de-intercalation.

The structural variation of graphitic cathodes before and after the rate tests was also characterized by XRD. **Figure 4-12**l - o show that NG, SG, and TG have slightly increased d_{002} after the high-rate tests, indicating interlayer expansion due to fast and repeated anion intercalation/de-intercalation. Fresh NG has the smallest d_{002} of 0.333(8) nm, and the cycled NG has the most significant interlayer expansion ratio of 0.44 %, indicating that NG suffers from structure deterioration, consistent with its SEM images (**Figure 4-12**d and h). This result suggests that NG with a small d_{002} is unsuitable for high-rate applications. In comparison, fresh TG has a larger d_{002} of 0.334(8) nm and experiences a lower interlayer expansion ratio of 0.25 %. The better structural stability of TG can be correlated to its smaller L_a and L_c, which offer better tolerance to interlayer expansion. The d_{002} of EG decreases slightly after the high-rate test. The anion intercalation/de-intercalation in EG may mainly occur near its surface or in a shallow region near its surface [266, 306]; thus, the interlayer expansion induced by anion intercalation is negligible on the measured average d_{002} of bulk EG.

Overall, TG performs better than NG under high current densities, as indicated by TG's higher capacity retention ratio of 88.3 % at 50 C and a higher capacity recovery of 98.0 % at 1 C after the rate test at 50 C. TG's excellent performance is associated with its fast anion storage kinetics, lower charge transfer resistance at the initial state, and good structural stability

resulting from its optimal crystalline size, which helps avoid the structural collapse resulting from fast and repetitive anion intercalation and de-intercalation.

4.3.3 Electrochemical performances of graphitic anodes

Next, graphite/Li anode half cells were assembled with the different graphitic materials acting as anodes, and their performance under different charge/discharge current densities was measured. **Figure 4-14**a displays their performance under the charge/discharge rates from 0.1 C to 10 C in the voltage window of 0.001–3 V. 10 C was selected as the upper cutoff for anodes because the corresponding current density would approach 50 C in cathodes (*i.e.*, 1 C = 372 mA g^{-1} for graphite anode, and 1 C = 100 mA g^{-1} for graphite cathode). **Figure 4-14**b shows the summary of the rate performance of graphitic anode half cells.

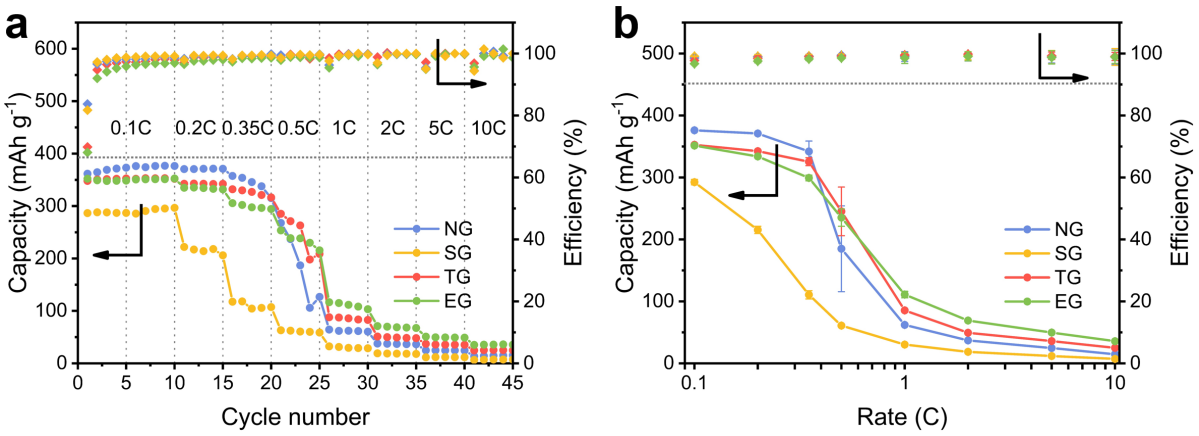

Figure 4-14. (a) Rate performance of graphite/Li half cells with different graphitic anodes. (b) Comparison of the rate performance of graphitic anodes from 0.1–10 C.

Their corresponding GCD profiles under different current densities are shown in **Figure 4-15** and **Figure 4-16**. TG and EG half cells deliver higher specific capacities at larger current

rates over 0.35 C till the end of the test. At lower rates from 0.1–0.35 C, TG and EG half cells have similar capacities comparable to NG half cells. In sharp contrast, SG half cells show a severe capacity fading starting from 0.2 C and maintain a much lower capacity through the rate test, indicating its inferior rate performance. From **Figure 4-16**, SG half cells show larger polarization induced by high current densities than the other three types of half cells. A larger voltage jump at the beginning of the charging process was observed for SG half cells under all C rates, which is related to the ohmic potential drop (IR drop), indicating SG half cells have larger resistance. During discharging, the high-voltage sloping region capacity is associated with the adsorption of Li^+ in defects or edge sites, whereas the low-voltage plateau capacity is assigned to Li^+ intercalation into the graphitic layers [288, 307, 308]. SG exhibits limited capacities in both sloping and low-voltage regions, revealing the sluggish Li^+ intercalation into its graphite interlamination. Previous studies have extensively investigated the poor kinetics of graphite anode [86, 307-309]. The inferior rate capability of SG can be ascribed to its smallest SSA and pore volume, relatively large crystal size, and less defective structure among the four graphitic materials, leading to limited active sites for Li^+ insertion, poor accommodation for electrolyte, and relatively long ion transport distance. The other half cells all suffered from capacity decay from around 0.5–1 C, showing similar trends as other graphitic anodes reported in the literature [94, 310, 311].

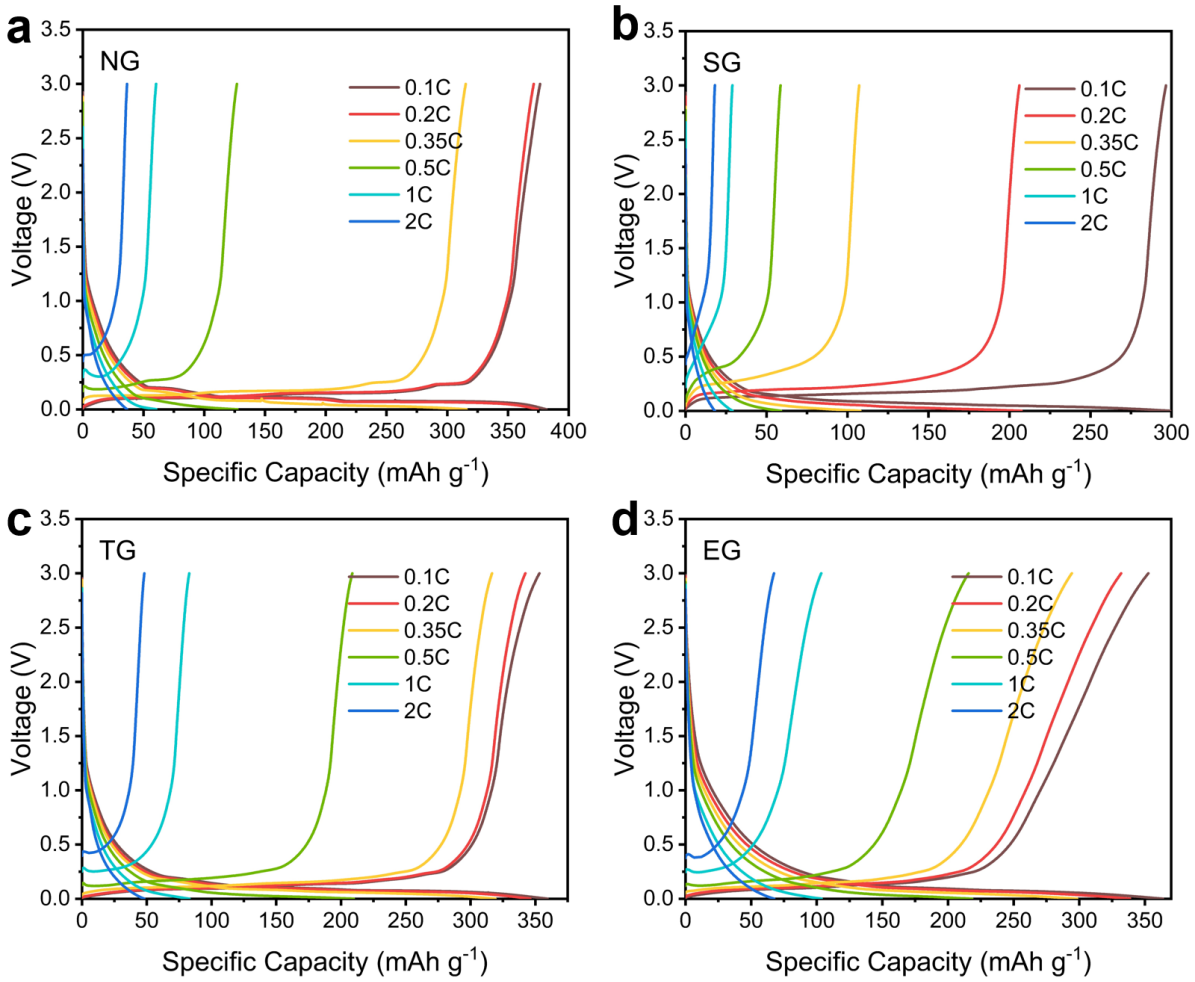

Figure 4-15. GCD curves from rate capability tests under different current rates of 0.1 C (10th cycle), 0.2 C (15th), 0.35 C (20th), 0.5 C (25th), 1 C (30th), and 2 C (35th) for different graphite anodes: (a) NG, (b) SG, (c) TG, and (d) EG.

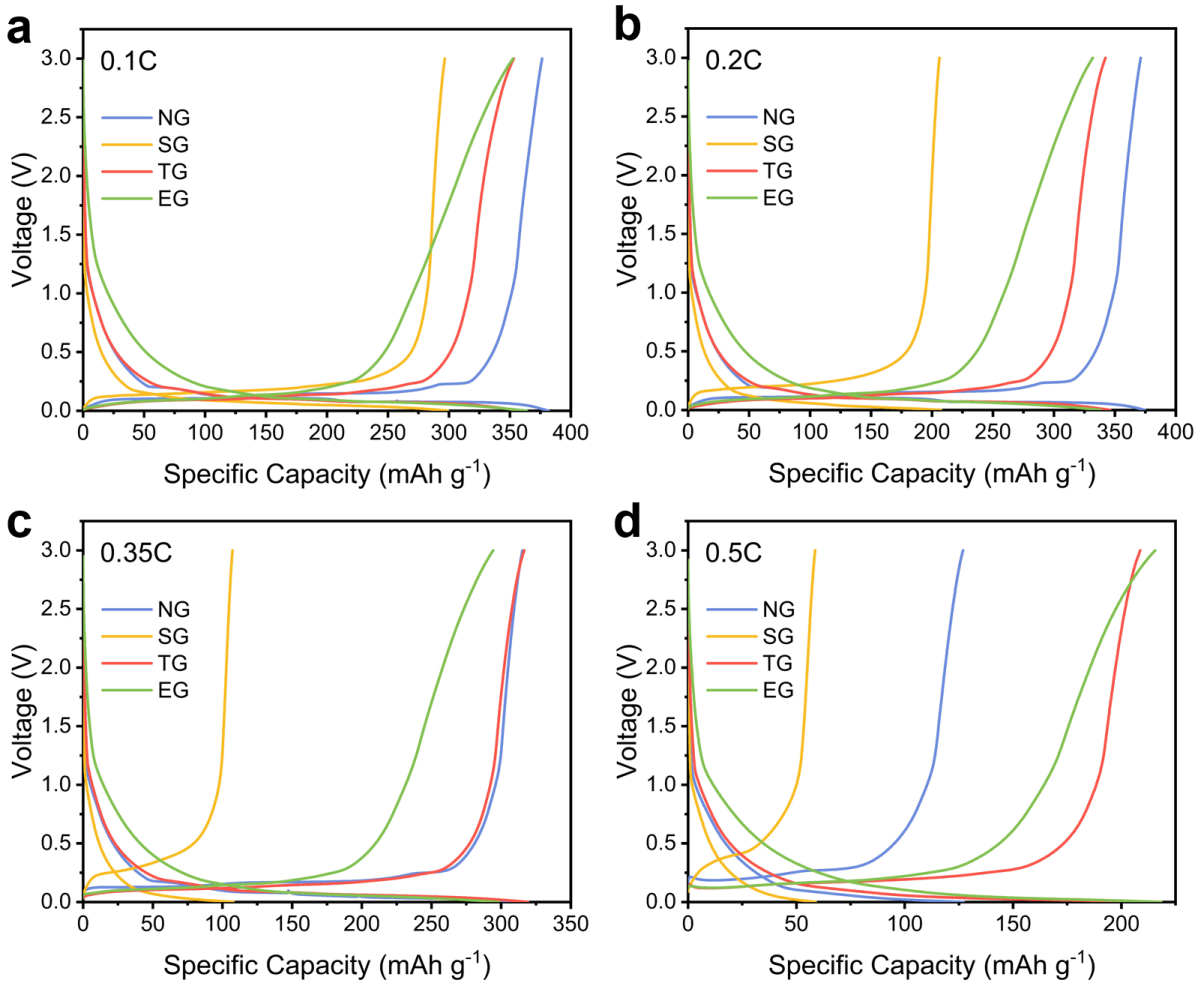

Figure 4-16. GCD curves of graphite/Li half cells with NG, SG, TG, and EG anodes from rate capability tests under different current rates: (a) 0.1 C, (b) 0.2 C, (c) 0.35 C, and (d) 0.5 C. (The data presented here is the same as shown in Figure S9 but in a different display version for the sake of horizontal comparison between the four graphitic anodes under a specific C rate.)

4.3.4 Electrochemical performances of DCB full cells

Finally, DCBs were assembled using the cell configuration shown in **Figure 4-1**a, using the same graphite materials in both cathodes and anodes. **Figure 4-17**a and b show the rate capabilities of assembled DCB full cells under different current rates from 1–50 C within the voltage range of 3.0–5.2 V. NG and SG full cells have a capacity of 83.7 and 91.8 mAh g^{-1} at

1 C with apparent capacity fading from 10 C. At the end of the tests, the capacities of NG and SG full cells drop to 59.6 and 65.6 mAh g^{-1}, representing the capacity retention ratio of 71.2 and 71.5 %, respectively. EG and TG full cells delivered their largest capacities of 74.7 and 75.1 mAh g^{-1} under 5 C, respectively. They have capacities of 66 and 53.4 mAh g^{-1} at the last cycle under 50 C, comparable to or even higher than those of NG and SG full cells under the same condition. They show significantly higher capacity retention ratios of 93.4 and 79.2 %, respectively, indicating their better rate performance with less capacity decay.

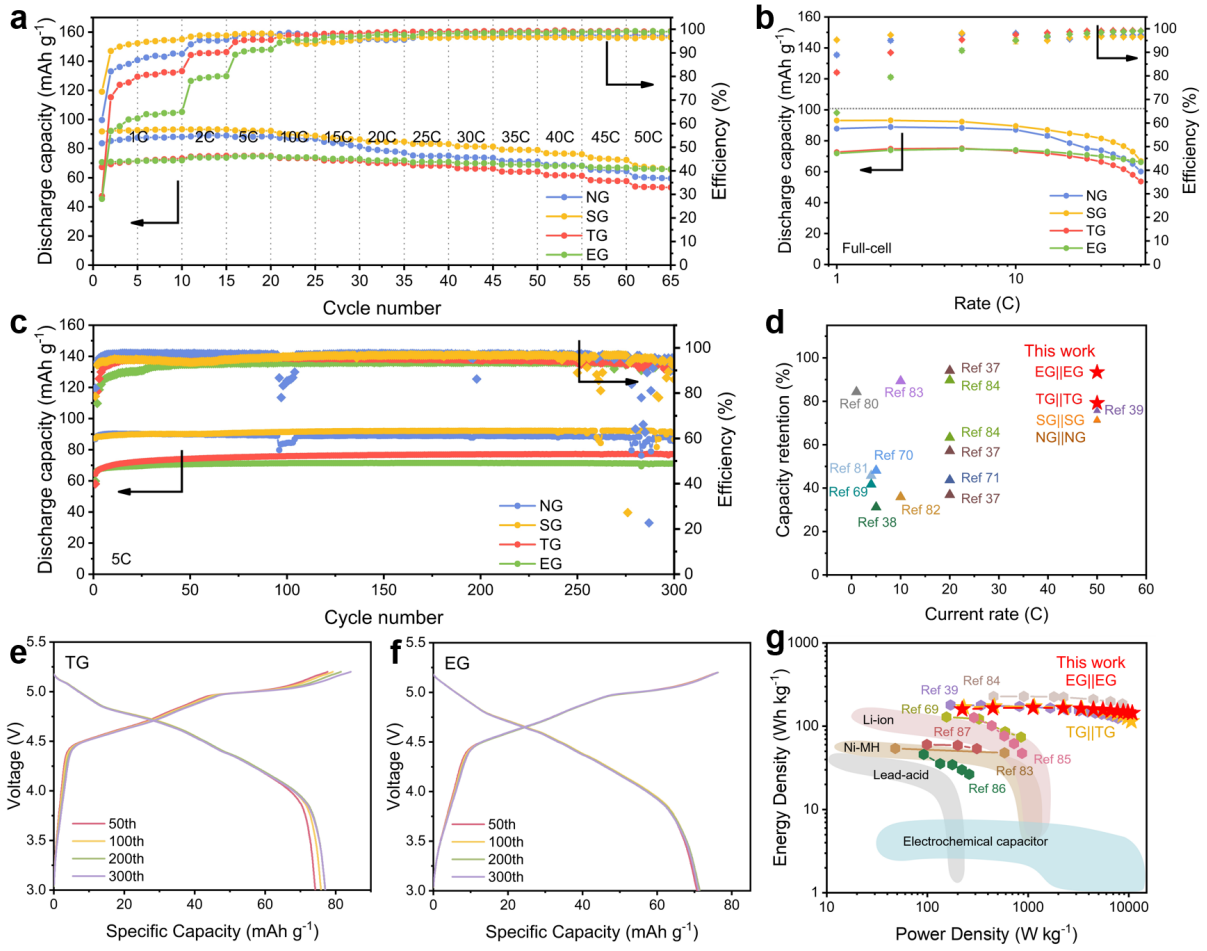

Figure 4-17. The electrochemical performance of DCB full cells assembled using different graphitic materials in cathodes and anodes. (a) The rate performance of DCB full cells. (b) Comparison of the rate performance of DCB full cells from 1 C to 50 C. (c) Cycling

performance of DCB full cells under 5 C rate. (d) Comparison of the rate performance of DCB full cells in this study with those in recently published studies. GCD curves of (e) TG and (f) EG full cells at selected cycles from cycling tests under 5 C rate. (g) Ragone plot of TG and EG DCB full cells in this study in comparison with conventional electrochemical energy storage devices and recently reported DCBs. The energy density and power density were calculated based on the total weight of active materials in both the anode and cathode.

A relatively high current rate of 5 C (500 mA g^{-1}) was selected to analyse the cycling performance of DCBs. **Figure 4-17**c shows that TG and EG full cells display highly stable cycling without capacity fading over 300 cycles. In contrast, NG and SG full cells have relatively unstable cycling, with fluctuating capacities occurring at only the 100^{th} cycle for the NG full cell and around the 250^{th} for the SG full cell. TG and EG full cells deliver discharge capacities of 77.1 and 71.1 mAh g^{-1} at the 300^{th} cycle, comparable to that of the NG full cell at 85.4 mAh g^{-1} and the SG full cell at 86.6 mAh g^{-1}. Slightly increased capacities were observed on all full cells during the initial 20 cycles, which can be originated from the gradual wetting and activation process of the electrodes after repetitive intercalation and de-intercalation [274, 283]. Large energy penalty is taken when opening up the graphite layers for intercalation, and insufficient penetration of electrodes by the electrolyte would limit the capacities during the initial cycles [304]. GCD profiles of the full cells at the 50^{th}, 100^{th}, 200^{th}, and 300^{th} cycles are shown in **Figure 4-17**e and f and **Figure 4-18**. TG and EG full cells display well-maintained charge and discharge curves during the 300 cycles and obtained high capacity retention ratios of 120 and 109 %, further confirming their excellent cycling stabilities. **Figure 4-17**d shows that their capacity retention ratio under high current density is also superior to that of most DCBs reported in recent studies. The details are summarised in **Table 4-5** [270-272, 280, 283, 284, 287, 304, 305, 312, 313]. **Figure 4-17**g shows a Ragone plot of DCB full cells in this

study compared to conventional electrochemical energy storage devices and recently reported DCBs [272, 280, 281, 283, 284, 286, 314-316]. The energy density and power density are estimated based on the total weight of active electrode materials in both anodes and cathodes (**Table 4-6**, **Table 4-7** and **Table 4-8**). The TG full cell has high energy densities of 168.7 and 114.9 Wh kg^{-1} at power densities of 0.23 and 10.6 kW kg^{-1}, respectively. The EG full cell shows high energy densities of 159.7 and 144.3 Wh kg^{-1} at power densities of 0.22 and 10.8 kW kg^{-1}, respectively. The superior energy densities and power densities of the TG and EG full cells outperform most conventional energy storage devices and recently reported DCBs.

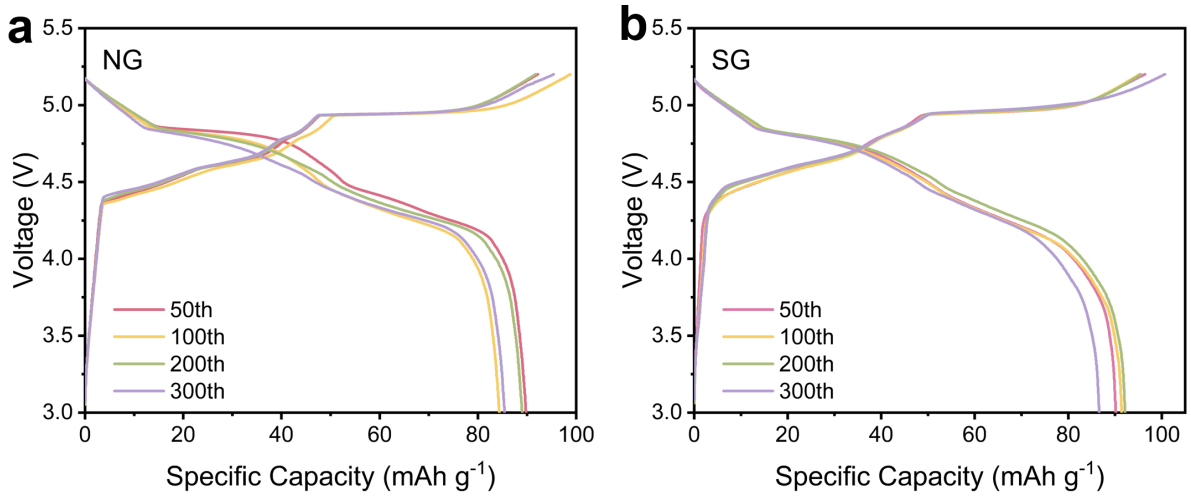

Figure 4-18. GCD curves of (a) NG and (b) EG full cells at selected cycles from cycling tests under 5 C rate.

Table 4-5. Performance comparison of DCBs developed in this work with other recently reported DCBs.

Electrode (Cathode/ Anode)	Electrolyte	Cycling rate	Cycles	Final capacity, mAh g^{-1}	Capacity retention, %	Rate used in rate capability tests	Capacity at highest rate, mAh g^{-1}	Capacity retention, %
TG|TG (this work)	1 M LiPF6 in EMC	5 C	300	77.1	120 %; 99.7 %	1-50 C	53.4	79.2 %

					(compare with max capacity)			
EG|EG (this work)	1 M LiPF6 in EMC	5 C	300	71.1	109 %; 99.4 % (compare with max capacity)	1-50 C	66	93.4 %
NG|NG (this work)	1 M LiPF6 in EMC	5 C	300	85.4	98.4 %; 94.5 % (compare with max capacity)	1-50 C	59.6	71.2 %
SG|SG (this work)	1 M LiPF6 in EMC	5 C	300	86.6	99.1 %; 93.9 % (compare with max capacity)	1-50 C	65.6	71.5 %
Graphite| graphite [312]	$AlCl_3$ and [EMIm]Cl (1.3:1 M)	0.2 C	600	70	79.5 %	0.2-1 C	70	84.3 %
Composite graphite (CG)|CG [313]	$PP_{14}TFSI$	3 C	600	47	100 %	0.5-4 C	32	45.7 %
KS6L graphite| SMG A4 graphite [271]	3.5 M $LiPF_6$ in EMC	0.5 C	30	93	100 %	0.5-5 C	29	31.2 %
Natural graphite| natural graphite [304]	$Pyr_{14}TFSI$	3 C	100	27	60 %	0.5-5 C	25	48.1 %
Graphite| graphite [283]	5.2 M KFSI in TMS	1 C	300	83.4	100 %	1-4 C	34.8	41.7 %
Graphite| graphite [287]	4 M $LiPF_6$ in EMC with 3% FEC	5 C	1000	60	75 %	0.5-10 C	56	35.9 %
Mesocarbon microbead (MCMB)| MCMB [280]	1 M $LiPF_6$ in EMC/SL (1:4 vol)	5 C	3000	-	88.5 %	0.5-10 C	-	89.3 %
Graphite| graphite [270]	0.5 M $LiPF_6$ in EMC/SL (1:4 vol)	5 C	400	52.9	79.2 %	1-20 C	34.4	36.9 %
Graphite| graphite [270]	1 M $LiPF_6$ in EMC/SL (1:4 vol)	5 C	850	67.8	82.1 %	1-20 C	54.4	57.1 %
Graphite| graphite [270]	2 M $LiPF_6$ in EMC/SL (1:4 vol)	5 C	1000	83.7	94.7 %	1-20 C	91	94.1 %
Reduced graphene	1 M $LiPF_6$ + 0.02 M	10 C	400	280	46.7 %	1-20 C	190	43.7 %

oxide (rGO)| MCMB [305]	LiDFOB in FEC/FDEC/HFE (2:2:6 vol)							
MTI graphite| RGS graphite [272]	3 M $LiPF_6$ in EMC with 0.5 wt% LiDFOB	10 C	6500	89	92.4 %	1-50 C	78	75.7 %
Graphite| graphite (switched) [284]	2 M $LiPF_6$ in EMC with 3 wt% VC	5 C	500	85	96 %	2-20 C	82	89.7 %
Graphite| graphite (unswitched) [284]	2 M $LiPF_6$ in EMC with 3 wt% VC	-	-	-	-	2-20 C	53.4	63.3 %
MCMB graphite| CGP graphite [268]	1.7 M $LiPF_6$ in FEC/EMC (4:6 w/w) + 5 mM HFIP	C/7	50	38	60.3 %	-	-	-
KS6L graphite| graphite [317]	$Pyr_{14}TFSI$ with LiTFSI	5 C	500	50	99.8 %	-	-	-
Spent graphite annealed at 650 ºC (SG-650)|SG-800 [285]	1 M $LiPF_6$ in EC/DMC (1:1 vol)	0.5 C	50	36	61 %	-	-	-

Table 4-6. Energy density and power density of TG full cells in this study.

I_c (mA g^{-1})	V_m (V)	$C_{cathode}$ (mAh g^{-1})	C_{full} (mAh g^{-1})	E_{full} (Wh kg^{-1})	P_{full} (kW kg^{-1})
100	4.60	73.3	36.7	168.7	0.23
200	4.61	75.1	37.6	173.0	0.46
500	4.59	75.1	37.6	172.5	1.15
1000	4.56	73.5	36.8	167.8	2.29

1500	4.53	71.9	36.0	163.0	3.41
2000	4.50	70.3	35.2	158.3	4.49
2500	4.47	68.5	34.3	153.1	5.57
3000	4.44	66.6	33.3	147.8	6.65
3500	4.40	64.3	32.2	141.6	7.72
4000	4.37	61.9	31.0	135.2	8.69
4500	4.32	58.4	29.2	126.1	9.66
5000	4.26	54	27.0	114.9	10.61

Table 4-7. Energy density and power density of EG full cells in this study.

I_c (mA g^{-1})	V_m (V)	$C_{cathode}$ (mAh g^{-1})	C_{full} (mAh g^{-1})	E_{full} (Wh kg^{-1})	P_{full} (kW kg^{-1})
100	4.43	72.0	36.0	159.7	0.22
200	4.46	74.0	37.0	165.0	0.45
500	4.47	74.7	37.4	167.0	1.12
1000	4.46	74.1	37.1	165.3	2.23
1500	4.45	73.1	36.6	162.6	3.34
2000	4.43	71.9	36.0	159.4	4.45
2500	4.42	71.0	35.5	156.9	5.54
3000	4.41	70.0	35.0	154.3	6.61
3500	4.39	69.0	34.5	151.6	7.69
4000	4.38	68.2	34.1	149.3	8.81

4500	4.37	67.3	33.7	147.0	9.80
5000	4.35	66.3	33.2	144.3	10.82

Table 4-8. Energy density and power density of TG and EG full cells based on the entire mass of anodes and cathodes.

I_c (mA g^{-1})	TG full cell		EG full cell	
	E'_{full} (Wh kg^{-1})	P'_{full} (kW kg^{-1})	E'_{full} (Wh kg^{-1})	P'_{full} (kW kg^{-1})
100	135.0	0.18	127.7	0.18
200	138.4	0.37	132.0	0.36
500	138.0	0.92	133.6	0.89
1000	134.2	1.83	132.2	1.78
1500	130.4	2.73	130.1	2.68
2000	126.6	3.59	127.5	3.56
2500	122.5	4.45	125.5	4.43
3000	118.3	5.32	123.4	5.29
3500	113.3	6.18	121.3	6.15
4000	108.1	6.95	119.5	7.05
4500	100.9	7.73	117.6	7.84
5000	91.9	8.48	115.4	8.66

4.4 Conclusion

Graphitic materials synthesized by catalytic methane pyrolysis as a co-product of H_2 production can be purified by high-temperature (2800 °C) thermal treatment or low-temperature electrochemical purification methods, reaching the purity of 99.32 (TG) and 97.59 wt.% (EG), respectively. GCD, *dQ/dV*, and CV analysis of their charge storage mechanism as cathodes in DCB half cells indicate that TG and EG enable faster charge storage kinetics than commercial NG and SG, involving surface redox reactions. TG cathode shows a capacity of 78.4 mAh g^{-1} under 2 C and retains 98.0 % at 76.8 mAh g^{-1} at 1 C after the rate capability test to 50 C. SEM and XRD show that commercial NG and SG have severe structural collapses under high current rates. In contrast, TG demonstrates excellent structural stability under fast and repeated anion de-/intercalation with a low interlayer expansion rate of 0.25 %. Further, as anodes in DCB half cells, TG and EG also show excellent rate performances with higher specific capacities at 0.35–10 C. DCB full cells assembled using EG and TG display large capacities of 74.7 and 75.1 mAh g^{-1} at 5 C rate and higher capacity retentions. In addition, TG and EG demonstrate highly stable cycling processes without capacity decay at a high current rate of 5 C over 300 cycles. TG and EG full cells also exhibit superior energy densities of 168.7 and 159.7 Wh kg^{-1} and power densities of 10.6 and 10.8 kW kg^{-1} (based on the total weight of active electrode materials in both anodes and cathodes), outperforming most conventional energy storage devices and recently reported DCBs. Overall, the purified graphitic co-product of H_2 production can serve as both cathode and anode materials in DCBs with excellent rate performance and cycling stability. This opens their new application in energy storage, benefiting the broader adoption of the emission-free H_2 production process via methane pyrolysis.

Chapter 5. Conclusions and outlooks

5.1 Conclusions

Catalytic methane pyrolysis is a promising approach to achieve environmentally friendly hydrogen production, which directly splits methane into hydrogen and solid carbon materials with no direct carbon dioxide emissions. With a mass ratio of hydrogen to solid carbons of 1 to 3, large amounts of carbon materials are generated from the catalytic methane pyrolysis process. Developing suitable applications for these solid carbon co-products can turn them into value-added commodities, avoid waste generation, and bring economic benefits to offset hydrogen production costs. Carbon materials play a crucial role in electrochemical energy storage devices, serving as essential components of electrodes, including conductive additives and active materials. With the ever-growing energy demand, the continuous development of the energy storage field holds great potential for the accommodation of these carbon co-products from clean hydrogen production via the catalytic pyrolysis process.

First, a comprehensive study is carried out on the widely used techniques for the characterization of carbon materials and the determination of their physiochemical properties and electrochemical performances. Microscopic and diffraction techniques, including SEM, TEM and XRD, could be employed to detect carbon materials' morphology and crystal structure. Nitrogen physisorption technique can determine carbon materials' surface area and pore structure. Spectroscopic techniques, including Raman and XPS can be applied to obtain the chemical structure, defect level and surface functional groups of carbon materials. Thermal techniques such as TGA could examine carbon materials' purity and thermal stability. Electrochemical characterization techniques including CV, EIS and GCD measurements could be used to evaluate their electrochemical performances. All these technologies are used in

further works to investigate and understand the characteristics of solid carbon materials co-produced from the catalytic methane pyrolysis process.

Second, graphitic carbon materials are synthesized as a co-product from the catalytic methane pyrolysis process using Fe ore catalysts. They are purified by the standard high-temperature thermal treatment at 2800 ^{o}C and the alternative electrochemical method to reach high purity of 99.82 and 99.59 wt.%, respectively. Being evaluated as conductive carbon additives for zinc-carbon batteries, the purified carbon materials show a high electrical conductivity of up to 98 S cm^{-1} when incorporated in MnO_2 cathodes and a good electrolyte (1M $ZnSO_4$) absorption capability of up to 4.2 mg mg^{-1}, which are two essential properties for carbon conductive additives. Zinc-carbon batteries assembled using these carbon materials exhibit a specific capacity of 114 (thermal) and 109 (electrochemical) mAh g^{-1} under 0.05 A g^{-1}. They demonstrate higher electrode conductivity, better rate performance, lower internal resistance, and superior long-term stability compared with cells using commercial carbon conductive additives (Super P). Thus, the high-purity graphitic carbon materials from the catalytic methane pyrolysis process can serve as efficient carbon conductive additives for batteries. This opens a new path to generate a value-added commodity as a co-product from eco-friendly hydrogen production.

Third, dual-carbon batteries utilizing carbon materials as active materials for both anode and cathode electrodes are promising battery systems due to the unique advantages of low cost, high sustainability, and high working voltage. Their current challenges of unsatisfied cyclability and poor rate performance resulted from graphite cathodes suffering from severe structural deterioration, calling for advanced carbon electrode materials. The graphitic carbon co-products from methane pyrolysis are demonstrated as both cathodes and anodes to enable high-rate-performance dual-carbon batteries, outperforming commercial natural and synthetic graphite. The carbon purity can reach 99.32 and 97.59 wt.%, respectively, using a standard

high-temperature thermal treatment or a room-temperature electrochemical method. Compared to graphite, they have smaller crystalline sizes and larger surface areas, enabling faster surface redox reactions and better structural stability upon electrolyte ion intercalation. Dual-carbon full cells with 1M $LiPF_6$ in ethyl methyl carbonate electrolyte deliver energy storage capacities of 75.1 and 74.7 mAh g^{-1} at 500 mA g^{-1} with capacity retentions of 79.2 and 93.4 % after the high-rate charge/discharge over 5000 mA g^{-1}, respectively. They can also be cycled at 500 mA g^{-1} over 300 cycles without capacity decay, demonstrating excellent cycling stability. They show energy densities of 168.7 and 159.7 Wh kg^{-1} at power densities of 10.6 and 10.8 kW kg^{-1}, outperforming recently reported dual-carbon batteries. These findings open a new application of graphitic carbon co-products from methane pyrolysis, benefiting the broader adoption of the emission-free hydrogen production process.

5.2 Outlooks

Further studies could explore three aspects.

Optimising the high-purity synthesis of graphitic carbon: Here, the original graphitic carbon materials generated from methane pyrolysis using low-cost Fe ore catalysts show purities around 78 wt.%. Additional procedures, such as thermal or electrochemical treatment, are required to purify these carbon co-products before employing them in energy storage devices, complicating the process and increasing manufacturing costs. Thus, optimising the high-purity synthesis of graphitic carbon materials is imperative for their accommodation in energy storage devices. Meanwhile, developing methane pyrolysis technologies that simultaneously yield hydrogen with enhanced methane conversion and high-quality carbon co-products is critical for successful commercial implementation.

Modifying graphitic carbon with optimal structures: Graphitic carbon materials from methane pyrolysis using Fe ore catalysts are demonstrated as efficient conductive carbon additives and active materials for anode and cathode electrodes. Acting as conductive additives, they enable MnO_2 cathodes with high electrode conductivity and good electrolyte absorption capability, which further contribute to the zinc-carbon batteries with better rate performance, lower internal resistance, and superior long-term stability, compared with commercial carbon conductive additives (Super P). Regarding active electrode materials, these graphitic carbon materials with smaller crystalline sizes and larger surface areas favour faster surface redox reactions and better structural stability upon ion intercalation, leading to high-rate-performance dual-carbon batteries outperforming commercial natural and synthetic graphite. The carbon structures of graphitic carbon materials have strong effects on the intrinsic properties of carbon materials and the electrochemical performances of related cells; thus, modifying these carbon co-products with optimal structures (such as surface functionalization) is vital for achieving advanced energy storage systems with performance enhancement.

Evaluating other energy storage devices: In this work, zinc-carbon batteries and dual-carbon batteries are selected as the representative systems to demonstrate the effectiveness of graphitic carbon co-products from methane pyrolysis serving as conductive additives and active materials for electrodes, respectively. Currently, there is a lack of studies that evaluated energy storage applications for such carbon materials. Therefore, further investigations are necessary to validate the suitability of carbon co-products for other energy storage devices. For example, lithium-ion batteries that have already been commercialised and dominated the portable electronics market could be considered as a potential battery system to accommodate these carbon materials. As discussed in the section 1.4.2, LIBs utilizing graphite anode materials show the intercalation/de-intercalation mechanism for lithium storage, which is similar to the lithium storage process of the graphite/Li half cells with graphitic anodes

demonstrated in section 4.3.3. Thus, it is speculated that the graphitic carbon co-products from methane pyrolysis may work as anode electrode materials for LIBs. Besides lithium-ion batteries, other rechargeable battery systems that involve carbon materials are also worth exploring, such as sodium-ion batteries, potassium-ion batteries, zinc-air batteries, and carbon-enhanced lead-acid batteries. This could help to extend the value-added applications for the graphitic carbon materials from methane pyrolysis and enhance the economic viability of this low-emission hydrogen production process.

Reference

[1] P. Agreement, Paris agreement, report of the conference of the parties to the United Nations framework convention on climate change (21st session, 2015: Paris). Retrived December, HeinOnline, 2015, p. 2017.

[2] C.-F. Schleussner, J. Rogelj, M. Schaeffer, T. Lissner, R. Licker, E.M. Fischer, R. Knutti, A. Levermann, K. Frieler, W. Hare, Science and policy characteristics of the Paris Agreement temperature goal, Nature Climate Change 6(9) (2016) 827-835.

[3] S.J. Davis, N.S. Lewis, M. Shaner, S. Aggarwal, D. Arent, I.L. Azevedo, S.M. Benson, T. Bradley, J. Brouwer, Y.-M. Chiang, Net-zero emissions energy systems, Science 360(6396) (2018) eaas9793.

[4] J.M. Thomas, P.P. Edwards, P.J. Dobson, G.P. Owen, Decarbonising energy: The developing international activity in hydrogen technologies and fuel cells, J. Energy Chem. 51 (2020) 405-415.

[5] A.I. Osman, N. Mehta, A.M. Elgarahy, M. Hefny, A. Al-Hinai, A.a.H. Al-Muhtaseb, D.W. Rooney, Hydrogen production, storage, utilisation and environmental impacts: a review, Environmental Chemistry Letters (2022) 1-36.

[6] Q. Hassan, A.M. Abdulateef, S.A. Hafedh, A. Al-samari, J. Abdulateef, A.Z. Sameen, H.M. Salman, A.K. Al-Jiboory, S. Wieteska, M. Jaszczur, Renewable energy-to-green hydrogen: A review of main resources routes, processes and evaluation, Int. J. Hydrogen Energy (2023).

[7] M. Yue, H. Lambert, E. Pahon, R. Roche, S. Jemei, D. Hissel, Hydrogen energy systems: A critical review of technologies, applications, trends and challenges, Renewable Sustainable Energy Rev. 146 (2021) 111180.

[8] Z. Abdin, A. Zafaranloo, A. Rafiee, W. Mérida, W. Lipiński, K.R. Khalilpour, Hydrogen as an energy vector, Renewable Sustainable Energy Rev. 120 (2020) 109620.

[9] D. Tang, G.-L. Tan, G.-W. Li, J.-G. Liang, S.M. Ahmad, A. Bahadur, M. Humayun, H. Ullah, A. Khan, M. Bououdina, State-of-the-art hydrogen generation techniques and storage methods: A critical review, Journal of Energy Storage 64 (2023) 107196.

[10] S.E. Jose M Bermudez, Hydrogen, 2023. https://www.iea.org/reports/hydrogen. (Accessed 10 July 2023).

[11] S.R. Patlolla, K. Katsu, A. Sharafian, K. Wei, O.E. Herrera, W. Mérida, A review of methane pyrolysis technologies for hydrogen production, Renewable Sustainable Energy Rev. 181 (2023) 113323.

[12] IEA, Global Hydrogen Review 2022, 2022. https://www.iea.org/reports/global-hydrogen-review-2022.

[13] I.E. Agency, Global Hydrogen Review 2023, 2023.

[14] F. Birol, The future of hydrogen: seizing today's opportunities, IEA Report prepared for the G 20 (2019).

[15] M. Newborough, G. Cooley, Developments in the global hydrogen market: The spectrum of hydrogen colours, Fuel Cells Bulletin 2020(11) (2020) 16-22.

[16] B. Lumbers, J. Barley, F. Platte, Low-emission hydrogen production via the thermo-catalytic decomposition of methane for the decarbonisation of iron ore mines in Western Australia, Int. J. Hydrogen Energy 47(37) (2022) 16347-16361.

[17] M. Hermesmann, T. Müller, Green, turquoise, blue, or grey? Environmentally friendly hydrogen production in transforming energy systems, Progress in Energy and Combustion Science 90 (2022) 100996.

[18] N. Sánchez-Bastardo, R. Schlögl, H. Ruland, Methane pyrolysis for zero-emission hydrogen production: A potential bridge technology from fossil fuels to a renewable and sustainable hydrogen economy, Industrial & Engineering Chemistry Research 60(32) (2021) 11855-11881.

[19] N. Sánchez-Bastardo, R. Schlögl, H. Ruland, Methane pyrolysis for co2-free h2 production: A green process to overcome renewable energies unsteadiness, Chemie Ingenieur Technik 92(10) (2020) 1596-1609.

[20] B. Parkinson, M. Tabatabaei, D.C. Upham, B. Ballinger, C. Greig, S. Smart, E. McFarland, Hydrogen production using methane: Techno-economics of decarbonizing fuels and chemicals, Int. J. Hydrogen Energy 43(5) (2018) 2540-2555.

[21] L. Weger, A. Abánades, T. Butler, Methane cracking as a bridge technology to the hydrogen economy, Int. J. Hydrogen Energy 42(1) (2017) 720-731.

[22] O. Machhammer, A. Bode, W. Hormuth, Financial and ecological evaluation of hydrogen production processes on large scale, Chemical Engineering & Technology 39(6) (2016) 1185-1193.

[23] J. Riley, C. Atallah, R. Siriwardane, R. Stevens, Technoeconomic analysis for hydrogen and carbon Co-Production via catalytic pyrolysis of methane, Int. J. Hydrogen Energy 46(39) (2021) 20338-20358.

[24] M. McConnachie, M. Konarova, S. Smart, Literature review of the catalytic pyrolysis of methane for hydrogen and carbon production, Int. J. Hydrogen Energy (2023).

[25] S. Schneider, S. Bajohr, F. Graf, T. Kolb, State of the art of hydrogen production via pyrolysis of natural gas, ChemBioEng Reviews 7(5) (2020) 150-158.

[26] H.F. Abbas, W.W. Daud, Hydrogen production by methane decomposition: a review, Int. J. Hydrogen Energy 35(3) (2010) 1160-1190.

[27] H.F. Abbas, W.W. Daud, Thermocatalytic decomposition of methane for hydrogen production using activated carbon catalyst: Regeneration and characterization studies, Int. J. Hydrogen Energy 34(19) (2009) 8034-8045.

[28] A. Cornejo, H.T. Chua, A process for producing hydrogen and graphitic carbon from hydrocarbons, Google Patents, 2019.

[29] B. Eisenberg, Kinetics of methane pyrolysis, Yale University1965.

[30] K. Makarov, V. Pechik, Kinetics of methane pyrolysis under conditions of pyrolytic carbon formation, Carbon 12(4) (1974) 391-403.

[31] H. Grabke, Evidence on the surface concentration of carbon on gamma iron from the kinetics of the carburization in CH 4− H 2, Metallurgical Transactions 1 (1970) 2972-2975.

[32] J.-W. Snoeck, G. Froment, M. Fowles, Kinetic study of the carbon filament formation by methane cracking on a nickel catalyst, Journal of Catalysis 169(1) (1997) 250-262.

[33] J. Wang, X. Li, Y. Zhou, G. Yu, L. Jin, H. Hu, Mechanism of methane decomposition with hydrogen addition over activated carbon via in-situ pyrolysis-electron impact ionization time-of-flight mass spectrometry, Fuel 263 (2020) 116734.

[34] Q. Chen, A.C. Lua, Kinetic reaction and deactivation studies on thermocatalytic decomposition of methane by electroless nickel plating catalyst, Chemical Engineering Journal 389 (2020) 124366.

[35] D. Bae, Y. Kim, E.H. Ko, S.J. Han, J.W. Lee, M. Kim, D. Kang, Methane pyrolysis and carbon formation mechanisms in molten manganese chloride mixtures, Applied Energy 336 (2023) 120810.

[36] T. Kreuger, W. van Swaaij, S. Kersten, Methane pyrolysis over porous particles, Catal. Today 420 (2023) 114058.

[37] Z. Fan, W. Weng, J. Zhou, D. Gu, W. Xiao, Catalytic decomposition of methane to produce hydrogen: A review, J. Energy Chem. 58 (2021) 415-430.

[38] M. Ouyang, P. Boldrin, R.C. Maher, X. Chen, X. Liu, L.F. Cohen, N.P. Brandon, A mechanistic study of the interactions between methane and nickel supported on doped ceria, Applied Catalysis B: Environmental 248 (2019) 332-340.

[39] N. Bayat, M. Rezaei, F. Meshkani, Methane decomposition over Ni–Fe/Al2O3 catalysts for production of COx-free hydrogen and carbon nanofiber, Int. J. Hydrogen Energy 41(3) (2016) 1574-1584.

[40] R.A. Dagle, V. Dagle, M.D. Bearden, J.D. Holladay, T.R. Krause, S. Ahmed, An overview of natural gas conversion technologies for co-production of hydrogen and value-added solid carbon products, (2017).

[41] A. Rastegarpanah, M. Rezaei, F. Meshkani, K. Zhang, X. Zhao, W. Pei, Y. Liu, J. Deng, H. Arandiyan, H. Dai, Influence of group VIB metals on activity of the Ni/MgO catalysts for methane decomposition, Applied Catalysis B: Environmental 248 (2019) 515-525.

[42] N. Bayat, F. Meshkani, M. Rezaei, Thermocatalytic decomposition of methane to COx-free hydrogen and carbon over Ni–Fe–Cu/Al2O3 catalysts, Int. J. Hydrogen Energy 41(30) (2016) 13039-13049.

[43] A.E. Awadallah, A.A. Aboul-Enein, A.H. Mahmoud, S.S. Abd El Rehim, A.K. El-Ziaty, A.K. Aboul-Gheit, ZrxMg1-xO supported cobalt catalysts for methane decomposition into CO x-free hydrogen and carbon nanotubes, International Journal of Green Energy 15(10) (2018) 568-576.

[44] Z. Zhong, H. Chen, S. Tang, J. Ding, J. Lin, K.L. Tan, Catalytic growth of carbon nanoballs with and without cobalt encapsulation, Chemical Physics Letters 330(1-2) (2000) 41-47.

[45] U. Ashik, W.W. Daud, H.F. Abbas, Production of greenhouse gas free hydrogen by thermocatalytic decomposition of methane–A review, Renewable Sustainable Energy Rev. 44 (2015) 221-256.

[46] J. Zhang, X. Li, H. Chen, M. Qi, G. Zhang, H. Hu, X. Ma, Hydrogen production by catalytic methane decomposition: carbon materials as catalysts or catalyst supports, Int. J. Hydrogen Energy 42(31) (2017) 19755-19775.

[47] B. Fidalgo, N. Muradov, J. Menéndez, Effect of H2S on carbon-catalyzed methane decomposition and CO2 reforming reactions, Int. J. Hydrogen Energy 37(19) (2012) 14187-14194.

[48] J. Zhang, X. Li, W. Xie, Q. Hao, H. Chen, X. Ma, K2CO3-promoted methane pyrolysis on nickel/coal-char hybrids, Journal of Analytical and Applied Pyrolysis 136 (2018) 53-61.

[49] Z. Fang, R.L. Smith, X. Qi, Production of hydrogen from renewable resources, Springer2015.

[50] D.C. Upham, V. Agarwal, A. Khechfe, Z.R. Snodgrass, M.J. Gordon, H. Metiu, E.W. McFarland, Catalytic molten metals for the direct conversion of methane to hydrogen and separable carbon, Science 358(6365) (2017) 917-921.

[51] B. Parkinson, C.F. Patzschke, D. Nikolis, S. Raman, D.C. Dankworth, K. Hellgardt, Methane pyrolysis in monovalent alkali halide salts: Kinetics and pyrolytic carbon properties, Int. J. Hydrogen Energy 46(9) (2021) 6225-6238.

[52] J. Prabowo, L. Lai, B. Chivers, D. Burke, A.H. Dinh, L. Ye, Y. Wang, Y. Wang, L. Wei, Y. Chen, Solid carbon co-products from hydrogen production by methane pyrolysis: Current understandings and recent progress, Carbon (2023) 118507.

[53] R. Guil-Lopez, J. Botas, J. Fierro, D. Serrano, Comparison of metal and carbon catalysts for hydrogen production by methane decomposition, Appl. Catal., A 396(1-2) (2011) 40-51.

[54] N.S.N. Hasnan, S.N. Timmiati, K.L. Lim, Z. Yaakob, N.H.N. Kamaruddin, L.P. Teh, Recent developments in methane decomposition over heterogeneous catalysts: an overview, Materials for Renewable and Sustainable Energy 9 (2020) 1-18.

[55] R. Baker, Catalytic growth of carbon filaments, Carbon 27(3) (1989) 315-323.

[56] R. Baker, M. Barber, P. Harris, F. Feates, R. Waite, Nucleation and growth of carbon deposits from the nickel catalyzed decomposition of acetylene, Journal of catalysis 26(1) (1972) 51-62.

[57] N. Bayat, M. Rezaei, F. Meshkani, Hydrogen and carbon nanofibers synthesis by methane decomposition over Ni–Pd/Al2O3 catalyst, Int. J. Hydrogen Energy 41(12) (2016) 5494-5503.

[58] S. Iijima, Direct observation of the tetrahedral bonding in graphitized carbon black by high resolution electron microscopy, Journal of Crystal Growth 50(3) (1980) 675-683.

[59] C. He, N. Zhao, C. Shi, X. Du, J. Li, Carbon nanotubes and onions from methane decomposition using Ni/Al catalysts, Materials chemistry and physics 97(1) (2006) 109-115.

[60] C. Zhang, J. Li, C. Shi, C. He, E. Liu, N. Zhao, Effect of Ni, Fe and Fe-Ni alloy catalysts on the synthesis of metal contained carbon nano-onions and studies of their electrochemical hydrogen storage properties, J. Energy Chem. 23(3) (2014) 324-330.

[61] M. Keller, A. Matsumura, A. Sharma, Spray-dried Fe/Al2O3 as a carbon carrier for COx-free hydrogen production via methane cracking in a fluidized bed process, Chemical Engineering Journal 398 (2020) 125612.

[62] W. Liang, H. Yan, C. Chen, D. Lin, K. Tan, X. Feng, Y. Liu, X. Chen, C. Yang, H. Shan, Revealing the effect of nickel particle size on carbon formation type in the methane decomposition reaction, Catalysts 10(8) (2020) 890.

[63] S. Tong, B. Miao, L. Zhang, S.H. Chan, Decarbonizing natural gas: A review of catalytic decomposition and carbon formation mechanisms, Energies 15(7) (2022) 2573.

[64] W. Zhang, L. Gao, M. Zhang, J. Cui, Y. Li, L. Gao, S. Zhang, Methane catalytic cracking to make hydrogen and graphitic nano carbons (Nanotubes, Microfibers, Microballs, Onions) with zero emission, Synthesis and Reactivity in Inorganic, Metal-Organic, and Nano-Metal Chemistry 44(8) (2014) 1166-1174.

[65] M. Pudukudy, Z. Yaakob, M.S. Takriff, Methane decomposition over unsupported mesoporous nickel ferrites: effect of reaction temperature on the catalytic activity and properties of the produced nanocarbon, RSC advances 6(72) (2016) 68081-68091.

[66] H. Nishii, D. Miyamoto, Y. Umeda, H. Hamaguchi, M. Suzuki, T. Tanimoto, T. Harigai, H. Takikawa, Y. Suda, Catalytic activity of several carbons with different structures for methane decomposition and by-produced carbons, Applied Surface Science 473 (2019) 291-297.

[67] R. Vander Wal, M. Makiesse Nkiawete, Carbons as catalysts in thermo-catalytic hydrocarbon decomposition: a review, C 6(2) (2020) 23.

[68] Y. Schwob, F. Fischer, L. Fulcheri, P. Willemez, Conversion of carbon or carbon-containing compounds in a plasma, Google Patents, 2000.

[69] S.-J. Park, S.-J. Park, History and structure of carbon fibers, Carbon Fibers (2018) 1-30.

[70] M. Holmes, Global carbon fibre market remains on upward trend, Reinforced Plastics 58(6) (2014) 38-45.

[71] C. Zhang, W. Zhang, N.E. Drewett, X. Wang, S.J. Yoo, H. Wang, T. Deng, J.G. Kim, H. Chen, K. Huang, Integrating catalysis of methane decomposition and electrocatalytic hydrogen evolution with Ni/CeO2 for improved hydrogen production efficiency, ChemSusChem 12(5) (2019) 1000-1010.

[72] Y. Yao, L. Lai, Z. Yu, Y. Pan, Y. Yu, V. Lo, A. Roy, B. Chivers, X. Zhong, L. Wei, Carbon/iron by-product from catalytic methane decomposition as recyclable Fenton catalyst for pollutant degradation, Journal of Hazardous Materials 437 (2022) 129328.

[73] Y. Ji, C. Palmer, E.E. Foley, R. Giovine, E. Yoshida, E. Sebti, A. Patterson, E. McFarland, R. Clément, Valorizing the carbon byproduct of methane pyrolysis in batteries, Carbon 204 (2023) 26-35.

[74] G.W. Vinal, Primary batteries, New York, 1950.

[75] T.B. Reddy, Linden's handbook of batteries, McGraw-Hill Education2011.

[76] C. Daniel, J.O. Besenhard, Handbook of battery materials, John Wiley & Sons2012.

[77] J. Ni, Y. Li, Carbon nanomaterials in different dimensions for electrochemical energy storage, Adv. Energy Mater. 6(17) (2016) 1600278.

[78] J. Xiao, J. Han, C. Zhang, G. Ling, F. Kang, Q.H. Yang, Dimensionality, function and performance of carbon materials in energy storage devices, Adv. Energy Mater. 12(4) (2022) 2100775.

[79] J. Entwistle, R. Ge, K. Pardikar, R. Smith, D. Cumming, Carbon binder domain networks and electrical conductivity in lithium-ion battery electrodes: A critical review, Renewable Sustainable Energy Rev. 166 (2022) 112624.

[80] I. Cho, J. Choi, K. Kim, M.-H. Ryou, Y.M. Lee, A comparative investigation of carbon black (Super-P) and vapor-grown carbon fibers (VGCFs) as conductive additives for lithium-ion battery cathodes, Rsc Advances 5(115) (2015) 95073-95078.

[81] C. Li, X. Zhang, K. Wang, H.-t. Zhang, X.-z. Sun, Y.-w. Ma, Three dimensional graphene networks for supercapacitor electrode materials, New Carbon Materials 30(3) (2015) 193-206.

[82] C. Tang, Q. Zhang, M.Q. Zhao, J.Q. Huang, X.B. Cheng, G.L. Tian, H.J. Peng, F. Wei, Nitrogen-doped aligned carbon nanotube/graphene sandwiches: facile catalytic growth on

bifunctional natural catalysts and their applications as scaffolds for high-rate lithium-sulfur batteries, Adv. Mater. 26(35) (2014) 6100-6105.

[83] Z. Yang, J. Ren, Z. Zhang, X. Chen, G. Guan, L. Qiu, Y. Zhang, H. Peng, Recent advancement of nanostructured carbon for energy applications, Chemical reviews 115(11) (2015) 5159-5223.

[84] G. Wang, M. Yu, X. Feng, Carbon materials for ion-intercalation involved rechargeable battery technologies, Chem. Soc. Rev. 50(4) (2021) 2388-2443.

[85] T. Nagaura, K. Tozawa, Progress in batteries and solar cells, JEC Press 9 (1990) 209.

[86] L. Li, D. Zhang, J. Deng, Y. Gou, J. Fang, H. Cui, Y. Zhao, M. Cao, Carbon-based materials for fast charging lithium-ion batteries, Carbon 183 (2021) 721-734.

[87] Y. Chen, J. Key, K. O'regan, T. Song, Y. Han, E. Kendrick, Revealing the rate-limiting electrode of lithium batteries at high rates and mass loadings, Chemical Engineering Journal 450 (2022) 138275.

[88] S.-M. Lee, J. Kim, J. Moon, K.-N. Jung, J.H. Kim, G.-J. Park, J.-H. Choi, D.Y. Rhee, J.-S. Kim, J.-W. Lee, A cooperative biphasic MoO x–MoP x promoter enables a fast-charging lithium-ion battery, Nat. Commun. 12(1) (2021) 39.

[89] Y.-O. Kim, S.-M. Park, Intercalation mechanism of lithium ions into graphite layers studied by nuclear magnetic resonance and impedance experiments, J. Electrochem. Soc. 148(3) (2001) A194.

[90] J.-H. Shim, S. Lee, Characterization of graphite etched with potassium hydroxide and its application in fast-rechargeable lithium ion batteries, J. Power Sources 324 (2016) 475-483.

[91] Q. Cheng, Y. Zhang, Multi-channel graphite for high-rate lithium ion battery, J. Electrochem. Soc. 165(5) (2018) A1104.

[92] J. Kim, S.M.N. Jeghan, G. Lee, Superior fast-charging capability of graphite anode via facile surface treatment for lithium-ion batteries, Microporous and Mesoporous Materials 305 (2020) 110325.

[93] D.-K. Son, J. Kim, M.R. Raj, G. Lee, Elucidating the structural redox behaviors of nanostructured expanded graphite anodes toward fast-charging and high-performance lithium-ion batteries, Carbon 175 (2021) 187-201.

[94] Q. Cheng, R. Yuge, K. Nakahara, N. Tamura, S. Miyamoto, KOH etched graphite for fast chargeable lithium-ion batteries, J. Power Sources 284 (2015) 258-263.

[95] M. Tebyetekerwa, T.T. Duignan, Z. Xu, X. Song Zhao, Rechargeable Dual-Carbon Batteries: A Sustainable Battery Technology, Adv. Energy Mater. 12(44) (2022) 2202450.

[96] S. Iijima, Helical microtubules of graphitic carbon, nature 354(6348) (1991) 56-58.

[97] S. Iijima, Carbon nanotubes: past, present, and future, Physica B: Condensed Matter 323(1-4) (2002) 1-5.

[98] E. Frackowiak, F. Beguin, Electrochemical storage of energy in carbon nanotubes and nanostructured carbons, Carbon 40(10) (2002) 1775-1787.

[99] C. De las Casas, W. Li, A review of application of carbon nanotubes for lithium ion battery anode material, J. Power Sources 208 (2012) 74-85.

[100] B.J. Landi, M.J. Ganter, C.D. Cress, R.A. DiLeo, R.P. Raffaelle, Carbon nanotubes for lithium ion batteries, Energy Environ. Sci. 2(6) (2009) 638-654.

[101] L. Sun, X. Wang, Y. Wang, Q. Zhang, Roles of carbon nanotubes in novel energy storage devices, Carbon 122 (2017) 462-474.

[102] L. Dai, D.W. Chang, J.B. Baek, W. Lu, Carbon nanomaterials for advanced energy conversion and storage, Small 8(8) (2012) 1130-1166.

[103] P. Sehrawat, C. Julien, S. Islam, Carbon nanotubes in Li-ion batteries: A review, Materials Science and Engineering: B 213 (2016) 12-40.

[104] B. Gao, A. Kleinhammes, X. Tang, C. Bower, L. Fleming, Y. Wu, O. Zhou, Electrochemical intercalation of single-walled carbon nanotubes with lithium, Chemical physics letters 307(3-4) (1999) 153-157.

[105] G. Maurin, C. Bousquet, F. Henn, P. Bernier, R. Almairac, B. Simon, Electrochemical lithium intercalation into multiwall carbon nanotubes: a micro-Raman study, Solid State Ionics 136 (2000) 1295-1299.

[106] F. Leroux, K. Metenier, S. Gautier, E. Frackowiak, S. Bonnamy, F. Beguin, Electrochemical insertion of lithium in catalytic multi-walled carbon nanotubes, J. Power Sources 81 (1999) 317-322.

[107] S. Kawasaki, T. Hara, Y. Iwai, Y. Suzuki, Metallic and semiconducting single-walled carbon nanotubes as the anode material of Li ion secondary battery, Materials Letters 62(17-18) (2008) 2917-2920.

[108] R.S. Morris, B.G. Dixon, T. Gennett, R. Raffaelle, M.J. Heben, High-energy, rechargeable Li-ion battery based on carbon nanotube technology, J. Power Sources 138(1-2) (2004) 277-280.

[109] X.X. Wang, J.N. Wang, H. Chang, Y.F. Zhang, Preparation of short carbon nanotubes and application as an electrode material in Li-ion batteries, Adv. Funct. Mater. 17(17) (2007) 3613-3618.

[110] E. Frackowiak, S. Gautier, H. Gaucher, S. Bonnamy, F. Beguin, Electrochemical storage of lithium in multiwalled carbon nanotubes, Carbon 37(1) (1999) 61-69.

[111] A.S. Claye, J.E. Fischer, C.B. Huffman, A.G. Rinzler, R.E. Smalley, Solid-state electrochemistry of the Li single wall carbon nanotube system, J. Electrochem. Soc. 147(8) (2000) 2845.

[112] J. Eom, H.-S. Kwon, J. Liu, O. Zhou, Lithium insertion into purified and etched multi-walled carbon nanotubes synthesized on supported catalysts by thermal CVD, Carbon 42(12-13) (2004) 2589-2596.

[113] J.-X. Li, Y. Zhao, L.-H. Guan, Lithium storage in single-walled carbon nanotubes, Electrochemistry communications 12(4) (2010) 592-595.

[114] H.S. Nalwa, Encyclopedia of nanoscience and nanotechnology (v. 8. Ne-P), American scientific publishers2004.

[115] M. Zhao, Y. Xia, L. Mei, Diffusion and condensation of lithium atoms in single-walled carbon nanotubes, Physical Review B—Condensed Matter and Materials Physics 71(16) (2005) 165413.

[116] H. Shimoda, B. Gao, X. Tang, A. Kleinhammes, L. Fleming, Y. Wu, O. Zhou, Lithium intercalation into opened single-wall carbon nanotubes: storage capacity and electronic properties, Physical review letters 88(1) (2001) 015502.

[117] W.H. Shin, H.M. Jeong, B.G. Kim, J.K. Kang, J.W. Choi, Nitrogen-doped multiwall carbon nanotubes for lithium storage with extremely high capacity, Nano letters 12(5) (2012) 2283-2288.

[118] L. Qie, W.M. Chen, Z.H. Wang, Q.G. Shao, X. Li, L.X. Yuan, X.L. Hu, W.X. Zhang, Y.H. Huang, Nitrogen-doped porous carbon nanofiber webs as anodes for lithium ion batteries with a superhigh capacity and rate capability, Adv. Mater. 24(15) (2012) 2047-2050.

[119] S. Zhong, H. Liu, D. Wei, J. Hu, H. Zhang, H. Hou, M. Peng, G. Zhang, H. Duan, Long-aspect-ratio N-rich carbon nanotubes as anode material for sodium and lithium ion batteries, Chemical Engineering Journal 395 (2020) 125054.

[120] B. Gao, C. Bower, J. Lorentzen, L. Fleming, A. Kleinhammes, X. Tang, L. McNeil, Y. Wu, O. Zhou, Enhanced saturation lithium composition in ball-milled single-walled carbon nanotubes, Chemical Physics Letters 327(1-2) (2000) 69-75.

[121] X. Li, J. Liu, Y. Zhang, Y. Li, H. Liu, X. Meng, J. Yang, D. Geng, D. Wang, R. Li, High concentration nitrogen doped carbon nanotube anodes with superior Li+ storage performance for lithium rechargeable battery application, J. Power Sources 197 (2012) 238-245.

[122] J. Li, F. Zhang, C. Wang, C. Shao, B. Li, Y. Li, Q.-H. Wu, Y. Yang, Self nitrogen-doped carbon nanotubes as anode materials for high capacity and cycling stability lithium-ion batteries, Materials & Design 133 (2017) 169-175.

[123] G. Kucinskis, G. Bajars, J. Kleperis, Graphene in lithium ion battery cathode materials: A review, J. Power Sources 240 (2013) 66-79.

[124] J. Zhu, R. Duan, S. Zhang, N. Jiang, Y. Zhang, J. Zhu, The application of graphene in lithium ion battery electrode materials, SpringerPlus 3(1) (2014) 1-8.

[125] X. Li, X. Wang, L. Zhang, S. Lee, H. Dai, Chemically derived, ultrasmooth graphene nanoribbon semiconductors, science 319(5867) (2008) 1229-1232.

[126] J.C. Meyer, A.K. Geim, M.I. Katsnelson, K.S. Novoselov, T.J. Booth, S. Roth, The structure of suspended graphene sheets, Nature 446(7131) (2007) 60-63.

[127] S. Gilje, S. Han, M. Wang, K.L. Wang, R.B. Kaner, A chemical route to graphene for device applications, Nano letters 7(11) (2007) 3394-3398.

[128] E. Yoo, J. Kim, E. Hosono, H.-s. Zhou, T. Kudo, I. Honma, Large reversible Li storage of graphene nanosheet families for use in rechargeable lithium ion batteries, Nano letters 8(8) (2008) 2277-2282.

[129] S. Yu, B. Guo, T. Zeng, H. Qu, J. Yang, J. Bai, Graphene-based lithium-ion battery anode materials manufactured by mechanochemical ball milling process: A review and perspective, Composites Part B: Engineering (2022) 110232.

[130] A. Rajkamal, R. Thapa, Carbon allotropes as anode material for lithium-ion batteries, Advanced Materials Technologies 4(10) (2019) 1900307.

[131] C. Wang, D. Li, C.O. Too, G.G. Wallace, Electrochemical properties of graphene paper electrodes used in lithium batteries, Chemistry of materials 21(13) (2009) 2604-2606.

[132] D. Pan, S. Wang, B. Zhao, M. Wu, H. Zhang, Y. Wang, Z. Jiao, Li storage properties of disordered graphene nanosheets, Chemistry of materials 21(14) (2009) 3136-3142.

[133] C. Uthaisar, V. Barone, Edge effects on the characteristics of Li diffusion in graphene, Nano letters 10(8) (2010) 2838-2842.

[134] Z.-S. Wu, W. Ren, L. Xu, F. Li, H.-M. Cheng, Doped graphene sheets as anode materials with superhigh rate and large capacity for lithium ion batteries, ACS nano 5(7) (2011) 5463-5471.

[135] D. Wang, D. Choi, J. Li, Z. Yang, Z. Nie, R. Kou, D. Hu, C. Wang, L.V. Saraf, J. Zhang, Self-assembled TiO2–graphene hybrid nanostructures for enhanced Li-ion insertion, ACS nano 3(4) (2009) 907-914.

[136] D. Wang, R. Kou, D. Choi, Z. Yang, Z. Nie, J. Li, L.V. Saraf, D. Hu, J. Zhang, G.L. Graff, Ternary self-assembly of ordered metal oxide− graphene nanocomposites for electrochemical energy storage, ACS nano 4(3) (2010) 1587-1595.

[137] H. Wang, L.-F. Cui, Y. Yang, H. Sanchez Casalongue, J.T. Robinson, Y. Liang, Y. Cui, H. Dai, Mn3O4− graphene hybrid as a high-capacity anode material for lithium ion batteries, J. Am. Chem. Soc. 132(40) (2010) 13978-13980.

[138] K. Chang, D. Geng, X. Li, J. Yang, Y. Tang, M. Cai, R. Li, X. Sun, Ultrathin MoS2/nitrogen-doped graphene nanosheets with highly reversible lithium storage, Adv. Energy Mater. 3(7) (2013) 839-844.

[139] C. Gao, Z. Jiang, P. Wang, L.R. Jensen, Y. Zhang, Y. Yue, Optimized assembling of MOF/SnO2/Graphene leads to superior anode for lithium ion batteries, Nano Energy 74 (2020) 104868.

[140] R. Mo, X. Tan, F. Li, R. Tao, J. Xu, D. Kong, Z. Wang, B. Xu, X. Wang, C. Wang, Tin-graphene tubes as anodes for lithium-ion batteries with high volumetric and gravimetric energy densities, Nat. Commun. 11(1) (2020) 1374.

[141] H. Xue, Y. Wu, Y. Zou, Y. Shen, G. Liu, Q. Li, D. Yin, L. Wang, J. Ming, Unraveling metal oxide role in exfoliating graphite: new strategy to construct high-performance graphene-modified SiOx-based anode for lithium-ion batteries, Adv. Funct. Mater. 30(21) (2020) 1910657.

[142] G. Li, Y. Li, H. Liu, Y. Guo, Y. Li, D. Zhu, Architecture of graphdiyne nanoscale films, Chem. Commun. 46(19) (2010) 3256-3258.

[143] S. Chen, Y. Xue, Y. Li, 2D graphdiyne, what's next?, Next Materials 1(3) (2023) 100031.

[144] X. Zheng, S. Chen, J. Li, H. Wu, C. Zhang, D. Zhang, X. Chen, Y. Gao, F. He, L. Hui, Two-dimensional carbon graphdiyne: Advances in fundamental and application research, ACS nano 17(15) (2023) 14309-14346.

[145] H. Yu, Y. Xue, Y. Li, Graphdiyne and its assembly architectures: synthesis, functionalization, and applications, Adv. Mater. 31(42) (2019) 1803101.

[146] M. Long, L. Tang, D. Wang, Y. Li, Z. Shuai, Electronic structure and carrier mobility in graphdiyne sheet and nanoribbons: theoretical predictions, ACS nano 5(4) (2011) 2593-2600.

[147] Z. Jia, Y. Li, Z. Zuo, H. Liu, C. Huang, Y. Li, Synthesis and Properties of 2D Carbon□ Graphdiyne, Accounts of chemical research 50(10) (2017) 2470-2478.

[148] Z. Zheng, Y. Xue, Y. Li, A new carbon allotrope: graphdiyne, Trends in Chemistry 4(8) (2022) 754-768.

[149] B. Jang, J. Koo, M. Park, H. Lee, J. Nam, Y. Kwon, H. Lee, Graphdiyne as a high-capacity lithium ion battery anode material, Applied Physics Letters 103(26) (2013).

[150] H. Zhang, Y. Xia, H. Bu, X. Wang, M. Zhang, Y. Luo, M. Zhao, Graphdiyne: A promising anode material for lithium ion batteries with high capacity and rate capability, Journal of Applied Physics 113(4) (2013).

[151] C. Sun, D.J. Searles, Lithium storage on graphdiyne predicted by DFT calculations, J. Phys. Chem. C 116(50) (2012) 26222-26226.

[152] H. Zhang, M. Zhao, X. He, Z. Wang, X. Zhang, X. Liu, High mobility and high storage capacity of lithium in sp–sp2 hybridized carbon network: the case of graphyne, J. Phys. Chem. C 115(17) (2011) 8845-8850.

[153] C. Huang, S. Zhang, H. Liu, Y. Li, G. Cui, Y. Li, Graphdiyne for high capacity and long-life lithium storage, Nano Energy 11 (2015) 481-489.

[154] H. Shang, Z. Zuo, L. Li, F. Wang, H. Liu, Y. Li, Y. Li, Ultrathin graphdiyne nanosheets grown in situ on copper nanowires and their performance as lithium-ion battery anodes, Angew. Chem., Int. Ed. 57(3) (2018) 774-778.

[155] S. Zhang, H. Du, J. He, C. Huang, H. Liu, G. Cui, Y. Li, Nitrogen-doped graphdiyne applied for lithium-ion storage, ACS applied materials & interfaces 8(13) (2016) 8467-8473.

[156] Y. Leng, Materials characterization: introduction to microscopic and spectroscopic methods, John Wiley & Sons2013.

[157] S. Rathinavel, K. Priyadharshini, D. Panda, A review on carbon nanotube: An overview of synthesis, properties, functionalization, characterization, and the application, Materials Science and Engineering: B 268 (2021) 115095.

[158] P.K. Chu, L. Li, Characterization of amorphous and nanocrystalline carbon films, Materials chemistry and physics 96(2-3) (2006) 253-277.

[159] X. Jie, J. Wang, S. Gonzalez-Cortes, B. Yao, W. Li, Y. Gao, J.R. Dilworth, T. Xiao, P.P. Edwards, Catalytic activity of various carbons during the microwave-initiated deep dehydrogenation of hexadecane, JACS Au 1(11) (2021) 2021-2032.

[160] S. Zhang, L. Li, A. Kumar, Materials characterization techniques, CRC press2008.

[161] K. Jurkiewicz, M. Pawlyta, A. Burian, Structure of carbon materials explored by local transmission electron microscopy and global powder diffraction probes, C 4(4) (2018) 68.

[162] Y. Chen, X. Li, X. Zhou, H. Yao, H. Huang, Y.-W. Mai, L. Zhou, Hollow-tunneled graphitic carbon nanofibers through Ni-diffusion-induced graphitization as high-performance anode materials, Energy Environ. Sci. 7(8) (2014) 2689-2696.

[163] Q.T. Ain, S.H. Haq, A. Alshammari, M.A. Al-Mutlaq, M.N. Anjum, The systemic effect of PEG-nGO-induced oxidative stress in vivo in a rodent model, Beilstein journal of nanotechnology 10(1) (2019) 901-911.

[164] Y. Pan, L. Cao, Y. Yao, Y. Tao, V. Lo, Z. Zheng, B. Chivers, J. Prabowo, F. Liu, L. Lai, Graphitic Co-Products of Clean Hydrogen Production Enabling High-Rate-Performance Dual-Carbon Batteries, Adv. Energy Mater. (2023) 2300495.

[165] S. Yurdakal, C. Garlisi, L. Özcan, M. Bellardita, G. Palmisano, (Photo) catalyst characterization techniques: adsorption isotherms and BET, SEM, FTIR, UV–Vis, photoluminescence, and electrochemical characterizations, Heterogeneous photocatalysis, Elsevier2019, pp. 87-152.

[166] F. Fu, L. Lin, E. Xu, Functional pretreatments of natural raw materials, Advanced high strength natural fibre composites in construction, Elsevier2017, pp. 87-114.

[167] K.S. Sing, Reporting physisorption data for gas/solid systems with special reference to the determination of surface area and porosity (Recommendations 1984), Pure and applied chemistry 57(4) (1985) 603-619.

[168] R.L. McCreery, Raman spectroscopy for chemical analysis, John Wiley & Sons2005.

[169] S.K. Sharma, M.J. Egan, Raman Spectroscopy, Remote Compositional Analysis: Techniques for understanding spectroscopy, mineralogy, and geochemistry of planetary surfaces (2019) 120-146.

[170] P. Vandenabeele, Practical Raman spectroscopy: an introduction, John Wiley & Sons2013.

[171] M. Dresselhaus, A. Fung, A. Rao, S. Di Vittorio, K. Kuriyama, G. Dresselhaus, M. Endo, New characterization techniques for activated carbon fibers, Carbon 30(7) (1992) 1065-1073.

[172] H. Seyama, M. Soma, B. Theng, X-ray photoelectron spectroscopy, Developments in Clay Science, Elsevier2013, pp. 161-176.

[173] J.C. Vickerman, I.S. Gilmore, Surface analysis: the principal techniques, John Wiley & Sons2011.

[174] Z. Lu, G. Chen, S. Siahrostami, Z. Chen, K. Liu, J. Xie, L. Liao, T. Wu, D. Lin, Y. Liu, High-efficiency oxygen reduction to hydrogen peroxide catalysed by oxidized carbon materials, Nat. Catal. 1(2) (2018) 156-162.

[175] G. Bontempelli, R. Toniolo, Voltammetry-Linear sweep and cyclic, Encyclopedia of Analytical Science, Second Edition, Elsevier Applied Science2005, pp. 188-197.

[176] S. Parhi, N. Dash, S. Praharaj, D. Rout, An overview of voltammetric techniques to the present era, Electrochemical Sensors Based on Carbon Composite Materials: Fabrication, properties and applications (2022) 1-1-1-24.

[177] V.D. Parker, Linear sweep and cyclic voltammetry, Comprehensive Chemical Kinetics, Elsevier1986, pp. 145-202.

[178] Q. Wu, T. He, Y. Zhang, J. Zhang, Z. Wang, Y. Liu, L. Zhao, Y. Wu, F. Ran, Cyclic stability of supercapacitors: materials, energy storage mechanism, test methods, and device, Journal of Materials Chemistry A 9(43) (2021) 24094-24147.

[179] L.A. Middlemiss, A.J. Rennie, R. Sayers, A.R. West, Characterisation of batteries by electrochemical impedance spectroscopy, Energy Reports 6 (2020) 232-241.

[180] S. Wang, J. Zhang, O. Gharbi, V. Vivier, M. Gao, M.E. Orazem, Electrochemical impedance spectroscopy, Nature Reviews Methods Primers 1(1) (2021) 41.

[181] C.M. Brett, Electrochemical impedance spectroscopy in the characterisation and application of modified electrodes for electrochemical sensors and biosensors, Molecules 27(5) (2022) 1497.

[182] A.C. Lazanas, M.I. Prodromidis, Electrochemical impedance spectroscopy─ a tutorial, ACS Measurement Science Au 3(3) (2023) 162-193.

[183] W. Choi, H.-C. Shin, J.M. Kim, J.-Y. Choi, W.-S. Yoon, Modeling and applications of electrochemical impedance spectroscopy (EIS) for lithium-ion batteries, Journal of Electrochemical Science and Technology 11(1) (2020) 1-13.

[184] F. Licht, M. Davis, H. Andreas, Charge redistribution and electrode history impact galvanostatic charging/discharging and associated figures of merit, J. Power Sources 446 (2020) 227354.

[185] S. Sharma, P. Chand, Supercapacitor and electrochemical techniques: A brief review, Results in Chemistry 5 (2023) 100885.

[186] Y. Sun, G. Yang, H. Cui, J. Wang, C. Wang, Zn x Ge1–x O 3D Micronano Structures with Excellent Performance as Anode Material in Lithium Ion Battery, ACS Applied Materials & Interfaces 7(28) (2015) 15230-15239.

[187] I. Dincer, C. Acar, Review and evaluation of hydrogen production methods for better sustainability, International Journal of Hydrogen Energy 40(34) (2015) 11094-11111.

[188] P. Nikolaidis, A. Poullikkas, A comparative overview of hydrogen production processes, Renewable & Sustainable Energy Reviews 67 (2017) 597-611.

[189] T.D. Veras, T.S. Mozer, D. dos Santos, A.D. Cesar, Hydrogen: Trends, production and characterization of the main process worldwide, International Journal of Hydrogen Energy 42(4) (2017) 2018-2033.

[190] T. Zhang, M.D. Amiridis, Hydrogen production via the direct cracking of methane over silica-supported nickel catalysts, Appl. Catal., A 167(2) (1998) 161-172.

[191] U.P.M. Ashik, W.M.A. Wan Daud, H.F. Abbas, Production of greenhouse gas free hydrogen by thermocatalytic decomposition of methane – A review, Renewable Sustainable Energy Rev. 44 (2015) 221-256.

[192] U.P.M. Ashik, W. Daud, J. Hayashi, A review on methane transformation to hydrogen and nanocarbon: Relevance of catalyst characteristics and experimental parameters on yield, Renewable Sustainable Energy Rev. 76 (2017) 743-767.

[193] J.X. Qian, T.W. Chen, L.R. Enakonda, D.B. Liu, J.M. Basset, L. Zhou, Methane decomposition to pure hydrogen and carbon nano materials: State-of-the-art and future perspectives, Int. J. Hydrogen Energy 45(32) (2020) 15721-15743.

[194] Z.Y. Fan, W. Weng, J. Zhou, D. Gu, W. Xiao, Catalytic decomposition of methane to produce hydrogen: A review, J. Energy Chem. 58 (2021) 415-430.

[195] L. Alves, V. Pereira, T. Lagarteira, A. Mendes, Catalytic methane decomposition to boost the energy transition: Scientific and technological advancements, Renewable Sustainable Energy Rev. 137 (2021).

[196] J.B. Zhang, X. Li, H.Y. Chen, M. Qi, G.R. Zhang, H.Q. Hu, X.X. Ma, Hydrogen production by catalytic methane decomposition: Carbon materials as catalysts or catalyst supports, Int. J. Hydrogen Energy 42(31) (2017) 19755-19775.

[197] R. Musamali, Y.M. Isa, Decomposition of methane to carbon and hydrogen: A catalytic perspective, Energy Technol. 7(6) (2019).

[198] R. Vander Wal, M.M. Nkiawete, Carbons as catalysts in thermo-catalytic hydrocarbon decomposition: A review, C-Journal of Carbon Research 6(2) (2020).

[199] I.W. Wang, D.A. Kutteri, B.Y. Gao, H.J. Tian, J.L. Hu, Methane pyrolysis for carbon nanotubes and CO_x-Free H_2 over transition-metal catalysts, Energy Fuels 33(1) (2019) 197-205.

[200] J.X. Qian, L.R. Enakonda, W.J. Wang, D. Gary, P. Del-Gallo, J.M. Basset, D.B. Liu, L. Zhou, Optimization of a fluidized bed reactor for methane decomposition over Fe/Al_2O_3 catalysts: Activity and regeneration studies, Int. J. Hydrogen Energy 44(60) (2019) 31700-31711.

[201] D. Kang, C. Palmer, D. Mannini, N. Rahimi, M.J. Gordon, H. Metiu, E.W. McFarland, Catalytic methane pyrolysis in molten alkali chloride salts containing iron, ACS Catal. 10(13) (2020) 7032-7042.

[202] L. Zhou, L.R. Enakonda, S. Li, D. Gary, P. Del-Gallo, C. Mennemann, J.M. Basset, Iron ore catalysts for methane decomposition to make CO_x free hydrogen and carbon nano material, J. Taiwan Inst. Chem. Eng. 87 (2018) 54-63.

[203] T.B. Reddy, D. Linden, Linden's handbook of batteries, 4th ed. ed., McGraw-Hill, New York, 2011.

[204] G. Liu, H. Zheng, S. Kim, Y. Deng, A.M. Minor, X. Song, V.S. Battaglia, Effects of Various Conductive Additive and Polymeric Binder Contents on the Performance of a Lithium-Ion Composite Cathode, J. Electrochem. Soc. 155(12) (2008) A887-A892.

[205] B.J. Landi, M.J. Ganter, C.D. Cress, R.A. DiLeo, R.P. Raffaelle, Carbon nanotubes for lithium ion batteries, Energy Environ. Sci. 2(6) (2009) 638-654.

[206] R. Tang, Q.B. Yun, W. Lv, Y.B. He, C.H. You, F.Y. Su, L. Ke, B.H. Li, F.Y. Kang, Q.H. Yang, How a very trace amount of graphene additive works for constructing an efficient conductive network in LiCoO2-based lithium-ion batteries, Carbon 103 (2016) 356-362.

[207] M. Takeno, T. Fukutsuka, K. Miyazaki, T. Abe, Influence of carbonaceous materials on electronic conduction in electrode-slurry, Carbon 122 (2017) 202-206.

[208] S.R. Daemi, C. Tan, T. Volkenandt, S.J. Cooper, A. Palacios-Padros, J. Cookson, D.J.L. Brett, P.R. Shearing, Visualizing the Carbon Binder Phase of Battery Electrodes in Three Dimensions, Acs Applied Energy Materials 1(8) (2018) 3702-3710.

[209] L.T. Xu, W. Lv, K. Shi, S.J. Xiao, C.H. You, Y.B. He, F.Y. Kang, Q.H. Yang, Holey graphenes as the conductive additives for $LiFePO_4$ batteries with an excellent rate performance, Carbon 149 (2019) 257-262.

[210] S. Ko, Y. Yamada, L. Lander, A. Yamada, Stability of conductive carbon additives in 5 V-class Li-ion batteries, Carbon 158 (2020) 766-771.

[211] Y. Huang, Z.X. Li, S.Y. Jin, S.D. Zhang, H.L. Wang, P. Hiralal, G.A.J. Amaratunga, H. Zhou, Carbon nanohorns/nanotubes: An effective binary conductive additive in the cathode of high energy-density zinc-ion rechargeable batteries, Carbon 167 (2020) 431-438.

[212] J. Xiao, J. Han, C. Zhang, G. Ling, F. Kang, Q.-H. Yang, Dimensionality, function and performance of carbon materials in energy storage devices, Adv. Energy Mater. n/a(n/a) (2021) 2100775.

[213] X.X. Ji, Y.B. Mu, J.B. Liang, T. Jiang, J. Zeng, Z.J. Lin, Y.H. Lin, J. Yu, High yield production of 3D graphene powders by thermal chemical vapor deposition and application as highly efficient conductive additive of lithium ion battery electrodes, Carbon 176 (2021) 21-30.

[214] K. Shen, X. Chen, W. Shen, Z.-H. Huang, B. Liu, F. Kang, Thermal and gas purification of natural graphite for nuclear applications, Carbon 173 (2021) 769-781.

[215] A.D. Jara, A. Betemariam, G. Woldetinsae, J.Y. Kim, Purification, application and current market trend of natural graphite: A review, International Journal of Mining Science and Technology 29(5) (2019) 671-689.

[216] M. Yoshio, H. Wang, K. Fukuda, Y. Hara, Y. Adachi, Effect of Carbon Coating on Electrochemical Performance of Treated Natural Graphite as Lithium-Ion Battery Anode Material, Journal of The Electrochemical Society 147(4) (2000) 1245.

[217] K. Parvez, Z.-S. Wu, R. Li, X. Liu, R. Graf, X. Feng, K. Müllen, Exfoliation of graphite into graphene in aqueous solutions of inorganic salts, J. Am. Chem. Soc. 136(16) (2014) 6083-6091.

[218] T.C. Achee, W. Sun, J.T. Hope, S.G. Quitzau, C.B. Sweeney, S.A. Shah, T. Habib, M.J. Green, High-yield scalable graphene nanosheet production from compressed graphite using electrochemical exfoliation, Sci. Rep. 8(1) (2018) 1-8.

[219] F. Liu, C. Wang, X. Sui, M.A. Riaz, M. Xu, L. Wei, Y. Chen, Synthesis of graphene materials by electrochemical exfoliation: Recent progress and future potential, Carbon Energy 1(2) (2019) 173-199.

[220] R. Saito, M. Hofmann, G. Dresselhaus, A. Jorio, M. Dresselhaus, Raman spectroscopy of graphene and carbon nanotubes, Adv. Phys. 60(3) (2011) 413-550.

[221] A.C. Ferrari, D.M. Basko, Raman spectroscopy as a versatile tool for studying the properties of graphene, Nat. Nanotechnol. 8(4) (2013) 235-246.

[222] D. Pantea, H. Darmstadt, S. Kaliaguine, L. Sümmchen, C. Roy, Electrical conductivity of thermal carbon blacks: Influence of surface chemistry, Carbon 39(8) (2001) 1147-1158.

[223] B. Marinho, M. Ghislandi, E. Tkalya, C.E. Koning, G. de With, Electrical conductivity of compacts of graphene, multi-wall carbon nanotubes, carbon black, and graphite powder, Powder Technol. 221 (2012) 351-358.

[224] I. Cho, J. Choi, K. Kim, M.-H. Ryou, Y.M. Lee, A comparative investigation of carbon black (Super-P) and vapor-grown carbon fibers (VGCFs) as conductive additives for lithium-ion battery cathodes, RSC Adv. 5(115) (2015) 95073-95078.

[225] J. Yan, K. Dong, Y. Zhang, X. Wang, A.A. Aboalhassan, J. Yu, B. Ding, Multifunctional flexible membranes from sponge-like porous carbon nanofibers with high conductivity, Nat. Commun. 10(1) (2019) 1-9.

[226] J. Lahaye, M. Wetterwald, J. Messiet, Electrolyte absorption capacity of conducting carbon blacks used in Leclanche type batteries, J. Appl. Electrochem. 14(1) (1984) 117-122.

[227] X. Yu, Y. Fu, X. Cai, H. Kafafy, H. Wu, M. Peng, S. Hou, Z. Lv, S. Ye, D. Zou, Flexible fiber-type zinc–carbon battery based on carbon fiber electrodes, Nano Energy 2(6) (2013) 1242-1248.

[228] L. Li, T.K. Hoang, J. Zhi, M. Han, S. Li, P. Chen, Functioning mechanism of the secondary aqueous Zn-β-MnO_2 battery, ACS Appl. Mater. Interfaces 12(11) (2020) 12834-12846.

[229] B. Zhang, Y. Yu, Y. Liu, Z.-D. Huang, Y.-b. He, J.-K. Kim, Percolation threshold of graphene nanosheets as conductive additives in Li 4 Ti 5 O 12 anodes of Li-ion batteries, Nanoscale 5(5) (2013) 2100-2106.

[230] R. Tian, N. Alcala, S.J. O'Neill, D.V. Horvath, J. Coelho, A.J. Griffin, Y. Zhang, V. Nicolosi, C. O'Dwyer, J.N. Coleman, Quantifying the effect of electronic conductivity on the rate performance of nanocomposite battery electrodes, ACS Appl. Energy Mater. 3(3) (2020) 2966-2974.

[231] Z. Ju, X. Zhang, S.T. King, C.D. Quilty, Y. Zhu, K.J. Takeuchi, E.S. Takeuchi, D.C. Bock, L. Wang, A.C. Marschilok, Unveiling the dimensionality effect of conductive fillers in thick battery electrodes for high-energy storage systems, Appl. Phys. Rev. 7(4) (2020) 041405.

[232] X. Fan, Y. Zhu, C. Luo, L. Suo, Y. Lin, T. Gao, K. Xu, C. Wang, Pomegranate-structured conversion-reaction cathode with a built-in Li source for high-energy Li-ion batteries, ACS nano 10(5) (2016) 5567-5577.

[233] W. Sun, F. Wang, S. Hou, C. Yang, X. Fan, Z. Ma, T. Gao, F. Han, R. Hu, M. Zhu, Zn/MnO_2 battery chemistry with H^+ and Zn^{2+} coinsertion, J. Am. Chem. Soc. 139(29) (2017) 9775-9778.

[234] Y.J. Kim, A.C. Marschilok, K.J. Takeuchi, E.S. Takeuchi, Silver vanadium phosphorous oxide, $Ag_2VO_2PO_4$: Chimie douce preparation and resulting lithium cell electrochemistry, J. Power Sources 196(16) (2011) 6781-6787.

[235] K. Giagloglou, J.L. Payne, C. Crouch, R.K. Gover, P.A. Connor, J.T. Irvine, Transition metal chlorides $NiCl_2$, $KNiCl_3$, Li_6VCl_8 and Li_2MnCl_4 as alternative cathode materials in primary Li thermal batteries, J. Electrochem. Soc. 165(14) (2018) A3510.

[236] W. Kiciński, S. Dyjak, Transition metal impurities in carbon-based materials: Pitfalls, artifacts and deleterious effects, Carbon 168 (2020) 748-845.

[237] S. Sharma, S.K. Ghoshal, Hydrogen the future transportation fuel: From production to applications, Renewable Sustainable Energy Rev. 43 (2015) 1151-1158.

[238] F. Dawood, M. Anda, G. Shafiullah, Hydrogen production for energy: An overview, Int. J. Hydrogen Energy 45(7) (2020) 3847-3869.

[239] P. Nikolaidis, A. Poullikkas, A comparative overview of hydrogen production processes, Renewable Sustainable Energy Rev. 67 (2017) 597-611.

[240] T. da Silva Veras, T.S. Mozer, A. da Silva César, Hydrogen: trends, production and characterization of the main process worldwide, Int. J. Hydrogen Energy 42(4) (2017) 2018-2033.

[241] T. Zhang, M.D. Amiridis, Hydrogen production via the direct cracking of methane over silica-supported nickel catalysts, Appl. Catal., A 167(2) (1998) 161-172.

[242] U. Ashik, W.W. Daud, J.-i. Hayashi, A review on methane transformation to hydrogen and nanocarbon: Relevance of catalyst characteristics and experimental parameters on yield, Renewable Sustainable Energy Rev. 76 (2017) 743-767.

[243] J.X. Qian, T.W. Chen, L.R. Enakonda, D.B. Liu, J.-M. Basset, L. Zhou, Methane decomposition to pure hydrogen and carbon nano materials: State-of-the-art and future perspectives, Int. J. Hydrogen Energy 45(32) (2020) 15721-15743.

[244] L. Alves, V. Pereira, T. Lagarteira, A. Mendes, Catalytic methane decomposition to boost the energy transition: Scientific and technological advancements, Renewable Sustainable Energy Rev. 137 (2021) 110465.

[245] X. Zhou, Q. Liu, C. Jiang, B. Ji, X. Ji, Y. Tang, H.M. Cheng, Strategies towards low-cost dual-ion batteries with high performance, Angew. Chem., Int. Ed. 59(10) (2020) 3802-3832.

[246] T. Placke, A. Heckmann, R. Schmuch, P. Meister, K. Beltrop, M. Winter, Perspective on performance, cost, and technical challenges for practical dual-ion batteries, Joule 2(12) (2018) 2528-2550.

[247] S. Chen, Q. Kuang, H.J. Fan, Dual-Carbon Batteries: Materials and Mechanism, Small 16(40) (2020) 2002803.

[248] M. Wang, Y. Tang, A review on the features and progress of dual-ion batteries, Adv. Energy Mater. 8(19) (2018) 1703320.

[249] Y. Sui, C. Liu, R.C. Masse, Z.G. Neale, M. Atif, M. AlSalhi, G. Cao, Dual-ion batteries: The emerging alternative rechargeable batteries, Energy Storage Mater. 25 (2020) 1-32.

[250] M. Tebyetekerwa, T.T. Duignan, Z. Xu, X. Song Zhao, Rechargeable Dual-Carbon Batteries: A Sustainable Battery Technology, Adv. Energy Mater. (2022) 2202450.

[251] Z. Guo, Z. Xu, F. Xie, J. Feng, M. Titirici, Strategies for High Energy Density Dual-Ion Batteries Using Carbon-Based Cathodes, Adv. Energy Sustainability Res. 2(11) (2021) 2100074.

[252] H. Jiang, Z. Chen, Y. Yang, C. Fan, J. Zhao, G. Cui, Rational Design of Functional Electrolytes Towards Commercial Dual-Ion Batteries, ChemSusChem 16(4) (2023) e202201561.

[253] X. Tong, F. Zhang, B. Ji, M. Sheng, Y. Tang, Carbon-coated porous aluminum foil anode for high-rate, long-term cycling stability, and high energy density dual-ion batteries, Adv. Mater. 28(45) (2016) 9979-9985.

[254] C. Jiang, Y. Fang, J. Lang, Y. Tang, Integrated configuration design for ultrafast rechargeable dual-ion battery, Adv. Energy Mater. 7(19) (2017) 1700913.

[255] H.-J. Liao, Y.-M. Chen, Y.-T. Kao, J.-Y. An, Y.-H. Lai, D.-Y. Wang, Freestanding cathode electrode design for high-performance sodium dual-ion battery, J. Phys. Chem. C 121(44) (2017) 24463-24469.

[256] K.V. Kravchyk, P. Bhauriyal, L. Piveteau, C.P. Guntlin, B. Pathak, M.V. Kovalenko, High-energy-density dual-ion battery for stationary storage of electricity using concentrated potassium fluorosulfonylimide, Nat. Commun. 9(1) (2018) 1-9.

[257] J. Park, Z.L. Xu, G. Yoon, S.K. Park, J. Wang, H. Hyun, H. Park, J. Lim, Y.J. Ko, Y.S. Yun, Stable and high-power calcium-ion batteries enabled by calcium intercalation into graphite, Adv. Mater. 32(4) (2020) 1904411.

[258] X. Lei, Y. Zheng, F. Zhang, Y. Wang, Y. Tang, Highly stable magnesium-ion-based dual-ion batteries based on insoluble small-molecule organic anode material, Energy Storage Mater. 30 (2020) 34-41.

[259] Q. Guo, K.i. Kim, H. Jiang, L. Zhang, C. Zhang, D. Yu, Q. Ni, X. Chang, T. Chen, H. Xia, A high-potential anion-insertion carbon cathode for aqueous zinc dual-ion battery, Adv. Funct. Mater. 30(38) (2020) 2002825.

[260] Y. Qiao, K. Jiang, X. Li, H. Deng, Y. He, Z. Chang, S. Wu, S. Guo, H. Zhou, A hybrid electrolytes design for capacity-equivalent dual-graphite battery with superior long-term cycle life, Adv. Energy Mater. 8(24) (2018) 1801120.

[261] J. Yan, S. Li, B. Lan, Y. Wu, P.S. Lee, Rational design of nanostructured electrode materials toward multifunctional supercapacitors, Adv. Funct. Mater. 30(2) (2020) 1902564.

[262] F. Wang, X. Wu, X. Yuan, Z. Liu, Y. Zhang, L. Fu, Y. Zhu, Q. Zhou, Y. Wu, W. Huang, Latest advances in supercapacitors: from new electrode materials to novel device designs, Chem. Soc. Rev. 46(22) (2017) 6816-6854.

[263] J. Huang, Y. Xie, Y. You, J. Yuan, Q. Xu, H. Xie, Y. Chen, Rational Design of Electrode Materials for Advanced Supercapacitors: From Lab Research to Commercialization, Adv. Funct. Mater. (2023) 2213095.

[264] X. Chen, R. Paul, L. Dai, Carbon-based supercapacitors for efficient energy storage, National Science Review 4(3) (2017) 453-489.

[265] E.Y.L. Teo, L. Muniandy, E.-P. Ng, F. Adam, A.R. Mohamed, R. Jose, K.F. Chong, High surface area activated carbon from rice husk as a high performance supercapacitor electrode, Electrochim. Acta 192 (2016) 110-119.

[266] W.H. Li, Q.L. Ning, X.T. Xi, B.H. Hou, J.Z. Guo, Y. Yang, B. Chen, X.L. Wu, Highly improved cycling stability of anion de-/intercalation in the graphite cathode for dual-ion batteries, Adv. Mater. 31(4) (2019) 1804766.

[267] Z. Xu, F. Xie, J. Wang, H. Au, M. Tebyetekerwa, Z. Guo, S. Yang, Y.S. Hu, M.M. Titirici, All-cellulose-based quasi-solid-state sodium-ion hybrid capacitors enabled by structural hierarchy, Adv. Funct. Mater. 29(39) (2019) 1903895.

[268] J.A. Read, A.V. Cresce, M.H. Ervin, K. Xu, Dual-graphite chemistry enabled by a high voltage electrolyte, Energy Environ. Sci. 7(2) (2014) 617-620.

[269] R. Hou, B. Liu, Y. Sun, L. Liu, J. Meng, M.D. Levi, H. Ji, X. Yan, Recent advances in dual-carbon based electrochemical energy storage devices, Nano Energy 72 (2020) 104728.

[270] T. Liu, X. Han, Z. Zhang, Z. Chen, P. Wang, P. Han, N. Ding, G. Cui, A high concentration electrolyte enables superior cycleability and rate capability for high voltage dual graphite battery, J. Power Sources 437 (2019) 226942.

[271] A. Heckmann, J. Thienenkamp, K. Beltrop, M. Winter, G. Brunklaus, T. Placke, Towards high-performance dual-graphite batteries using highly concentrated organic electrolytes, Electrochim. Acta 260 (2018) 514-525.

[272] Y. Wang, Y. Zhang, S. Wang, S. Dong, C. Dang, W. Hu, D.Y. Yu, Ultrafast Charging and Stable Cycling Dual-Ion Batteries Enabled via an Artificial Cathode–Electrolyte Interface, Adv. Funct. Mater. 31(29) (2021) 2102360.

[273] Y. Wang, Y. Zhang, Q. Duan, P.-K. Lee, S. Wang, Y. Denis, Engineering cathode-electrolyte interface of graphite to enable ultra long-cycle and high-power dual-ion batteries, J. Power Sources 471 (2020) 228466.

[274] M. Zhang, Y. Pei, W. Liu, R. Liang, Y.-P. Deng, Z. Chen, A. Yu, Rational design of interlayer binding towards highly reversible anion intercalation cathode for dual ion batteries, Nano Energy 81 (2021) 105643.

[275] T. Placke, S. Rothermel, O. Fromm, P. Meister, S.F. Lux, J. Huesker, H.-W. Meyer, M. Winter, Influence of graphite characteristics on the electrochemical intercalation of bis (trifluoromethanesulfonyl) imide anions into a graphite-based cathode, J. Electrochem. Soc. 160(11) (2013) A1979.

[276] Y. Pan, V. Lo, L. Cao, A. Roy, B. Chivers, N. Noorbehesht, Y. Yao, J. Wang, L. Wei, Y. Chen, Graphitic carbon from catalytic methane decomposition as efficient conductive additives for zinc-carbon batteries, Carbon 192 (2022) 84-92.

[277] M. Pudukudy, Z. Yaakob, N. Dahani, M.S. Takriff, N.S.M. Hassan, Production of COx free hydrogen and nanocarbon via methane decomposition over unsupported porous nickel and iron catalysts, J. Cluster Sci. 28(3) (2017) 1579-1594.

[278] K. Parvez, Z.-S. Wu, R. Li, X. Liu, R. Graf, X. Feng, K. Müllen, Exfoliation of graphite into graphene in aqueous solutions of inorganic salts, J. Am. Chem. Soc. 136(16) (2014) 6083-6091.

[279] T.C. Achee, W. Sun, J.T. Hope, S.G. Quitzau, C.B. Sweeney, S.A. Shah, T. Habib, M.J. Green, High-yield scalable graphene nanosheet production from compressed graphite using electrochemical exfoliation, Sci. Rep. 8(1) (2018) 14525.

[280] P. Han, X. Han, J. Yao, L. Yue, J. Zhao, X. Zhou, G. Cui, Mesocarbon microbead based dual-carbon batteries towards low cost energy storage devices, J. Power Sources 393 (2018) 145-151.

[281] B. Ji, F. Zhang, N. Wu, Y. Tang, A dual-carbon battery based on potassium-ion electrolyte, Adv. Energy Mater. 7(20) (2017) 1700920.

[282] Z. Cheng, L. Guo, Q. Dong, C. Wang, Q. Yao, X. Gu, J. Yang, Y. Qian, Highly Durable and Ultrafast Cycling of Dual-Ion Batteries via In Situ Construction of Cathode–Electrolyte Interphase, Adv. Energy Mater. 12(44) (2022) 2202253.

[283] X. Li, X. Ou, Y. Tang, 6.0 V high-voltage and concentrated electrolyte toward high energy density K-based dual-graphite battery, Adv. Energy Mater. 10(41) (2020) 2002567.

[284] G. Wang, F. Wang, P. Zhang, J. Zhang, T. Zhang, K. Müllen, X. Feng, Polarity-switchable symmetric graphite batteries with high energy and high power densities, Adv. Mater. 30(39) (2018) 1802949.

[285] F.A. Kayakool, B. Gangaja, S. Nair, D. Santhanagopalan, Li-based all-carbon dual-ion batteries using graphite recycled from spent Li-ion batteries, Sustainable Mater. Technol. 28 (2021) e00262.

[286] J. Zhu, Y. Li, B. Yang, L. Liu, J. Li, X. Yan, D. He, A dual carbon-based potassium dual ion battery with robust comprehensive performance, Small 14(31) (2018) 1801836.

[287] Z. Zhou, N. Li, Y. Yang, H. Chen, S. Jiao, W.L. Song, D. Fang, Ultra-Lightweight 3D Carbon Current Collectors: Constructing All-Carbon Electrodes for Stable and High Energy Density Dual-Ion Batteries, Adv. Energy Mater. 8(26) (2018) 1801439.

[288] S. Alvin, H.S. Cahyadi, J. Hwang, W. Chang, S.K. Kwak, J. Kim, Revealing the intercalation mechanisms of lithium, sodium, and potassium in hard carbon, Adv. Energy Mater. 10(20) (2020) 2000283.

[289] S. Karimi, A. Heidarpour, S. Ghasemi, Structural and Morphological Characterization of the Expanded Graphite Obtained by Ball Milling and HF Leaching, Iran. J. Mater. Sci. Eng. 18(2) (2021) 1-12.

[290] L. Li, M. Wang, J. Guo, M. Cao, H. Qiu, L. Dai, Z. Yang, Regulation of radicals from electrochemical exfoliation of a double-graphite electrode to fabricate high-quality graphene, J. Mater. Chem. C 6(23) (2018) 6257-6263.

[291] S. Yang, S. Brüller, Z.-S. Wu, Z. Liu, K. Parvez, R. Dong, F. Richard, P. Samorì, X. Feng, K. Müllen, Organic radical-assisted electrochemical exfoliation for the scalable production of high-quality graphene, J. Am. Chem. Soc. 137(43) (2015) 13927-13932.

[292] R. Blyth, H. Buqa, F. Netzer, M. Ramsey, J. Besenhard, P. Golob, M. Winter, XPS studies of graphite electrode materials for lithium ion batteries, Applied Surface Science 167(1-2) (2000) 99-106.

[293] L. Zhou, L.R. Enakonda, S. Li, D. Gary, P. Del-Gallo, C. Mennemann, J.M. Basset, Iron ore catalysts for methane decomposition to make COx free hydrogen and carbon nano material, J. Taiwan Inst. Chem. Eng. 87 (2018) 54-63.

[294] M. Inaba, Z. Zhang, K. Matsuoka, Y. Soneda, Optimization of the reaction conditions for Fe-catalyzed decomposition of methane and characterization of the produced nanocarbon fibers, Catal. Today 332 (2019) 11-19.

[295] X. Jiang, L. Luo, F. Zhong, X. Feng, W. Chen, X. Ai, H. Yang, Y. Cao, Electrolytes for dual-carbon batteries, ChemElectroChem 6(10) (2019) 2615-2629.

[296] J.A. Read, In-situ studies on the electrochemical intercalation of hexafluorophosphate anion in graphite with selective cointercalation of solvent, J. Phys. Chem. C 119(16) (2015) 8438-8446.

[297] Q. Liu, S. Chen, X. Yu, L. Fan, J. Wang, T. Wang, R. Ma, X. Han, B. Lu, Low Cost and Superior Safety Industrial Grade Lithium Dual-Ion Batteries with a Second Life, Energy Technol. 6(10) (2018) 1994-2000.

[298] Y. Wang, S. Wang, Y. Zhang, P.-K. Lee, D.Y. Yu, Unlocking the true capability of graphite-based dual-ion batteries with ethyl methyl carbonate electrolyte, ACS Appl. Energy Mater. 2(10) (2019) 7512-7517.

[299] D. Zhu, L. Zhang, Y. Huang, J. Li, H. Fan, H. Wang, Ethylmethyl carbonate's role in hexafluorophosphate storage in graphite electrodes, ACS Appl. Energy Mater. 2(11) (2019) 8031-8038.

[300] J. Seel, J. Dahn, Electrochemical intercalation of PF 6 into graphite, J. Electrochem. Soc. 147(3) (2000) 892.

[301] W. Zhou, P.H.-L. Sit, First-principles understanding of the staging properties of the graphite intercalation compounds towards dual-ion battery applications, ACS omega 5(29) (2020) 18289-18300.

[302] S. Qiu, L. Xiao, M.L. Sushko, K.S. Han, Y. Shao, M. Yan, X. Liang, L. Mai, J. Feng, Y. Cao, Manipulating adsorption–insertion mechanisms in nanostructured carbon materials for high-efficiency sodium ion storage, Adv. Energy Mater. 7(17) (2017) 1700403.

[303] J. Liu, J. Wang, C. Xu, H. Jiang, C. Li, L. Zhang, J. Lin, Z.X. Shen, Advanced energy storage devices: basic principles, analytical methods, and rational materials design, Adv. Sci. 5(1) (2018) 1700322.

[304] A. Wang, W. Yuan, J. Fan, L. Li, A dual-graphite battery with pure 1-butyl-1-methylpyrrolidinium bis (trifluoromethylsulfonyl) imide as the electrolyte, Energy Technol. 6(11) (2018) 2172-2178.

[305] X. Qi, J. Mao, A high capacity dual-carbon battery universal design for ultrafast lithium/sodium storage, Diamond Relat. Mater. 120 (2021) 108663.

[306] G. Wang, M. Yu, J. Wang, D. Li, D. Tan, M. Löffler, X. Zhuang, K. Müllen, X. Feng, Self-activating, capacitive anion intercalation enables high-power graphite cathodes, Adv. Mater. 30(20) (2018) 1800533.

[307] J. Asenbauer, T. Eisenmann, M. Kuenzel, A. Kazzazi, Z. Chen, D. Bresser, The success story of graphite as a lithium-ion anode material–fundamentals, remaining challenges, and recent developments including silicon (oxide) composites, Sustainable Energy Fuels 4(11) (2020) 5387-5416.

[308] K.H. Chen, V. Goel, M.J. Namkoong, M. Wied, S. Müller, V. Wood, J. Sakamoto, K. Thornton, N.P. Dasgupta, Enabling 6C fast charging of Li-ion batteries with graphite/hard carbon hybrid anodes, Adv. Energy Mater. 11(5) (2021) 2003336.

[309] L. Zhao, B. Ding, X.Y. Qin, Z. Wang, W. Lv, Y.B. He, Q.H. Yang, F. Kang, Revisiting the Roles of Natural Graphite in Ongoing Lithium-Ion Batteries, Adv. Mater. 34(18) (2022) 2106704.

[310] Q. Cheng, Y. Okamoto, N. Tamura, M. Tsuji, S. Maruyama, Y. Matsuo, Graphene-like-graphite as fast-chargeable and high-capacity anode materials for lithium ion batteries, Sci. Rep. 7(1) (2017) 1-14.

[311] T.-H. Park, J.-S. Yeo, M.-H. Seo, J. Miyawaki, I. Mochida, S.-H. Yoon, Enhancing the rate performance of graphite anodes through addition of natural graphite/carbon nanofibers in lithium-ion batteries, Electrochim. Acta 93 (2013) 236-240.

[312] S. Wang, S. Jiao, W.-L. Song, H.-S. Chen, J. Tu, D. Tian, H. Jiao, C. Fu, D.-N. Fang, A novel dual-graphite aluminum-ion battery, Energy Storage Mater. 12 (2018) 119-127.

[313] J. Fan, Z. Zhang, Y. Liu, A. Wang, L. Li, W. Yuan, An excellent rechargeable PP 14 TFSI ionic liquid dual-ion battery, Chem. Commun. 53(51) (2017) 6891-6894.

[314] L. Zhang, Z. Liu, G. Wang, W. Feng, X. Wang, J. Feng, X. Zhang, H. Ma, X. Zhang, Y. Xu, In-situ Sacrificial Positive Additive Strategy for the Construction of a Stable Negative Interface in Dual Graphite Batteries, ChemElectroChem 9(24) (2022) e202200884.

[315] D. Chao, W. Zhou, F. Xie, C. Ye, H. Li, M. Jaroniec, S.-Z. Qiao, Roadmap for advanced aqueous batteries: From design of materials to applications, Science advances 6(21) (2020) eaba4098.

[316] X. Zhang, Y. Tang, F. Zhang, C.S. Lee, A novel aluminum–graphite dual-ion battery, Adv. Energy Mater. 6(11) (2016) 1502588.

[317] S. Rothermel, P. Meister, G. Schmuelling, O. Fromm, H.-W. Meyer, S. Nowak, M. Winter, T. Placke, Dual-graphite cells based on the reversible intercalation of bis (trifluoromethanesulfonyl) imide anions from an ionic liquid electrolyte, Energy Environ. Sci. 7(10) (2014) 3412-3423.